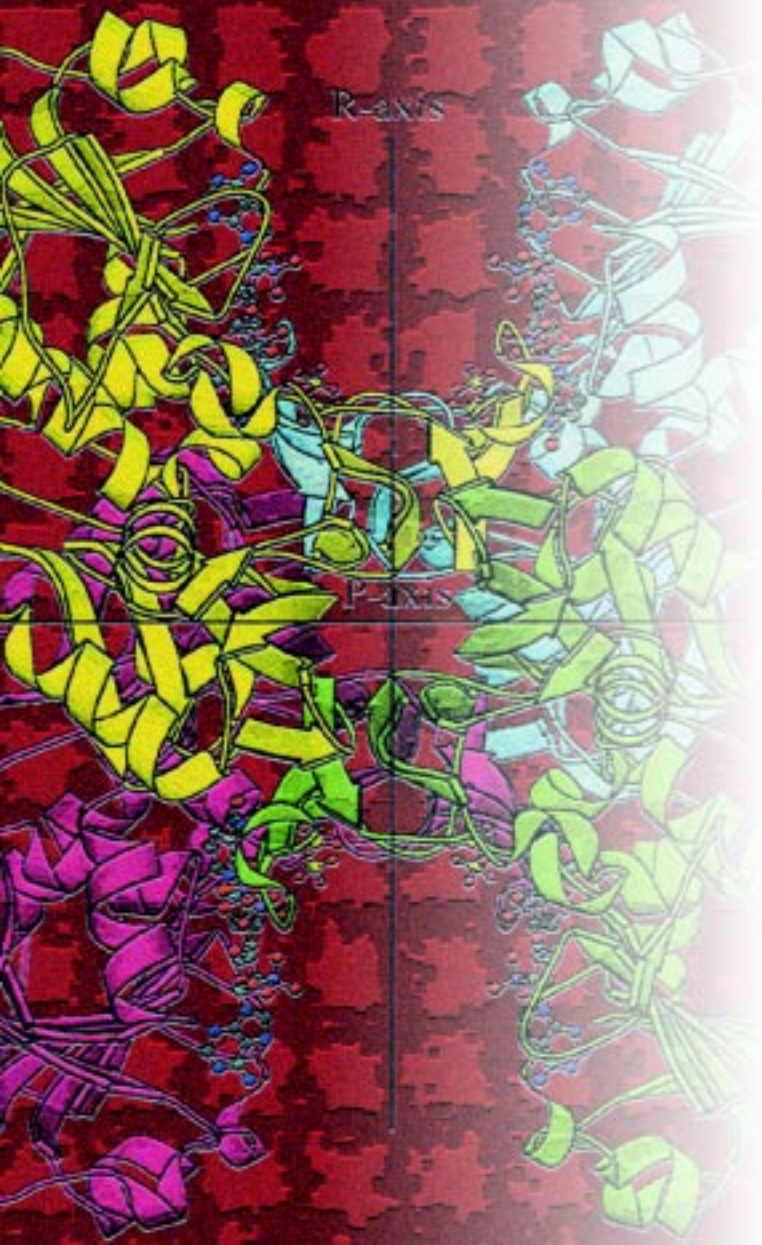


ELETTRA

HIGHLIGHTS

2000 - 2001



**EDITORIAL
COMMITTEE**

Massimo Altarelli
Carlo J. Bocchetta
Kristina Djinovic Carugo
Andrea Goldoni
Claudia Grubissa
Werner Jark
Maurizio Matteucci
Richard P. Walker

Printing & Graphic Design
Tipografia Alabarda, Trieste

HIGHLIGHTS 2000-2001

TABLE OF CONTENTS

5 Introduction

7 Research Highlights

10 *Biomedical Sciences*

Materials and Surfaces

30 *Structural Studies*

40 *Electronic Properties*

55 *Atomic, molecular and supramolecular studies*

63 *Carbon nanotubes*

70 *Instrumentation development*

75 Machine Status

76 *Operational Status and developments*

81 *The ELETTRA Transverse Multi Bunch Feedback System*

86 *Commissioning results of the Low Gap BPM system*

90 *Progress with the European Storage Ring Free-Electron Laser Project at ELETTRA*

93 Facts & Figures

94 *ELETTRA Beamline Status*

95 *ELETTRA Layout*

96 *Statistics of accepted proposals*

98 *Resources allocated at ELETTRA*

99 *Laboratory Staff*

101 Events

103 *Thirteenth International Conference on Vacuum Ultraviolet Radiation Physics*

107 *Inauguration of the Deep X-Ray Lithography beamline*

109 *VIII USERS' MEETING*

111 *Rai International*

111 *IAEA visit*

Introduction

It is a pleasure for me to introduce the new issue of the ELETTRA Highlights, which summarizes the achievements of the last 12 months.

During this period, the quantitative growth of the Laboratory has been evident, with the beginning of operation of the two beamlines devoted to microfabrication, the first data acquired on the Nanospectroscopy beamline, the imminent arrival of the first users on BACH, the new variable polarization beamline. Our program to further develop the beamlines, in collaboration with partner institutions, is going ahead and progress is often limited only by the availability of financial resources.

The first large orders of components of the new injection system (the booster synchrotron) are out. The construction activities will soon be very visible on the site, and other equally important activities for the improvement of the quality of the beams delivered to users are underway : the upgrade of the RF facilities, the development and installation of advanced feedback systems, as well as the recently started realignment of the storage ring.

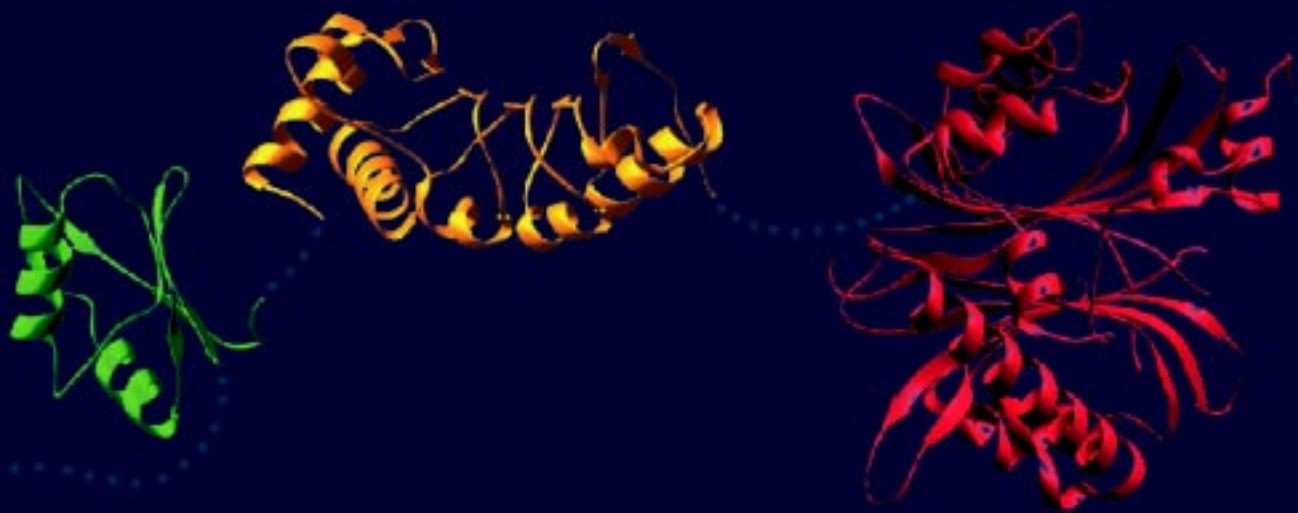
ELETTRA has been confirming its leadership position in FEL (free-electron laser) systems. A new project, with renewed support by the European Union, allows us and our European partners to continue the development of the storage ring FEL (now operating at a wavelength of 190 nm), to reduce the wavelength, and to start a vigorous experimental program. A project in collaboration with the National Institute for the Physics of Matter (INFN) and the Pirelli company to develop an innovative and versatile VUV and soft x-ray FEL, based on the ELETTRA Linac, was formulated and forwarded to the Italian government to request funding.

The experimental program has been vigorously pursued by our users and by the ELETTRA and associated laboratories (GdR) staff. The following pages detail many examples of problems in various fields of science, tackled with the help of synchrotron light.

They underscore the traditional strong points of ELETTRA, such as photoemission spectroscopy and microscopy, and their application to novel materials such as carbon nanotubes; the growing use of ELETTRA in the biomedical sciences, as well as our ability to develop state-of-the-art instrumentation.

I hope you will find these Highlights interesting and pleasant to read

Massimo Altarelli
Managing Director



**Research
Highlights**

Biomedical Sciences

- 10** Structural studies of the mRNA nuclear export factor TAP-p15
S. Fribourg, I.C. Braun, E. Izaurralde, E. Conti
- 12** Diffraction Enhanced X-ray Imaging of Biological Tissues
C. J. Hall, R. A. Lewis, A. P. Hufton, S. Evans, D. R. Dance, F. Arfelli, A. Olivo, L. Rigon, C. R. M. Boggis, I. O. Ellis, A. Evans, S. E. Pinder, L. Jacobs, P. A. McArthur, R. H. Menk, G. Tromba, K. D. Rogers
- 16** Characterization of mineralization in bone diseases
W. Tesch, P. Roschger, K. Klaushofer, I. Zizak, O. Paris, P. Fratzl, S. Bernstorff, H. Amenitsch
- 19** MAD data collection on a Hg derivative crystal of a novel pectate lyase from *Azospirillum irakense*
H. Novoa de Armas, A. Rabijns, C. Verboven, J. Desair, A. Vande broeck, J. Vanderleyden, C. De Ranter
- 22** Glyceraldehyde-3-phosphate dehydrogenases from chloroplasts
S. Fermani, A. Ripamonti, P. Sabatino, G. Zanotti, S. Scagliarini, P. Trost, P. Pupillo
- 26** Use of soft X-ray in phasing of biological macromolecules
M. Polentarutti, K. Djinovic-Carugo
- 28** A New Procedure for Automated Protein Structure Determination involving the use of soft X-rays
M. S. Weiss, T. Sicker, R. Hilgenfeld

Materials and surfaces

Structural studies

- 30** *In Situ*-SAXS Investigations on Zinc Sulphide Precipitation in a Liquid Jet on a Microsecond Time Scale
P. Bussian, W. Schmidt, F. Schüth, P. Ågren, J. Andersson, M. Lindén, H. Amenitsch
- 33** GISAXS study of cadmium sulfide quantum dots reveals clues for design optimization of electro-optical semiconductor devices
P. Dubcek, S. Bernstorff, U.V. Desnica, I.D. Desnica-Frankovic
- 36** Self-assembly of 2D-Hexagonal templated TiO₂ mesostructured films during dip-coating
D. Grosso, F. Babonneau, C. Sanchez, G. J. de A. A. Soler-Illia, E. L. Crepaldi, P.A. Albouy, H. Amenitsch, A.R. Balkenende, A. Brunet-Bruneau

Electronic properties

- 40** Investigation of the LMM Auger spectra of Fe in ultrathin Fe films grown on Cu(100): variations in the lifetime of 3d hole states
S. D'Addato, P. Luches, R. Gotter, L. Floreano, D. Cvetko, A. Morgante, A. Newton, D. Martin, P. Unsworth, P. Weightman

44 Low-dimensional electronic structures on In-terminated InAs(001)-c(4x4) and -(4x2)c(8x2) surfaces

P. De Padova, P. Perfetti, C. Quaresima, C. Richter, M. Zerrouki, K. Hricovini

47 Strong spin-filter effects observed in high-resolution photoemission from Cu(100) with circularly polarized light

R. Frömter, S. Legner, S.V. Borisenko, M.S. Golden, F. Matthes, C.M. Schneider, S. Zennaro, S. Turchini

50 Photoemission lineshape at finite temperature

Ch. Søndergaard, Ch. Schultz, Ph. Hofmann, S. Moreno, J.E Gayone, M.A. Vicente Alvarez, G. Zampieri, S. Lizzit, A. Baraldi

53 Direct experimental evidence of insensitivity of local Schottky barriers to lateral chemical inhomogeneity in case studies of metal/GaN(0001) interfaces

A. Barinov, L. Gregoratti, B. Kaulich, M. Kiskinova

Atomic, molecular and supramolecular studies

55 Coherence and correlation effects in indirect double photoionization

S. Rioual, B. Rouvellou, L. Avaldi, G. Battera, R. Camilloni, G. Stefani, G. Turri

59 X-ray structure of non-covalent calixarene-porphyrin supramolecular complexes with pH tuned stoichiometry

L. Di Costanzo, S. Geremia, L. Randaccio, R. Purrello

Carbon nanotubes

63 Carbon nanotubes

A. Goldoni, M. Kiskinova

64 X-ray photoelectron microscopy of the C1s core level of free standing single-wall carbon nanotubes

A. Goldoni, L. Gregoratti, B. Kaulich, M. Kiskinova, R. Larciprete, L. Sangaletti, F. Parmigiani

68 Electronic structure of aligned carbon nanotubes studied by photoemission microscopy

S. Suzuki, Y. Watanabe, T. Ogino, S. Heun, L. Gregoratti, A. Barinov, B. Kaulich, M. Kiskinova, W. Zhu, C. Bower, O. Zhou

Instrumentation development

70 A UHV compatible hybrid circuit for multichannel data acquisition systems

S. Carrato, G. Cautero, M. Cautero, C. Fava, D. Giuressi, B. Krastanov, P. Lacovig, R. Sergio, R. Tommasini

72 Novel Zone Plate Doublet for Differential Interference Contrast Microscopy Fabricated by means of Electron Beam Lithography

E. Di Fabrizio, B. Kaulich, S. Cabrini, F. Romanato, T. Wilhein, J. Susini

74 Deep X-Ray Lithography at ELETTRA

F. Pérennès, F. De Bona

Structural studies of the mRNA nuclear export factor TAP-p15

S. Fribourg, I.C. Braun, E. Izaurralde, E. Conti
European Molecular Biology Laboratory (EMBL)
Meyerhofstrasse 1, Heidelberg D-69117 Germany

INTRODUCTION

The export of mRNAs from the nucleus (where they are transcribed and processed) to the cytoplasm (where they act in protein synthesis) is a critical process in eukaryotic cells and occurs through nuclear pore complexes (NPCs), large assemblies that form channels across the nuclear envelope. TAP is a human protein that functions as a heterodimer with a small protein known as p15 to export mRNAs across the NPC to the cytoplasm.

TAP is a multidomain protein of 60 kDa. It recognizes RNAs with its N-terminal portion, either directly (as in the case of certain retroviral mRNAs that use this cellular factor to be exported to the cytoplasm of the host cell) or indirectly via additional adaptor proteins (as in the case of cellular mRNAs). Besides recognizing the RNA cargo, the transport factor has to associate with the NPC to translocate between the nuclear and cellular compartments. TAP uses its C-terminal portion to heterodimerize with p15, and this heterodimer is able to recognize the proteins that line the NPC, also known as nucleoporins. Nucleoporins typically contain repetitive sequence motifs (Phe-Gly repeats) which have been shown to be the docking site for TAP and

for many nucleocytoplasmic transport factors. Understanding the structural determinants for nucleoporin docking is essential to gain molecular insight into NPC translocation, and have been investigated using X-ray protein crystallography and synchrotron radiation.

METHODS

After determining the structure of the N-terminal cargo-binding portion of TAP [1], we recently solved the structure of the TAP-p15 heterodimeric domain in a ternary complex with a nucleoporin fragment [2] (Figure). The structure of the heterodimer was solved with a multiwavelength anomalous dispersion (MAD) experiment carried out at the XRD 1 beamline. In this experiment, a mercury compound was soaked in the crystals and data were collected at 3 different wavelengths around the mercury absorption edge (1.0057 Å, 1.0108 Å and 0.9358 Å for the peak, inflection and remote data sets, respectively). The data were recorded at 2.9 Å resolution with high redundancy and completeness (6.5 / 93.3%, 6.8 / 92.0% and 6.9 / 94.4% for the three data sets). The accuracy of the recorded data

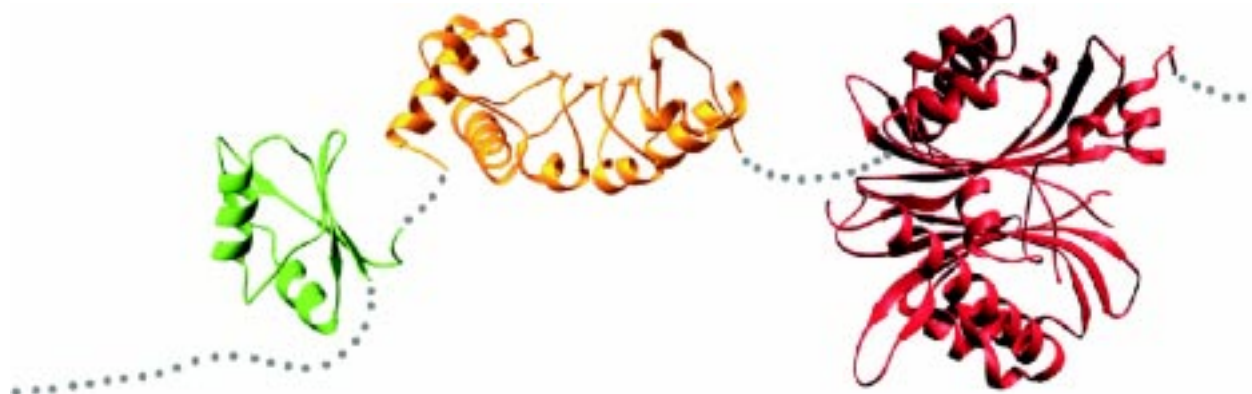


FIGURE. Structural framework of the mRNA export factor TAP-p15 heterodimer determined by X-ray crystallography. The N-terminal RNA-binding portion of TAP consists of a RNP-like domain (green) and a leucine-rich-repeat domain (yellow) [1]. The structure of the downstream domain of TAP in complex with its binding partner p15 (both in red) [2] shows a compact NTF2-like heterodimer which binds specifically a Phe-Gly nucleoporin repeat to mediate transport through the nuclear pore complex [2].

allowed the small changes in the diffraction pattern obtained around the Hg absorption edge to be detected and used successfully in the structure determination. The structure is now refined to 1.9 Å resolution (collected at ESRF) and the structure of its complex with a nucleoporin Phe-Gly (FG) repeat is also solved and refined to 2.8 Å resolution.

RESULTS AND DISCUSSION

The structure of the TAP-p15 heterodimer has a similar overall architecture of NTF2, a protein also involved in nuclear transport. NTF2 is a homodimer which imports the protein Ran from the cytoplasm to the nucleus. Ran is a GTPase of the Ras superfamily that regulates the bulk of nuclear import and export processes. In contrast to NTF2, however, the structures of TAP and p15 are incompatible with either Ran binding or homodimerization. This excludes the possibility that the mRNA export factor TAP is directly regulated by the GTPase Ran, settling an issue that had been rather controversial in the literature. The TAP-p15 heterodimer binds a nucleoporin FG-repeat sequence in a single hydrophobic pocket in the TAP domain. Although p15 itself does not bind the FG-containing peptide

directly, it contributes indirectly by forming a single structural and functional unit with the NTF2-like domain of TAP. Direct NPC association is mediated exclusively by TAP.

The nucleoporin Phe-Gly repeat binds TAP with a tight turn conformation. The turn is facilitated by the conformationally flexible glycine residues, and allows the insertion of the contiguous phenylalanine residue into an apolar surface pocket of the protein. The specificity of nucleoporin recognition thus appears to depend on both the glycine and phenylalanine residues, while the flanking amino acids of the repeat are not engaged in significant interactions. The fact that essentially only one side chain of the nucleoporin repeat is bound to the transport factor gives molecular insight into the generally low-affinity binding of nucleoporins to the TAP-p15 heterodimer, which is essential to ensure the high rate of RNA translocation through nuclear pore complexes.

ACKNOWLEDGMENTS

We are very grateful to Alberto Cassetta for invaluable assistance in the MAD experiment. The data were recorded under the proposal 2001004.

REFERENCES

- [1] E. Liker, E. Fernandez, E. Izaurralde, E. Conti (2000). *EMBO J.*; 19, 5587-5598
- [2] S. Fribourg, I.C. Braun, E. Izaurralde, E. Conti (2001). *Molecular Cell*; 8, 645-656

Diffraction Enhanced X-ray Imaging of Biological Tissues

C. J. Hall, R. A. Lewis

Daresbury Laboratory, Warrington, WA4 4AD, U.K.

A. P. Hufton

North Western Medical Physics, Christie Hospital, Manchester M20 4BX, U.K.

S. Evans, D. R. Dance

The Royal Marsden NHS Trust, London SW3 6JJ, U.K.

F. Arfelli, A. Olivo, L. Rigon

Department of Physics, Università di Trieste, Italy

C. R. M. Boggis

Manchester Breast Screening, Nightingale Centre, Manchester M20 0PT, U.K.

I. O. Ellis, A. Evans, S. E. Pinder

City Hospital, Nottingham, NG5 1PB, U.K.

L. Jacobs

Cancer Studies Unit, Queens Medical Centre, Nottingham, U.K.

P. A. McArthur

Department of Plastic Surgery, Whiston Hospital, Liverpool, U.K.

R. H. Menk, G. Tromba

Sincrotrone Trieste Società Consortile per Azioni, Basovizza, Italy

K. D. Rogers

Department of Materials & Medical Sciences, Cranfield University, Swindon, SN6 8LA, U.K.

INTRODUCTION

The purpose of this study was to explore the potential of refraction contrast X-ray imaging of biological systems. Images of a UK mammography test phantom, mouse lungs, heart, liver and legs, together with a human finger, were recorded using the SYRMEP beamline. The technique used has become to be known as ‘Diffraction Enhanced Imaging’ (DEI), which utilises a silicon crystal placed between the sample and the detector. This in effect separates the refracted X-rays from the transmitted and scattered radiation using the Bragg diffraction from the silicon crystal. The contrast in the images produced is related to changes in the X-ray refractive index of the tissues, rather than the absorption coefficient. This results in remarkable clarity compared with conventional X-ray images. Refraction index changes are greatest at the boundaries between different tissues, giving a marked edge enhancement effect and three-dimensional appearance to the images. The technique provides a way of imaging a property of biological tissues not yet clinically exploited, and further studies are

planned to identify specific applications in medical imaging.

Conventional medical X-ray imaging relies on differences in linear attenuation coefficients between the different tissues to produce differences in photon fluxes incident upon the detector. Whilst these differences are substantial between bone and soft tissue, for example, they are very small between the different types of soft tissue. The result of this is that the inherent contrast between soft tissues is very low. Contrast, or signal to noise ratio, can be maximised by using low X-ray energies and high exposures, but the radiation dose to the patient places practical limits on this.

In recent years, techniques have been developed which enable differences in the refractive index of different tissues to be exploited as an imaging tool. The refractive index for most materials differs from unity by only a few parts per million at X-ray energies. The difference between the refractive index for different tissues in a typical sample is about 100 times smaller than this; so to use this property to produce images was a challenge.

To date, relatively little work has been carried

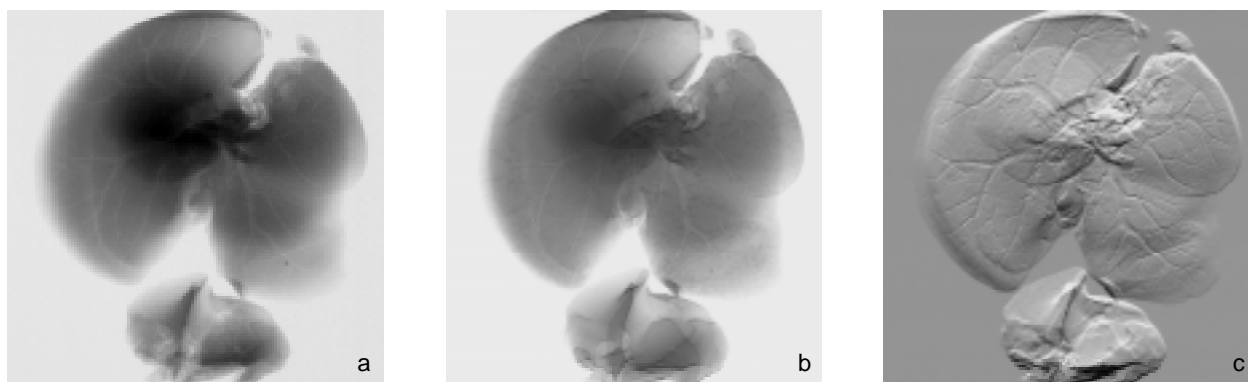


Figure 1. DEI images of a preserved mouse liver. The first (a) shows a radiogram taken with no analyser crystal. This would be similar to, but somewhat better than an image taken with a conventional x-ray generator / film system. The next (b) shows the image taken with the analyser crystal at the peak of its reflectivity curve. Finally image (c) shows an image processed to show only the refraction changes.

out using DEI to image biological tissues, and its potential for medical imaging has not yet been fully explored. Most work has involved imaging mice [1, 2] and as far as we are aware, the only human tissues imaged using DEI have been breast tissue samples [3, 4]. Our aim was therefore to investigate the feasibility of producing DEI images of a wider selection of animal and human organs and tissues. This would be an initial step in identifying which areas of clinical radiology might benefit from the new type of information displayed in these images.

We chose to image the lungs, liver, heart and leg dissected from a mouse. One of our aims was to compare DEI images with conventional X-ray images for pathological analysis. Our clinical colleagues were using mouse models to design drugs, which reduce the propensity for metastatic spread of breast cancer to bone. We were also hoping to try and identify new clinical information that could be visualised with DEI, and point the way to possible

applications in clinical radiology. During our beam time we also used DEI to image a cadaverous human finger. This was in collaboration with a hand surgeon who was delighted at the degree of bone and soft tissue detail present together in the images. Finally, DEI images were acquired of a TOR(MAM) phantom (Department of Medical Physics, Leeds University, UK). This is a semi-quantitative image quality test phantom widely used in the NHS Breast Screening Programme in Britain. It was imaged in line with with 3 cm of polymethylmethacrylate (Lucite, Perspex, Plexiglass) plastic, as it would be used for assessing conventional mammographic imaging systems.

IMAGES

Five types of images are displayed in this paper. For the dissected mouse liver, lung, heart, and the



Figure 2. DEI images of a preserved mouse lung. Once again (a) shows a radiogram taken with no analyser crystal. The second (b) shows the image taken with the analyser crystal at the peak of its reflectivity curve. Finally image (c) shows the apparent refraction image.

TOR(MAM) phantom, conventional radiograms were recorded using the synchrotron beam and the same detector close up to the sample. The ‘peak of reflection’ images were recorded with the analyser crystal set for maximum reflectivity with no sample in the beam. These images represent absorption contrast that is almost entirely free of scattered radiation, which would cause loss of signal to noise ratio (fogging) in a conventional radiogram. The ‘apparent absorption’ and ‘apparent refraction’ images were produced using the method described by Zhong et al, 2000 [2]. These images are synthesised from two images recorded with the analyser set to the 50% reflectivity point on either side of the reflectivity curve. The apparent absorption image contains practically the same information as the peak of reflectivity image but is somewhat noisier since it is a combination of two images. The refraction image contains information, which is entirely different from absorption contrast and represents the gradient of refractive index.

RESULTS AND DISCUSSION

As can be seen from the figures, all sets of images have similar characteristics. The peak of reflection and apparent absorption images are much clearer than the conventional radiograms. This is partly as a result of the improved contrast, due to the almost total absence of scatter, and partly due to the slight edge enhancement. The apparent refraction images show a marked edge enhancement effect. One edge of a structure appears lighter and the other darker, than the surrounding tissue. This gives the images a three-dimensional appearance. One other point to note, since DEI is sensitive to changes in refractive index rather than the absolute value, the refraction images



Figure 3. DEI images of a preserved mouse leg. A line of research undertaken by our colleagues is studying cancer metastases in the bone. They provided us with these control samples. DEI images should show the effect of this disease in much better detail than current conventional x-ray imaging. Image (a) show the peak of reflection image. Image (b) shows the apparent refraction.

lack any large area contrast.

Figure 1 shows our images of the mouse liver. The peak of reflection image (Fig. 1b) visualises the branching structures within the liver parenchyma more clearly than the conventional image (Fig. 1a). These vessels are seen even more clearly on the refraction image (Fig. 1c); the peripheral branching being seen extremely clearly down to approximately 50 μm resolution. It seems likely from the configuration of the central vessels that at least some

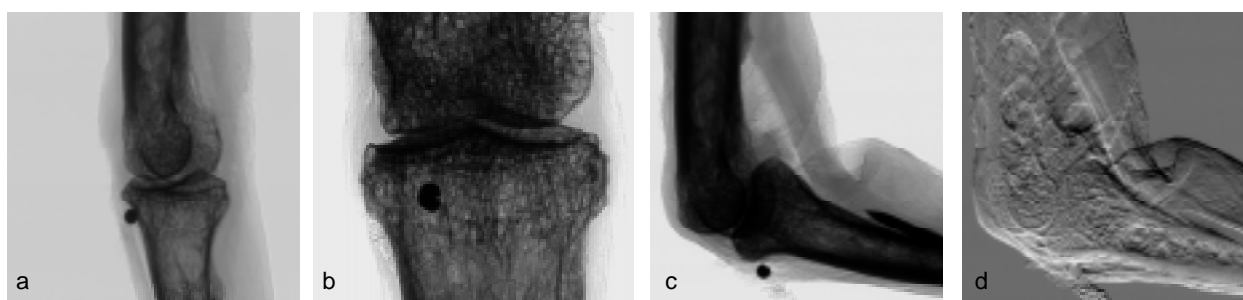


Figure 4. These images demonstrate the unique ability of DEI to show soft tissue detail as well as bone structure in the same contrast scale. Figure 4a shows the peak of reflectivity image for the finger joint under observation. Medics know this as the Proximal Interphalangeal Joint or PIP. The black ball seen below the knuckle was a lead ball used as a reference marker in past studies. A close up of the joint can be seen in (b). Figure 4c shows the joint, and the associated soft tissue structures, when the finger is flexed to right angles. The tendon, and its cuffs and ‘pulleys’ can be seen clearly. The pin seen in the lower left of the image is immobilising the next knuckle joint along. The last image is the apparent refraction image in the same orientation. Note the highlighting effect on the tendon.

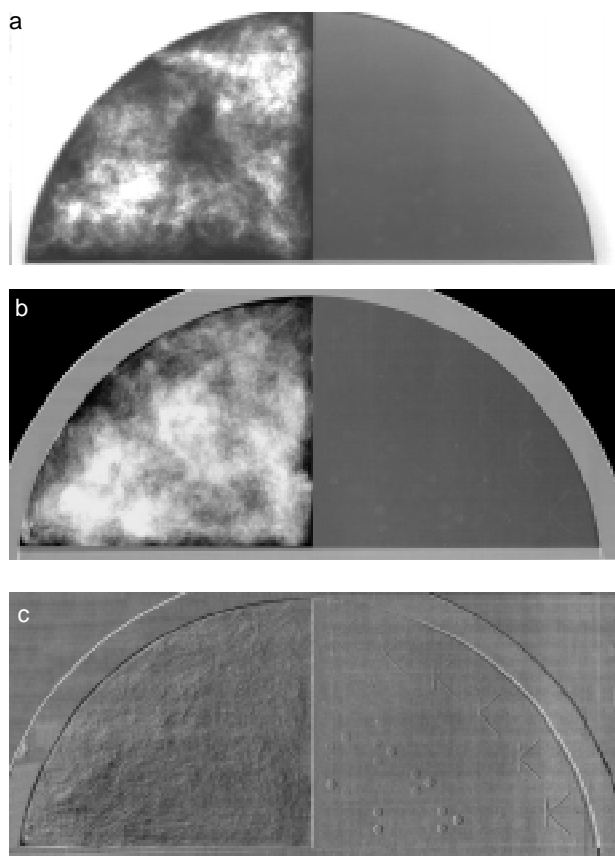


Figure 5. DEI images of the UK TorMam mammography phantom. Figure 5a shows a typical calibration image of this phantom on a standard mammography set. There are image quality features on the left hand half, which are barely visible. The peak of reflectivity image is shown in figure 5b. This shows a clear improvement, with a lot of the features now readily visible. The apparent refraction image (c) demonstrates well the remarkable 3-D effect that DEI provides in the images.

of these structures represent portal veins.

The lung images in Figure 2 demonstrate the general features already described. Both the peak of reflection and refraction images clearly show lobular, segmental and sub-segmental bronchi. The peak image (Fig. 2b) also shows areas of aerated lung

parenchyma distinct from the fluid-filled areas. These are seen even more clearly and down to a smaller diameter in the refraction image (Fig. 2c).

The peak of reflection image of the mouse leg (Fig. 3a) demonstrates good structure definition but with minimal detail inside the leg bones. This ‘trabecular’ structure is better seen in the refraction image (Fig. 3b).

Whereas conventional finger radiographs give no useful information on the tendons, one of the main features of the finger images (Fig. 4) is the clear demonstration of the flexor tendons, as well as providing good bone detail in the same images. The refraction image (Fig. 4b) also gives good definition, particularly on the articular surfaces of the bones making the joint. There is much enhanced trabecular detail in both bones. It can also be seen that different structures within the tendons can be seen.

The final set of images (Fig. 5) show conventional and DEI images of the Leeds TOR(MAM) test object. The enhanced visibility of the test details in the upper half of the phantom can clearly be seen in the apparent absorption and, especially, the refraction images. This level of detail is never obtained whilst testing standard mammography equipment. One notable feature is the virtual absence in the refraction image (Fig. 5c) of the vertical fibre structures. This is because the refractive index change is in the horizontal direction, whereas the analyser crystal is oriented to be sensitive to X-rays deflected in the vertical direction. Our next beam time will address this feature of the imaging system, by taking separate images with the object in different orientations, then using digital techniques to combine them.

ACKNOWLEDGMENTS

Thanks to all the SYRMEP team at ELETTRA and the University of Trieste. Work supported by ELETTRA award No. 2000166 via the EU grant HPRI-CT-1999-00033, and EU grant HPRI-CT-1999-50008.

REFERENCES

- [1] Ingal VN and Beliaevskaya EA. Imaging of biological objects in the plane-wave diffraction scheme. *Il Nuovo Cimento* 1997;19:553-560.
- [2] Zhong Z, Thomlinson W, Chapman D and Sayers D. Implementation of diffraction-enhanced imaging experiments at the NSLS and APS. *Nuclear Instruments and Methods in Physics Research A* 2000;450:556-567
- [3] Arfelli F, Bonvicini V, Bravin A, Cantatore G, Castelli E, Dalla Palma L et al. Mammography with synchrotron radiation: phase-detection techniques. *Radiology* 2000;215:286-293
- [4] Pisano ET, Johnston RE, Chapman D, Geradts J, Iacocca MV, Livasy CA et al. Human breast cancer specimens: diffraction - enhanced imaging with histologic correlation - improved conspicuity of lesion detail compared with digital radiography. *Radiology* 2000;214:895-901

Characterization of mineralization in bone diseases

W. Tesch

Erich Schmid Institute of Materials Science, Austrian Academy of Sciences, and Metals Physics Institute, University of Leoben, Leoben, Austria

Ludwig Boltzmann Institute of Osteology & 4th Medical Department, Hanusch Hospital, Vienna, Austria

P. Roschger, K. Klaushofer

Ludwig Boltzmann Institute of Osteology & 4th Medical Department, Hanusch Hospital, Vienna, Austria

I. Zizak

Hahn Meitner Institut, Berlin, Germany

O. Paris, P. Fratzl

Erich Schmid Institute of Materials Science, Austrian Academy of Sciences, and Metals Physics Institute, University of Leoben, Leoben, Austria

S. Bernstorff

Sincrotrone Trieste, Area Science Park, Trieste, Italy

H. Amenitsch

Institute of Biophysics and X-Ray Structure Research, Austrian Academy of Sciences, Graz, Austria

INTRODUCTION

Many biological materials (e.g. wood and bone), but also some artificial materials are hierarchically structured. Human bone for example exhibits a foam-like structure (trabecular bone) which is surrounded by a compact outer layer (cortical bone). From the viewpoint of materials science, the trabeculae with a typical thickness of 200 μm can be described as particle reinforced nano-fibercomposite. The basic building block is the mineralized collagen fibril. The fibrous collagen constitutes the main component of a three dimensional matrix into which the mineral hydroxyapatite forms. The degree of mineralization of the collagenous matrix as well as the size, shape and arrangement of the mineral particles are crucial parameters which influence the mechanical and functional properties of the whole structure [1]. During bone remodeling, old bone is resorbed by specialized biological cells and replaced by new bone matrix. This organic matrix is subsequently mineralized and has – initially – a smaller mineral content than the neighboring old bone.

The reason for mechanically deficient bone in many bone diseases is a localized disorder of the mineralized collagen matrix during bone modeling or remodeling processes. As an example, the process of Paget's disease is initiated by an abnormal increase in bone resorption, with subsequent compensatory increase in new bone formation, resulting in a disorganized mosaic of woven

and lamellar bone. This leads to bone that is expanded in size, less compact, more vascular, and more susceptible to deformity or fracture than normal bone. Another example is coeliac sprue, an inherited disease where one of the symptoms in adults is bone pain and bone weakness.

Therefore, the characterization of bone material in these diseases requires sophisticated methods originating from materials science, such as small-angle X-ray scattering (SAXS), X-ray diffraction (XRD), quantitative backscattered electron imaging (qBEI) or nanoindentation. The aim of such studies is to understand how the integrity of bone is influenced by certain diseases in order to provide sufficient information for medicine to develop efficient diagnoses and therapies.

MATERIALS AND METHODS

In order to find out how the basic collagen-mineral structure is altered in the case of bone diseases, several iliac crest bone samples were investigated (normal, pagetic, coeliac sprue). A combination of scanning small angle X-ray scattering (scanning SAXS) and quantitative backscattered electron imaging (qBEI) studies were applied to study normal and pathologically new formed bone areas in a position resolved way. Small-Angle X-ray Scattering (SAXS) is a commonly used tool for studying the size, shape and orientation

RESULTS AND DISCUSSION

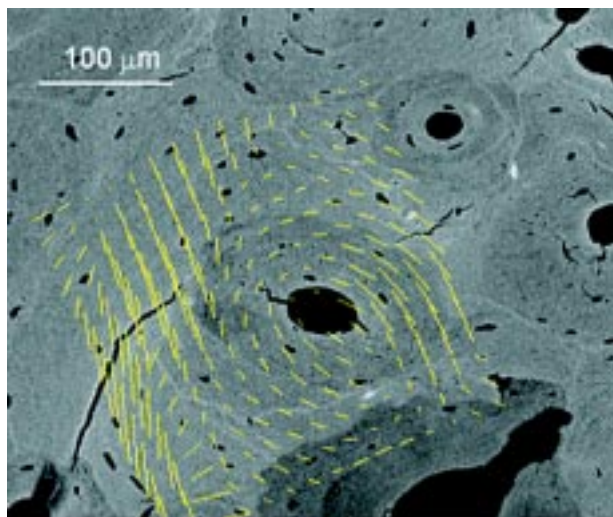


Figure 1. Orientation map of the mineral particles measured by scanning SAXS, overlaid on a qBEI.

of particles in the nanometer-range [2-6]. In recent experiments at ELETTRA we have developed an experimental setup for scanning-SAXS with a spatial resolution of 20 micrometer and applied it to the investigation of healthy human bone samples [2-5]. Prior to the SAXS measurements, qBEI images were taken to map the local mineral density of the iliac crest bone samples. From the digital images, areas of interest were chosen for the scanning SAXS measurements. 20 μm slices were prepared from sections containing the same surface as investigated by qBEI. Using the microbeam-setup at the SAXS beamline at ELETTRA, the first step of the measurement procedure was to acquire a radiography of the sample by detecting the transmitted intensity at each point of the section with an X-ray sensitive diode. This radiography provides an exact mapping of the mineral density distribution in the sample which can be compared with scanning electron micrographs. In the second step, the SAXS-signal was recorded with a 2D-detector, providing line scans or area maps of the area of interest. The 2D-SAXS patterns were evaluated by standard evaluation methods for bone as described in ref. [6].

In the first approach, we investigated the microstructure of bone tissues in osteons of healthy bone. Osteons are regions of compact bone around blood vessels and are particularly interesting due to the high degree of bone remodeling in this regions. By scanning areas of about $0.3 \times 0.3 \text{ mm}^2$, we were able to map some structural parameters of the mineral crystals in compact (lamellar) bone. Figure 1 shows an example of the orientation mapping in the neighborhood of an osteon. The yellow lines superimposed on an backscattered electron image indicate the orientation of the mineral particles embedded in the organic matrix as measured by scanning SAXS at ELETTRA. For this study a total number of four osteons from healthy patients were examined. As illustrated in Figure 1 the mineral particles are arranged in an onion-skin structure around the hole as the mineral particles follow the direction of the lamellae winding around the hole.

As a continuation of these measurements, we investigated new formed bone areas of healthy and diseased human iliac crest bone samples. The backscattered electron image in Figure 2 gives an overview of the trabecular architecture of normal, pagetic and coeliac bone. As the gray-levels of these pictures are proportional to the local calcium content, lower mineralized new formed bone areas (dark gray) and matured bone (brighter levels) can be distinguished for the case of healthy bone in Figure 2a. In contrast, the pagetic bone sample shows the typical mosaic like pattern (Fig. 2b), while the sample from a patient with coeliac spruce reveals trabeculae with a very high porosity (Fig. 2c).

In order to understand if and how the nanostructure of the mineralized collagen matrix is affected by these bone diseases, SAXS line-scans perpendicular to the trabeculae were performed. Figure 3 shows a line-scan across a region of new formed and matured bone from a patient with Paget's disease (Fig. 2b)

In the lower part of the figure (qBEI), high and low

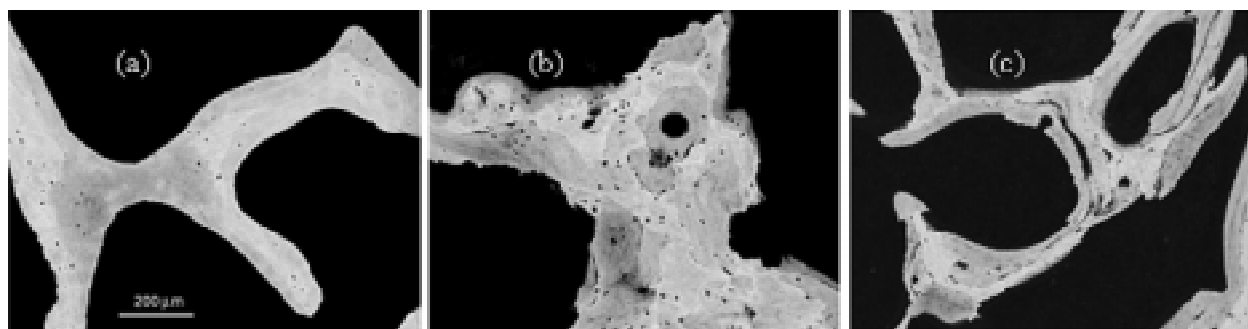


Figure 2 (a-c). Backscattered electron images of normal (a), pagetic (b) and coeliac bone trabeculae (c).

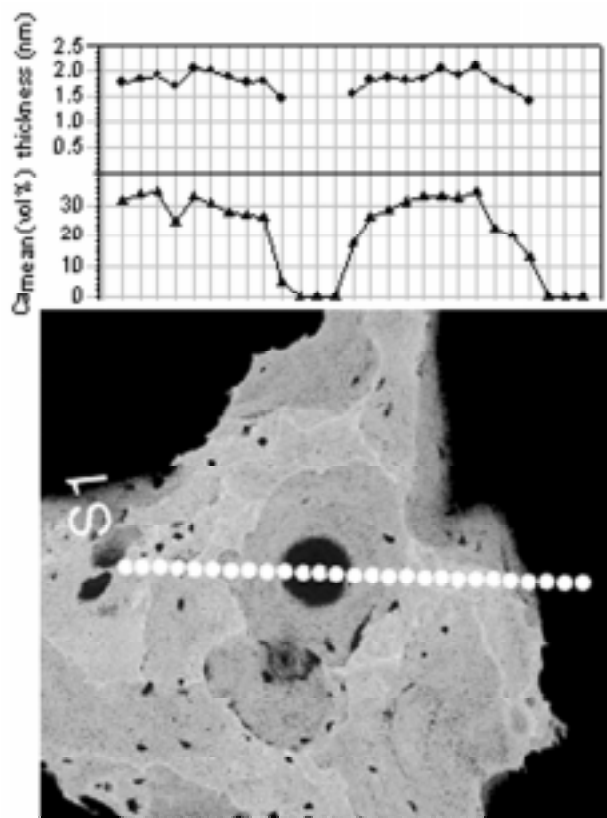


Figure 3. qBEI of pagetic bone with measurement values (thickness from SAXS and calcium content from qBEI).

grey-levels correspond to high and low mineral content. The white dots indicate positions of SAXS measurements at ELETTRA. The black hole in the middle of the picture is the lacuna of a former blood vessel, comparable to the osteon from Figure 1. As the X-ray beam was approximately 20 μm in diameter, the linescan was made with a step-width of 20 μm . The diagrams placed above the qBEI show the mean mineral thickness and the mean calcium content for each measurement point. Therefore, these results can be correlated locally to different stages of tissue maturation or diseases. In addition, using such combined images as shown in Figure 3, the results from investigation of the mineralization can be combined with previous histological studies revealing more information about the organic matrix embedding the mineralized particles.

The locally combined multimethod approach can

REFERENCES

- [1] S. Weiner and H.D. Wagner; *Ann. Rev. Mater. Sci.*; 28, 271, (1998)
- [2] I. Zizak, O. Paris, P. Roschger, S. Bernstorff, H. Amenitsch, K. Klaushofer and P. Fratzl; *ELETTRA NEWS* ; 31, (1999) (<http://www.elettra.trieste.it/science/news/volume36/EN60.html>).
- [3] I. Zizak, O. Paris, P. Roschger, S. Bernstorff, H. Amenitsch, K. Klaushofer and P. Fratzl; *J. Appl. Cryst.*; 30, 820, (2000)
- [4] O. Paris, I. Zizak, H. Lichtenegger, P. Roschger, K. Klaushofer and P. Fratzl, *Cell. Mol. Biol.*; 46, 993, (2000)
- [5] P. Fratzl, N. Fratzl-Zelman, K. Klaushofer, G. Vogl and K. Koller, *Calcif. Tissue Int.* 48, 407, (1991)
- [6] P. Fratzl, S. Scheiber and K. Klaushofer; *Conn Tissue Res*; 34, 274, (1996)

provide also new insights into the structure-function relationship of these tissues. Figure 4 shows how the thickness d (nm) of the plate-like mineral particles is correlated to the mean calcium content Ca_{mean} (vol%). For healthy bone (circles) a second order law can be found. Interestingly, although pagetic bone (triangles) does not seem to get as highly mineralized as normal bone, the correlation between the thickness and the mineral content is quite similar to the normal case. This might indicate that the basic building block, the mineralized collagen fibril, is not severely affected. In coeliac sprue (squares), however, the correlation behavior is different. It shows somewhat larger crystals at lower mineralization values and a rather linear correlation between the mineral thickness and the mineral content.

These results give important information on changes in bone material due to bone diseases. The defect in the case of the Paget's disease seems to be mostly at the microscopic level as the mineral crystal size and the correlation with the local calcium content are similar to normal bone. In contrast, in the case of coeliac sprue, the basic bone building block seems to be also altered by the disease, in addition to microstructural changes of the trabeculae (Figure 2c).

In conclusion, our studies demonstrate that the third generation synchrotron radiation sources such as ELETTRA are powerful research tool to investigate bone diseases.

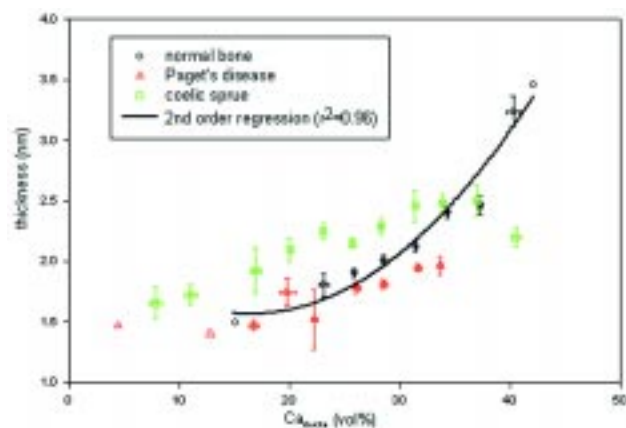


Figure 4. Correlation between mineral particles thickness (nm) and calcium content (vol %).

MAD data collection on a Hg derivative crystal of a novel pectate lyase from *Azospirillum irakense*

H. Novoa de Armas, A. Rabijns, C. Verboven, C. De Ranter

Laboratorium voor Analytische Chemie en Medicinale Fysicochemie, K. U. Leuven, E. Van Evenstraat 4, 3000 Leuven, Belgium

J. Desair, A. Vande Broeck, J. Vanderleyden

F.A Janssenslabo voor Genetica, K.U. Leuven, K. Mercierlaan 92, 3001 Leuven, Belgium

INTRODUCTION

Diseases-causing bacteria infect and spoil stored fruits and vegetables. During “soft-rot” spoilage, pectin, a major structural polysaccharide in the plant cell wall is enzymatically degraded, leading to the deterioration of fruit and vegetable tissue. Pectin is depolymerized by a combination of enzymatic activities of a group of carbohydrate-active enzymes: pectin methyl esterase, pectin acetyl esterase, pectin lyase, pectate lyase, and polygalacturonase. Lyases cleave internal glycosidic bonds via β -elimination, producing oligomers with 4,5-unsaturated residues at the non-reducing end.

Among these, the pectate lyases are the major pectinases and play a key role in the development of the soft-rot disease. Besides in phytopathogens, pectin depolymerization has also been reported in non-pathogenic plant associated bacteria such as the N_2 -fixing endosymbiont *Rhizobium* [1, 2]; and the N_2 -fixing soil bacterium *Azospirillum irakense* [3]. A gene from *A. irakense* encoding a pectate lyase (termed PelA) was isolated by heterologous expression of the gene in *Escherichia coli* [3]. Analysis of the corresponding amino acid sequence revealed no homology to other bacterial, plant and fungal pectinases leading to the classification of the enzyme in a new pectate lyase family (family 10).

Currently there are a number of pectate lyases (PelE and PelC from *Erwinia chrysanthemi*, Pel15 from *Bacillus* sp. strain KSM-P15, and PEL from *Bacillus subtilis* strain S1103) of which the crystal structure is reported in crystallographic databases [4, 5, 6], but the structure of a non-phytopathogenic pectate lyase has not yet been determined. Since *A. irakense* has never been reported to be pathogenic on plants, the structure of *A. irakense* PelA would be particularly interesting to identify potential differences with phytopathogenic pectate lyases.

Recently new members of family 10 were reported: Pel-15E from *Bacillus* sp. strain KSM-P15 [7] and Pel10A from *Pseudomonas cellulosa* [8] Pel-15E possesses some regions that are homologous to PelA with an overall 39.8% amino acid identity. The 35.8 kDa C-terminal module of Pel10A was shown to have 30 and 36% amino acid identities with PelA and Pel-15E, respectively.

Here we report the X-ray crystallographic characterization of the *A. irakense* PelA protein and preliminary structural determination results.

METHODS

The isolation and purification of PelA is reported in ref. [3]. Prior to crystallization, the protein solution was concentrated to approximately 10 mg ml⁻¹ by ultrafiltration using a Microcon concentrator (Amicon) with a 3 kDa cutoff. The initial crystallization conditions were established using sparse-matrix sampling [9] with hanging-drop vapor-diffusion geometry at 277 K, using Crystal Screens I and II (Hampton Research). A hanging drop was prepared by mixing equal volumes (2 ml each) of protein and the reservoir solution. Each hanging drop was placed over 700 μ l reservoir solutions.

Prior to flash-freezing, crystals were soaked for 30 minutes in a cryoprotectant solution consisting of the crystallization solution plus 25% glycerol. The crystals were mounted in cryo-loops and then plunged into liquid nitrogen. The cryo-loops were placed on a goniometer head and maintained at 100 K during diffraction data collection. Diffraction data for both native and heavy-atom treated crystals were collected using synchrotron light sources at EMBL-DESY (Hamburg) and ELETTRA (Trieste), respectively.

The diffraction data of the native crystals were

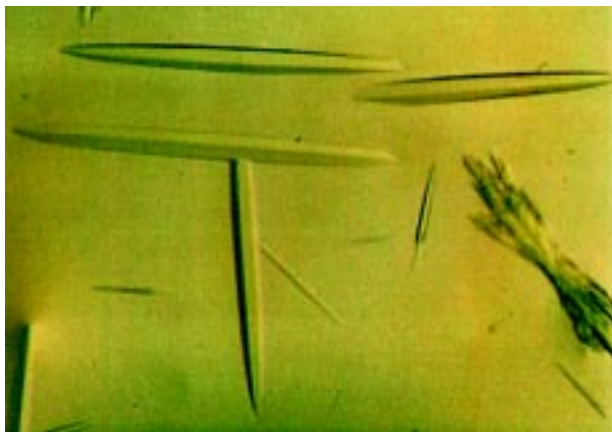


Fig. 1. Hexagonal crystals of *Azospirillum irakense* PelA.

collected using a MAR 345 imaging-plate detector. The three-wavelengths MAD data set on the heavy-atom (Hg) soaked crystal was collected using a MAR CCD 165 mm detector. The *DENZO* and *SCALEPACK* packages [10] were used for the determination of the unit cell parameters, data indexing, reduction and scaling. Patterson maps were initially generated with routine *MAPVIEW* of the *PHASES* program [11]. The program *SHARP* [12] was used to confirm and refine heavy-atoms sites as well as to find possible additional sites and the program *O* [13] was used for model building.

RESULTS AND DISCUSSION

Initially, two different types of crystals were obtained from 5 % *iso*-propanol and 2.0 M ammonium sulfate (type I) and 20% *iso*-propanol, 20% PEG 4000 and 0.1 M citrate pH 5.6 (type II), respectively. Further improvement of type II crystals to 15 % *iso*-propanol, 0.1 M imidazole pH 7.8 and a

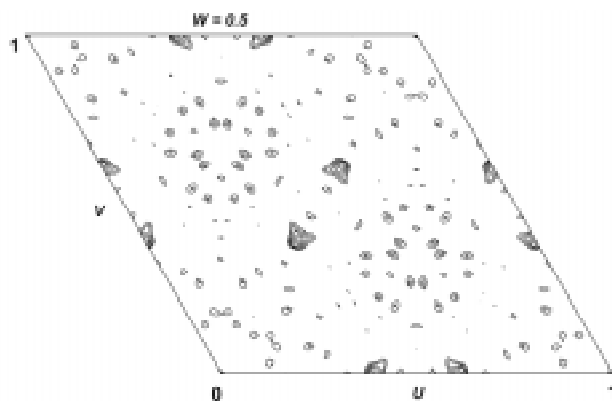


Fig. 2. Anomalous Patterson map for the ethylmercury phosphate derivative of PelA.

2:1 ratio of protein: reservoir-solution in the hanging drop gave rod-shaped (type III) crystals (Fig. 1) with approximate dimensions of 0.6 x 0.1 x 0.1 mm. These crystals are hexagonal with cell dimensions of $a = b = 85.55 \text{ \AA}$, $c = 230.13 \text{ \AA}$, $\gamma = 120^\circ$. They diffract to 1.9 \AA and a complete data set to 1.97 \AA was collected at the DESY BW7B beamline (Hamburg). From the symmetry of the intensity-weighted reciprocal lattice and systematically absent reflections (the absence of $00l$ reflections for $l \neq 6n$), the possible space groups were $P6_122$ and $P6_522$. Using the Matthews formula [14], one molecule in the asymmetric unit and a water content of 56% were predicted. Heavy-atom derivative screening identified a mercury isomorphous derivative when type III native PelA crystals were soaked in 0.5 mM ethylmercury phosphate for 24 hours and the heavy atom salt solution was prepared with 0.2 M lithium sulfate instead of 0.2 M ammonium sulfate. From the collected data set on such a Hg derivative crystal it was possible to locate one Hg site in the anomalous Patterson map (Fig. 2) and to refine this site (isomorphous and anomalous phasing powers after refinement were 2.53 and 1.19, respectively) to 2.6 \AA resolution. Structure determination using the MAD method [15] is presently underway on a three wavelengths data set collected in the ELETTRA XRD 1 beamline. The statistics for this MAD data set are also shown in Table 1. From the inspection of the handedness of the α -helices in the electron density maps obtained it was possible to establish unambiguously the right enantiomorph: $P6_522$. The electron density maps (Fig.3) show that the structure of PelA does not follow the characteristic parallel b-helix fold of the pectate lyase structures currently present in the PDB. This novel structure will provide detailed three-dimensional knowledge of this most recently discovered family of lyase, leading to the identification of key residues in substrate binding and the lyase catalytic mechanism.

ACKNOWLEDGMENTS

H. N. de Armas wants to thank the K.U.Leuven, Belgium, for an IRO scholarship. A. Rabijns is a Postdoctoral Research Fellow of the Fund for Scientific Research-Flanders (Belgium). C. Veerboven is a Postdoctoral Research Fellow of the K.U.Leuven Research Fund (OT/98/38). Walter Jottier is acknowledged for technical assistance during in house preliminary data collection. We acknowledge the support of the protein crystallography project team at the EMBL BW7B beam line at DORIS storage ring, DESY, Hamburg, and the staff of the XRD1 beamline, ELETTRA, Tri-

este. The European Union is acknowledged for supporting the work at EMBL Hamburg (HCMP to Large Installations Projects, contract No. CHGE-CT93-0040) and at ELETTRA (Human Potential Programme Transnational Access to Major Research Infrastructures, contract No. HPRI-CT-1999-00033).

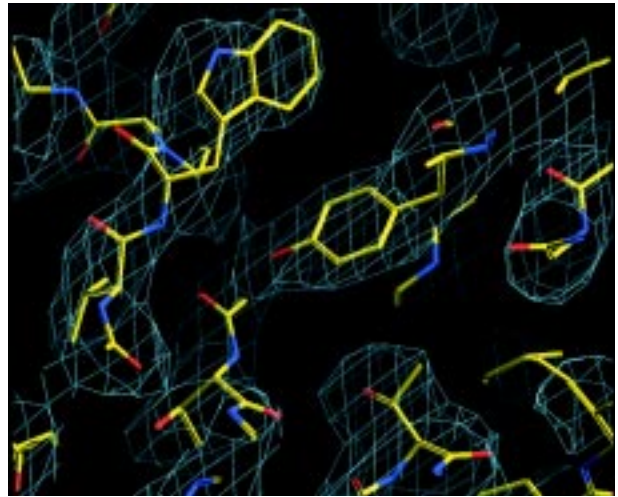


Fig. 3. PeIA model superimposed on its electron density.

Native PeIA crystal soaked in ethylmercury phosphate	
Crystal system	Hexagonal
Space group	$P6_522$
Unit-Cell parameters (Å, °)	$a = b = 86.113, c = 230.339 \text{ Å}, \gamma = 120^\circ$
λ_1 (Å), λ_2 (Å), λ_3 (Å)	0.918407, 0.991880 (reference), 1.010719
Resolution (Å)	2.65
Completeness (%)	$\lambda_1 = 97.3$ (98.3), $\lambda_2 = 100$ (99.9), $\lambda_3 = 98.1$ (98.1)
R for dispersive differences	$\lambda_3 - \lambda_1 = 0.070, \lambda_3 - \lambda_2 = 0.06$
R for anomalous differences	$\lambda_1 = 0.033, \lambda_2 = 0.039, \lambda_3 = 0.055$
Overall figure of merit for MAD phasing (before density modification)	0.44 (0.5-2.6 Å)

$R_{merge} = 100 \sum_h \sum_i (|F_{hi}^2 - \langle F_{hi}^2 \rangle|) / \sum_h \sum_i F_{hi}^2$, where F_{hi}^2 is the square of the i th intensity measurement of reflection h and $\langle F_{hi}^2 \rangle$ is the mean-squared intensity of the reflection. Values in parentheses refer to the highest resolution shell

Table 1. Synchrotron data collection statistics for the MAD phasing of the Hg derivative.

REFERENCES

- [1] Mateos, P.F., Jimenez-Zurdo, J.I., Chen, J., Squartini, A.S., Haack, S.K., Matínez-Molina, E., Hubbell, D.H. & Dazzo, F.B. (1992). *Appl. Environ. Microbiol.* 58, 1816-1822.
- [2] Hubbell, D.H., Morales, V.H. & Umali-García, M. (1978). *Appl. Environ. Microbiol.* 35, 210-213.
- [3] Bekri, M.A., Desair, J., Keijers, V., Proost, P., Searle-van Leeuwen, M., Vanderleyden, J. & VandeBroeck, A. (1999). *J. Bacteriol.* 181, 2440-2447.
- [4] Jenkins, J., Mayans, O., & Pickersgill, R. (1998). *J. Struct. Biol.* 122, 236-246.
- [5] Akita, M., Suzuki, A., Kobayashi, T., Ito, S. & Yamane, T. (2000). *Acta Cryst. D* 56, 749-750.
- [6] Pickersgill, R., Harris, G., Jenkins, J. (1994). *Nat Struct Biol.* 1(10), 717-723.
- [7] Sawada, K., Ogawa, A., Ozawa, T., Sumitomo, N., Hatada, Y., Kobazyashi, T. & Ito, S. (2000). *Eur. J. Biochem.* 267, 1510-1515.
- [8] Brown, I.E., Mallen, M.H., Charnock, S.J., Davies, G.J. & Black, G.W. (2001). *Biochem. J.* 355, 155-165.
- [9] Jancarik, J. & Kim, S. H. (1991). *J. Appl. Cryst.* 24, 409-411.
- [10] Otwinowski, Z. & Minor, W. (1997). *Methods Enzymol.* 276, 307-326.
- [11] Furey, W. & Swaminathan, S. (1990). *Am. Crystallogr. Assoc. Meet. Abstr.* 18 (PA33), 73.
- [12] de La Fortelle, E. & Bricogne, G. (1997). *Methods Enzymol.* 276, 472-494.
- [13] Jones, T.A., Zhou, J.Y., Cowan, S. & Kjeldgaard, M. (1991). *Acta Cryst. A* 47, 110-119.
- [14] Matthews, B.W. (1968). *J. Mol. Biol.* 33, 491-497.
- [15] Hendrickson, W. A. (1991). *Science* 254, 51-58.

Glyceraldehyde-3-phosphate dehydrogenases from chloroplasts

S. Fermani, A. Ripamonti, P. Sabatino

Dipartimento di Chimica “G. Ciamician”, Università di Bologna, via Selmi 2, 40126 Bologna, Italia

G. Zanotti

Centro di Studi sui Biopolimeri, Dipartimento di Chimica Organica, Università di Padova, via Marzolo 1, Padova, Italia

S. Scagliarini, P. Trost, P. Pupillo

Laboratorio di Fisiologia Vegetale, Dipartimento di Biologia, Università di Bologna, via Irnerio 42, 40126 Bologna, Italia

INTRODUCTION

Glyceraldehyde-3-phosphate dehydrogenases (GAPDH) are ubiquitous enzymes uniformly involved in glycolysis and gluconeogenesis and in the carbon reduction cycle of photosynthetic organisms. Photosynthetic GAPDHs of cyanobacteria, algae and higher plants recognize both NAD (nicotinamide adenine dinucleotide) and NADP (nicotinamide adenine dinucleotide phosphate) with a preference toward NADP. These latter GAPDHs are chloroplast-located and made up of either one type (A) or two types (A and B) of subunits [1]. Subunit A (36 kDa) and B (39 kDa) of chloroplast GAPDHs are homologous and highly conserved, except for the C-terminal extension of subunit B which includes 31 residues absent in subunit A. Two GAPDH isoforms have been observed in chloroplasts of higher plants. The major isoform contains subunits A and B in stoichiometric amounts. The second isoform of chloroplast GAPDH is a homotetramer of A-subunits. Although recombinant A₄-GAPDH can be obtained from *E. coli* cells transformed with the coding sequence for spinach subunit A, the existence of such A₄-isoform *in planta* has long been questioned [2]. The C-terminal extension of subunits B of A₂B₂ isoforms is actually very sensitive to proteolytic cleavage and the resulting truncated B-subunits may be taken for subunits A because of their similar electrophoretic mobility [3].

Here we present the crystal structures of the A₄ isoform of spinach chloroplast GAPDH complexed with NADP, of the regulative A₂B₂ isoform and of the recombinant A₄ form complexed with NAD.

METHODS

The A₄ and A₂B₂ isoforms of GAPDH have been purified to homogeneity from spinach chloroplasts.

Crystals of both forms were grown in the presence of NADP, using the hanging drop technique from (NH₄)₂SO₄ 1.5 M, with 0.1 M Tris pH 8.5 for A₄ and 0.1M KPi pH 7.5 for A₂B₂ from 10mg/ml protein solutions [4]. The recombinant form of A₄ isoform has been overexpressed from *E. coli* and complexed with NAD. Crystals were grown from (NH₄)₂SO₄ 0.8 M, with 0.1M Tris pH 7.5 from a 20mg/ml protein solution. X-ray diffraction data for the three species are given in Table 1. For data collection crystals were soaked for a few minutes in different solutions containing 1.5 M (NH₄)₂SO₄, 1 mM NADP and glycerol as cryoprotectant, starting from a glycerol concentration of 10% (v/v) to the final concentration of 40% (v/v). Data collections under cryogenic conditions were performed at the ELETTRA X-ray diffraction beamline.

The A₄ crystal structure was solved by molecular replacement using the coordinates of a mutated form of the holo wild-type GAPDH from *B. stearothermophilus* as a template, because of their high sequence homology (58,9 %). The results of rotation and translation searches showed the presence of three subunits in the asymmetric unit with a solvent content of about 62%. One of the three monomers generates a tetramer using the space group 222 point symmetry and a very similar tetramer is generated by the other two monomers, related by a non-crystallographic symmetry, using a crystallographic 2-fold axis. After refinement reached an R_{factor} of 22% and an R_{free} of 33%, the electron density maps revealed unambiguously the positions of the cofactor in each subunit. Finally, water molecules and two sulphate ions for each monomer were added to the model according to the electron density maps. The final model shows a crystallographic R factor of 21.3% for all data without s cut-off and an R_{free} of 25.4%.

Data of A₂B₂ isoform revealed to be isomorphous with that of A₄, containing three subunits in the

	A_4	A_2B_2	A_4 - NAD
Cell parameters (Å)	a = 145.9 b = 185.9 c = 106.3	a = 145.32 b = 185.32 c = 106.53	a = 140.82 b = 185.98 c = 105.70
Space group	C222	C222	C222
$V_{\text{unit cell}}$	2883155	2868928	2794441
V_M	3.33	3.11	3.35
Radiation wavelength (Å)	1.0	1.0	1.0
Detector	MAR345	MAR345	MAR- CCD
Temperature	100K	100K	100K
Max. resolution (Å)	3.0	2.8	2.6
Resolution data set (Å)	69 – 3.0	31.5 – 2.8	91 – 2.6
Measurements	507391	869072	982348
Unique reflections	28763	34807	36646
R_{symm}	0.133	0.121	0.067
Completeness (%)	93.1	97.8	98.2
R factor	0.21	0.25	0.258
R_{free}^*	0.25	0.30	0.304

Table 1. X-ray diffraction data.

* R_{free} calculated by randomly omitting 5% of the observed reflections from refinement

asymmetric unit. In the present case, the first monomer generates an A_4 tetramer, while the other two consist of one A and one B subunit generating an A_2B_2 tetramer *via* the crystallographic 2-fold axis. B subunits appear to be truncated, with no significant density present after C337. Thus, crystals contain the two different isoforms together, with the B subunits truncated probably due to a proteolytic cleavage occurred during crystallization. Model refinement is currently in progress.

Data of the recombinant A_4 -NAD show a perfect isomorphism with the data from A_4 -GAPDH complexed with NADP. The structure was solved by molecular replacement and the model refinement is still in progress.

RESULTS AND DISCUSSION

The A_4 isoform purified from spinach chloroplasts represents the simplest possible arrangement of photosynthetic GAPDH, being constituted of a single type of 36 kDa subunits assembled as tetramers (Fig. 1). Like any photosynthetic GAPDH, the A_4 isoform

shows double specificity toward NADP and NAD, although NADP is the preferred coenzyme [1].

As all other GAPDHs investigated so far, also the A_4 -GAPDH belongs to the Rossmann fold family [5] of dehydrogenases. The overall structure of spinach chloroplast A_4 -GAPDH is found to be basically similar to non-photosynthetic GAPDHs. In particular, each subunit of the tetramer comprises two domains: an NAD(P)-binding domain with a typical Rossmann folding, and a catalytic domain (Fig. 2). However, unlike most dehydrogenases of this family, the adenosine 2'-phosphate group of NADP does not form a salt bridge with any positively charged residue in its surroundings, being instead set in place by hydrogen bonds with a threonine belonging to the Rossmann fold and a serine located in the S-loop of a symmetry related monomer (Fig. 3). Finally, this study has highlighted the presence of a disulphide bridge between two symmetry related subunits, apparently a peculiar feature of A_4 -GAPDH from spinach chloroplasts [6]. The presence of this extra bond in spinach A_4 -GAPDH may conceivably be related to the relative stability of this chloroplast enzyme, which makes it an ideal source for structural

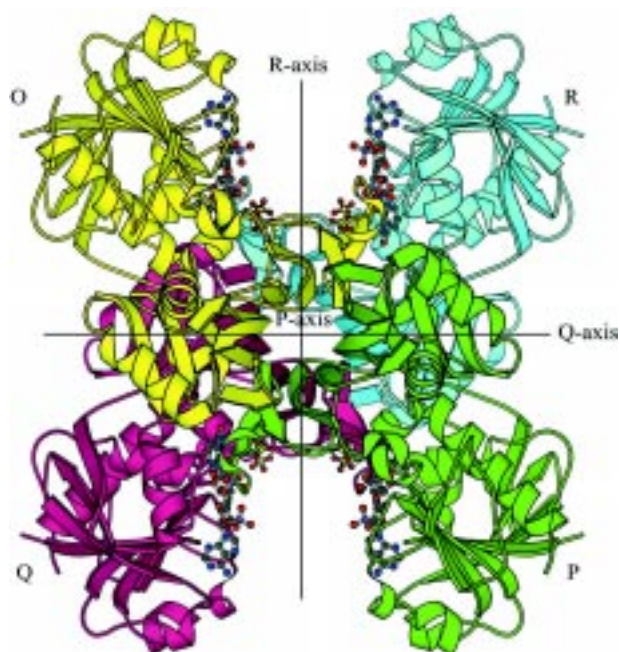


Figure 1. Ribbon model and nomenclature of the chloroplast GAPDH tetramer viewed along molecular axis P.

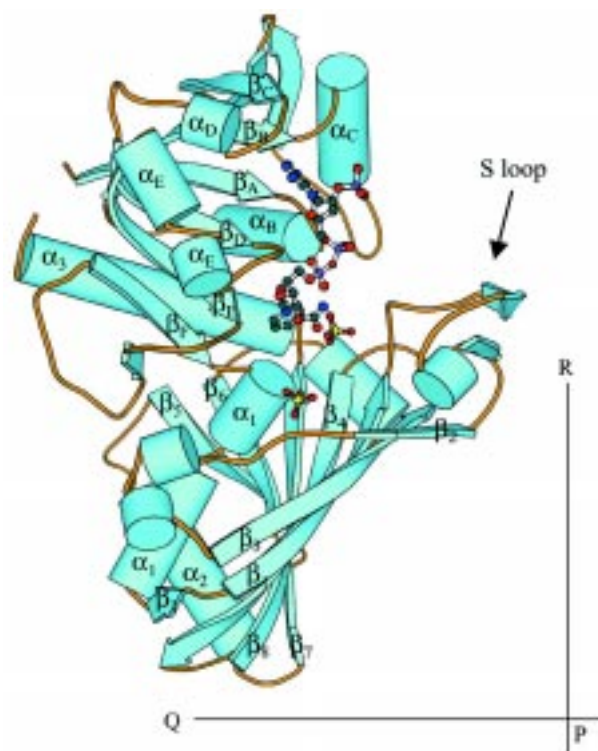


Figure 2. Localization of secondary structures in the A monomer of chloroplast GAPDHs. All the secondary structures with letter subscripts plus α_3 form the coenzyme-binding domain implies.

studies with respect to other plant sources.

The second isoform investigated, A_2B_2 , is in fact a co-crystallization of A_4 and A_2B_2 isoforms containing truncated B subunits. Identification of the B subunit, besides the sequence differences, is easily confirmed by the absence of the cysteine residue at position 200 and, therefore, the absence of the disulfide bridge which seems to be the fingerprint of the spinach A subunits. In fact Cys200 is replaced by an alanine in the B subunit of the regulative isoform of spinach GAPDH as well as in the A subunits of several GAPDHs from other plant species. Similarly, in cytosolic GAPDHs from eubacteria and eukaryotes, a cysteine is never found in this or a comparable position. As for the C-terminal extension, we cannot rule out the possibility that it is present but highly disordered, as is often the case for regulative domains.

The investigation of the crystal structure of the recombinant A_4 isoform complexed with NAD has been carried out to clarify the reasons for the cofactor specificity. The discrimination between

NAD and NADP depends mainly on the adenosine phosphate group of NADP, whereas in NAD the same position is occupied by a hydroxyl group, which acts as proton donor. Since the chemical environment and the steric hindrance are really different, the coenzyme specificity can not be determined by only the primary structure of the protein, but also depends on the three-dimensional arrangement of the residues involved in the cofactor interactions. In NAD-dependent oxidoreductases belonging to the Rossmann fold family it has been proposed that the presence of an acidic residue (often aspartate) discriminates the cofactor specificity for NAD by chelating the diol groups in positions 2' and 3' of the adenine ribose, at the same time preventing NADP binding due to electrostatic repulsion. While in A_4 -NADP Asp32 has its side chain directed away from the 2'-phosphate of NADP and is hydrogen-bonded to a water molecule, when the enzyme is complexed with NAD the Asp32 moves toward the ribose ring to stabilize the hydroxyl groups and the water molecule is not present.

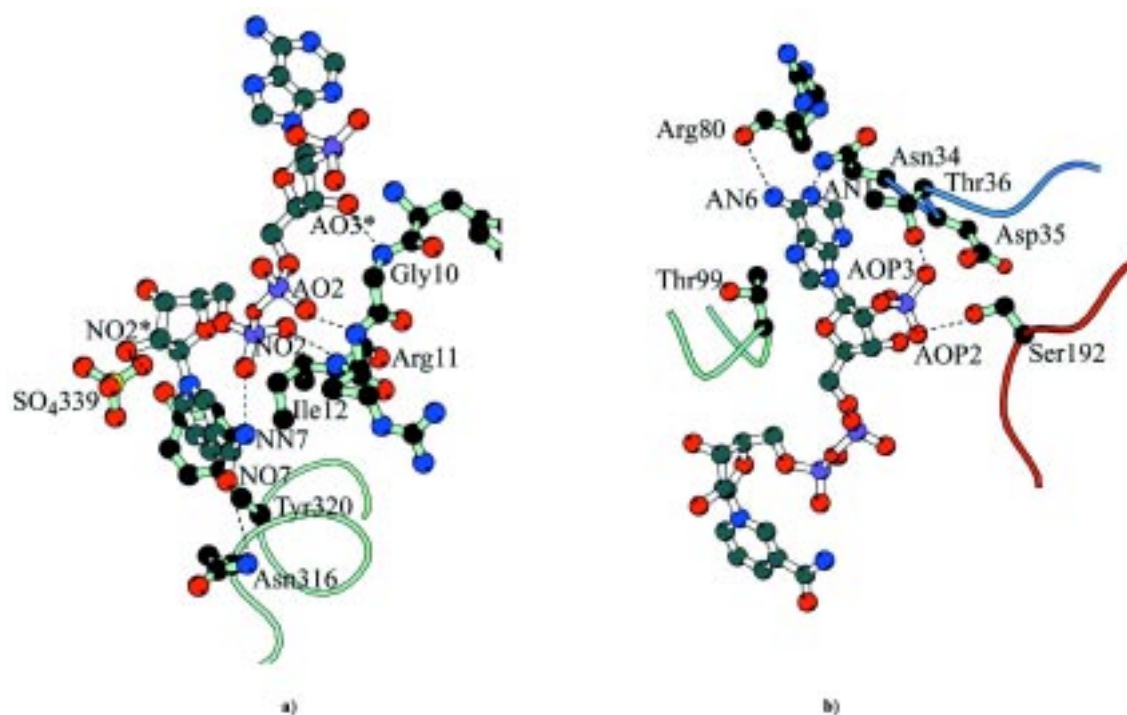


Figure 3. Shortest contacts between NADP and the A_4 protein atoms a) in the nicotinamide and diphosphate regions and b) in the 2'-phosphate and adenine ring moiety. Atom colour code: black: carbon, blue: nitrogen, red: oxygen, purple: phosphorous, yellow: sulphur.

REFERENCES

- [1] G. Ferri, M. Stoppini, M. Meloni, M. C. Zapponi and P. Iadarola; *Biochim. Biophys. Acta* 1041, 36, (1990); S. Scagliarini, P. Trost and P. Pupillo; *J. Exp. Bot.* 49, 1307, (1998).
- [2] E. Baalman, R. Scheibe, R. Cerff and W. Martin; *Plant Mol. Biol.* 32, 505, (1996)
- [3] R. Scheibe, E. Baalman, J. E. Backhausen, C. Rack and S. Vetter; *Biochimica et Biophysica Acta* 1296, 228, (1996); M. C. Zapponi, P. Iadarola, M. Stoppini and G. Ferri; *Biol. Chem. Hoppe-Seyler*, 374, 395, (1993).
- [4] P. Sabatino, S. Fermani, A. Ripamonti, A. Cassetta, S. Scagliarini and P. Trost; *Acta Cryst. D* 55, 566, (1999).
- [5] C. Branden, J. Tooze, *Introduction to protein structure*, Garland Publishing Inc., New York and London, (1999)
- [6] S. Fermani, A. Ripamonti, P. Sabatino, G. Zanotti, S. Scagliarini, F. Sparla, P. Trost and P. Pupillo *J. Molecular Biology*, in press (2001).

Use of soft X-ray in phasing of

M. Polentarutti, K. Djinovic-Carugo

Structural Biology Laboratory - Sincrotrone Trieste in AREA Science Park, Italy

Calculation of electron density image of a macromolecule requires the knowledge of phase for each diffracted X-ray wave. For the *de novo* phasing of macromolecular structures two principal techniques are employed: multiple isomorphous replacement (MIR) and multiwavelength anomalous dispersion (MAD). In case of more conventional MIR approach data sets are collected at the same single wavelength from native and different heavy-atom derivatives of the crystal. MAD approach on the other hand takes the advantage of energy dependence of X-ray scattering, since anomalous scatterers have different atomic scattering factors at different wavelength, which gives rise to variation in diffraction intensities. In a MAD experiment the diffraction data are therefore measured at several different wavelengths chosen in vicinity of the absorption edge of a certain anomalous scatterer present in the crystal.

MAD is now widely used for structural analysis of biological macromolecules. Nevertheless it has been argued that the collection of a single wavelength dataset at the absorption edge, in combination with solvent flattening techniques would be sufficient for solving the phase problem. Such an approach, termed single wavelength anomalous scattering (SAS or SAD) can be considered as a time efficient alternative to MAD techniques.

Experiments which take advantage of anomalous signal for phasing have been carried out on many different anomalous scatterers over a wide range of energies from Fe K edge (7.1 keV) to uranium LIII edge (17.2 keV). They include two types of absorption edges, the LIII and LII edges of heavier elements (e.g. Hg, Pt, Yb), many of which are also commonly used for MIR derivatives, and the K edges of lighter elements (e.g. Se, Fe).

In the last decade the interest in the use of soft X-rays in macromolecular crystallography has been continuously growing. Collection of anomalous diffraction data at the M edge of the very heavy elements such as uranium would give

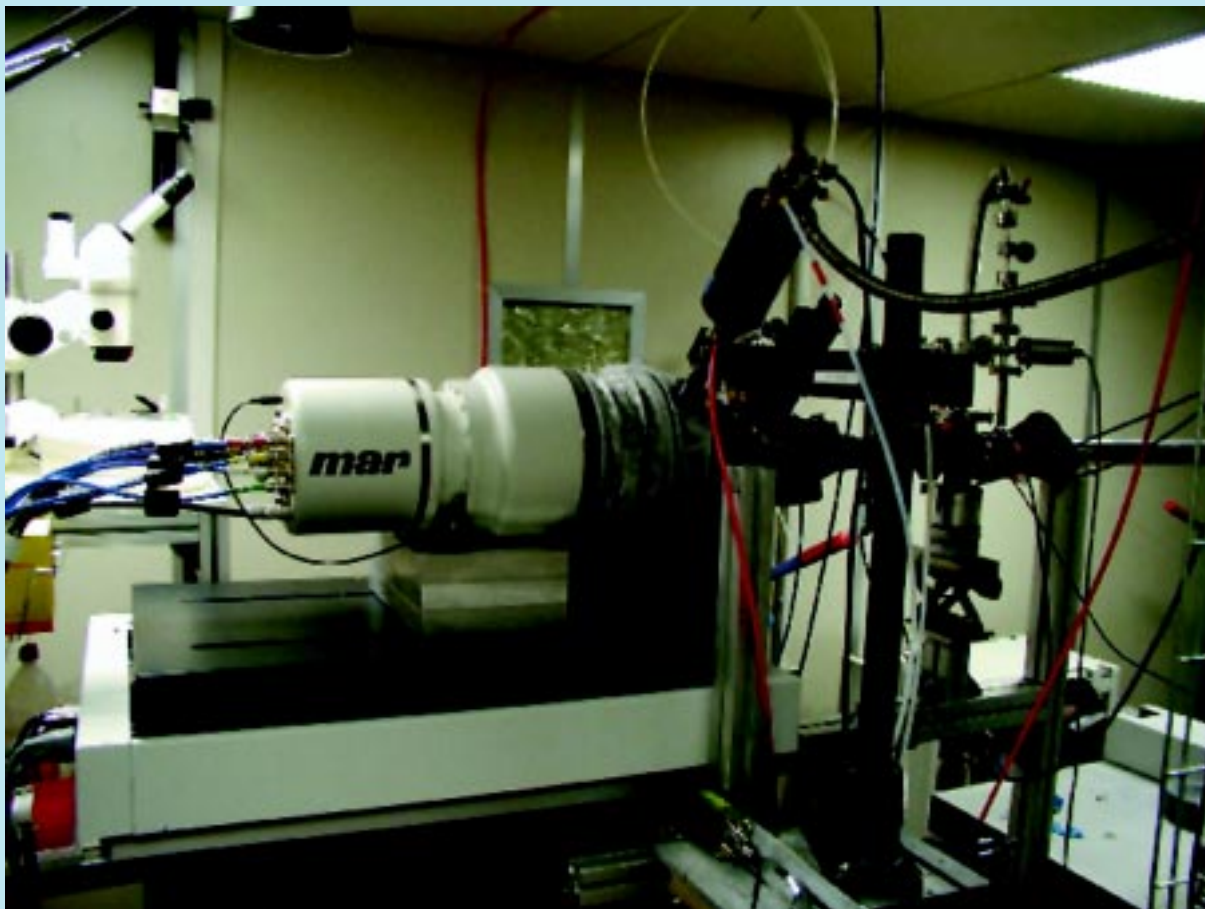
a very large signal for phase determination based on anomalous diffraction intensity differences ($\Delta f''$ at uranium Mv edge - 3.5 Å is 110 e) due to an intense white line.

The LIII edge of xenon at a wavelength of about 2.6 Å with a $\Delta f''$ of about 11 e⁻ offers another promising application, while K edge of xenon at about 0.3 Å is out of reach for most synchrotron sources. Another important application of soft X-rays in biological crystallography is centered around the enhancement of the anomalous signal of sulfur and phosphorus and the use of these elements as markers in macromolecular structure determination or the use of the enhanced anomalous sulfur signal in single wavelength anomalous scattering (SAS) experiments for phase determination.

Recent pilot experiments with soft X-rays at XRD1 beamline demonstrated that longer wavelengths can routinely be used in macromolecular crystallography. In order to make sulfur SAS approach generally applicable it is necessary to increase the weak anomalous signal and the accuracy of the data. One of the experimental concerns on data collection at long wavelengths is the absorption effect on the primary and secondary beam. It is therefore essential that suitable scaling protocols are used, combined with experimental set-up which diminishes absorption of X-rays in air. A helium purged beam-path (Figure) was therefore developed, spanning from the kapton window of the beamline to the CCD detector. This set-up combined with cooling system based on helium (at 100K) allows to keep the sample, primary and secondary beams in helium atmosphere, therefore substantially reducing absorption effects which are prominent at these wavelengths.

In the light of upcoming structural genomics projects undertaken worldwide, this approach is likely to become one of the standard phasing tools for nearly completely automated protein structure determination.

biological macromolecules



Helium purged beam path at XRD1 beamline.

REFERENCES

- Bond CS, Shaw MP, Alpey MS, Hunter WN.
Structure of the macrocycle thioestrepton solved using the anomalous dispersion contribution of sulfur.
Acta Crystallogr D Biol Crystallogr. 2001, 57, 755-8.
- Cianci M, Rizkallah PJ, Olczak A, Raftery J, Chayen NE, Zagalsky PF, Helliwell JR.
Structure of lobster apocrustacyanin A1 using softer X-rays.
Acta Crystallogr D Biol Crystallogr. 2001, 57, 1219-29.
- Dauter Z, Dauter M, de La Fortelle E, Bricogne G, Sheldrick GM.
Can anomalous signal of sulfur become a tool for solving protein crystal structures?
J Mol Biol. 1999, 28, 93-101.
- Gordon EJ, Leonard GA, McSweeney S, Zagalsky PF.
The C1 subunit of alpha-crustacyanin: the de novo phasing of the crystal structure of a 40 kDa homodimeric protein using the anomalous scattering from S atoms combined with direct methods.
Acta Crystallogr D Biol Crystallogr. 2001, 57, 1230-7.
- Liu Y, Ogata CM, Hendrickson WA.
Multiwavelength anomalous diffraction analysis at the M absorption edges of uranium.
Proc Natl Acad Sci U S A. 2001, 98, 10648-53.
- Weiss MS, Sicker T, Hilgenfeld R.
Soft X-rays, High Redundancy, and Proper Scaling. A New Procedure for Automated Protein Structure Determination via SAS.
Structure 2001, 9, 771-7.
- Weiss MS, Sicker T, Djinovic-Carugo K, Hilgenfeld R.
On the routine use of soft X-rays in macromolecular crystallography.
Acta Crystallogr D Biol Crystallogr. 2001, 57, 689-95.

A New Procedure for Automated Protein Structure Determination involving the use of soft X-rays

M. S. Weiss

Institute of Molecular Biotechnology, Department of Structural Biology and Crystallography, Beutenbergstr. 11, D-07745 Jena, Germany

Since 1.10.2001: EMBL Hamburg Outstation, c/o DESY, Notkestr. 85, D-22603 Hamburg, Germany

T. Sicker, R. Hilgenfeld

Institute of Molecular Biotechnology, Department of Structural Biology and Crystallography, Beutenbergstr. 11, D-07745 Jena, Germany

INTRODUCTION

In the past decade, the multiple wavelength anomalous dispersion (MAD) technique [1] has become the method of choice for determining the three-dimensional structure of a novel protein. Nevertheless, the single-wavelength anomalous scattering (SAS, sometimes also called SAD) approach, originally proposed by Wang [2], has recently been the subject of a number of discussions at crystallographic conferences and in publications as well. It is a more time-efficient alternative to a complete MAD analysis but has the inherent disadvantage that it fails to yield a unimodal phase probability distribution. In order to resolve the resulting phase ambiguity, it is therefore necessary to combine the SAS approach with density modification or other techniques.

Here we describe a method which exploits the weak anomalous signal present in the native protein crystal (provided by P, S, Cl⁻, K⁺, Ca²⁺, etc.). This is potentially very interesting because an average protein contains 4.2 S-atoms per 100 amino acids [3]. If the anomalous signal provided by these atoms turned out to be sufficient for phase determination, the preparation of selenomethionine proteins would cease to be a requirement for all but the larger polypeptides, or their complexes.

Our method is based on three major pillars: a) the use of soft X-rays in the wavelength range $\lambda = 1.5 - 3.0 \text{ \AA}$; b) the collection of highly redundant diffraction data; c) a suitable scaling protocol.

By collecting diffraction data at longer wavelengths, the weak anomalous signal present in the native protein crystal can be significantly enhanced so that the phasing power provided by the anomalous differences obtained in a SAS experiment

is sufficiently large to yield an interpretable electron density map. The very high redundancy (20 or higher for averaged intensities) of the collected diffraction data leads to very accurate anomalous differences and to small errors in these differences. Due to the absorption effects encountered, it is essential that a three-dimensional scaling model be employed, as we have shown in [4].

This approach was tested on hexagonal crystals of the Zn-metalloprotease thermolysin (316 amino acid residues, $M_r = 34.7 \text{ kDa}$). The structure contains three sulfur atoms (Met120, Met205, DMSO), five calcium ions and one zinc ion.

METHODS

Five data sets were collected at $\lambda = 1.5 \text{ \AA}$, 1.7 \AA , 1.9 \AA , 2.1 \AA and 2.64 \AA at the X-ray diffraction beamline of ELETTRA (Table 1). All five data sets were of very high redundancy and all of them were scaled using a 3D-scaling model to correct for absorption errors. The magnitude of the anomalous differences described by the anomalous R-factor R_{anom} was between 1.3% and 2.8%.

RESULTS AND DISCUSSION

An anomalous difference Patterson showing the peaks for all calcium and one of the sulfur atoms in the structure is shown in Figure 1. Due to the small errors in the averaged intensities (as described by the precision-indicating merging R-factor R_{pim} [5]) and in the anomalous differences, it was possible to determine the complete anomalous substructure [6] using the program Shake-and-Bake [7]. The largest

data set	A	B	C	D	E
used wavelength in Å	1.50	1.70	1.90	2.10	2.64
rotation range in °	360	360	360	360	360
detector distance in mm	70	55	40	40	40
resolution in Å	1.83	1.83	1.82	2.01	2.52
redundancy	40.4	39.6	36.7	34.9	35.0
completeness in %	100.0	99.9	100.0	100.0	100.0
R _{rim}	5.4	4.2	4.0	6.3	6.3
R _{pim}	0.8	0.6	0.6	1.0	1.0
R _{anom}	1.3	1.4	1.7	2.0	2.8

Table 1. Data collection and processing statistics

number of successful trials in this respect was achieved with the data collected at $\lambda = 1.9 \text{ \AA}$. At the longer wavelengths, the increase of the anomalous signal is probably counterbalanced by increased errors due to absorption which could not be fully compensated for by the use of the scaling protocol.

After calculation of the phases and solvent flattening, interpretable electron density maps were obtained. Correlation coefficients between SAS-phased and solvent-flattened electron density maps and the final $2F_{\text{obs}} - F_{\text{calc}}$ maps (after refinement) are shown in Figure 2. Again, the best results were obtained with the data set collected at $\lambda = 1.9 \text{ \AA}$. Furthermore, in the cases in which the resolution extended to about 2.0 \AA or better, the structure could be built completely automatically using the Arp/wArp procedure [8].

The described approach requires only modestly high resolution data; it should therefore be applicable to a wide range of protein crystals which contain up to 35 kDa (or maybe even more) in their asymmetric unit. Especially in the light of all the emerging structural genomics projects, it may have the potential to become one of the standard approaches for nearly completely automated protein structure determination.

REFERENCES

- [1] Hendrickson, W.A. and Ogata, C.M., *Methods Enzymol.* 276, 494-522 (1997).
- [2] Wang, B.-C., *Methods Enzymol.* 115, 90-112 (1985).
- [3] McCaldon, P. and Argos, P., *Proteins* 4, 99-122 (1988).
- [4] Weiss, M.S., Sicker, T., Djinovic-Carugo, K. and Hilgenfeld, R., *Acta Crystallogr. D* 57, 689-695 (2001).
- [5] Weiss, M.S., *J. Appl. Crystallogr.* 34, 130-135 (2001).
- [6] Weiss, M.S., Sicker, T. and Hilgenfeld, R., *Structure* 9, 771-777 (2001).
- [7] Weeks, C.M. and Miller, M., *J. Appl. Crystallogr.* 32, 120-124 (1999).
- [8] Perrakis, A., Morris, R. and Lamzin, V. *Nature Struct. Biol.* 6, 458-463 (1999).

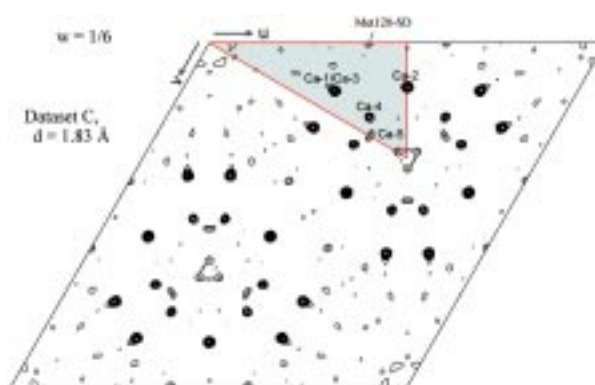


Figure 1. Anomalous difference Patterson map for data set C ($\lambda = 1.9 \text{ \AA}$) at a resolution of $d = 1.83 \text{ \AA}$. The peaks shown are for the calcium ions Ca-2 (on a special position), Ca-1/3 (same x and y-coordinates), Ca-4 and Ca-5 (not fully occupied) as well as for the sulfur atom of Met120. The zinc ion of the active site and the two other sulfur atoms of the structure do not appear as peaks in this synthesis.

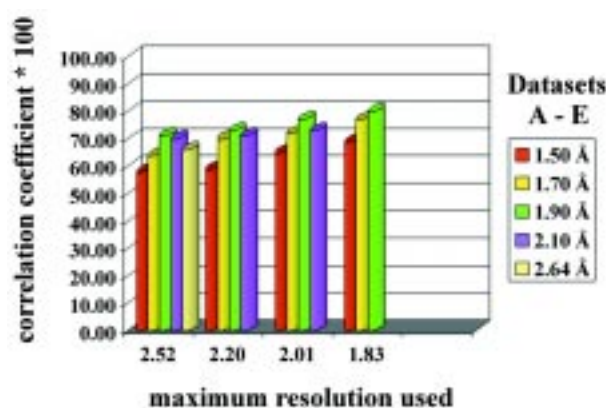


Figure 2. Correlation coefficients between SAS-phased and solvent-flattened electron density maps and the final $2F_{\text{obs}} - F_{\text{calc}}$ maps (after refinement) for the five data sets processed at four different resolutions (1.83 \AA , 2.01 \AA , 2.20 \AA and 2.52 \AA).

In Situ-SAXS Investigations on Zinc Sulphide Precipitation in a Liquid Jet on a Microsecond Time Scale

P. Bussian, W. Schmidt, F. Schüth

Max-Planck-Institut für Kohlenforschung, Kaiser-Wilhelm-Platz 1, D-45470 Mülheim/Ruhr, Germany

P. Ågren

Vaisala Oyj, P.O. Box 26, FIN-00421 Helsinki, Finland

J. Andersson, M. Lindén

Department of Physical Chemistry, Åbo Akademi University, Porthansgatan 3-5, FIN-20500 Turku, Finland

H. Amenitsch

Institute of Biophysics and X-ray Structure Research, Austrian Academy of Sciences, Schieldstr. 6, A-8042 Graz, Austria

INTRODUCTION

In solid state chemistry the analysis and understanding of nucleation from solution is one of the most challenging problems. Simultaneously, it is a highly rewarding task for the so-called tailoring of materials and their properties. However, especially for very fast precipitation reactions only very few techniques are available for analysis of these reactions. In principle two methodologies could be used. On the one hand, the pre-nucleation state in solution with ever increasing oligomer size can be analyzed, which has recently been done in our group with mass spectrometric methods [1]. On the other hand, it is possible to investigate the already formed solid (post-nucleation state) with ever decreasing particle size. The latter method for analysis has been chosen to investigate the precipitation of sparingly soluble sulphides as a model system with small angle X-ray scattering (SAXS). In combination with a tubular reactor set-up SAXS can give new insights in the very early stages of precipitation reactions on a microsecond time scale.

The tubular reactor is a versatile tool for the study of very fast precipitation reactions even with slow analytical techniques. Surprisingly, to the best of our knowledge the tubular reactor set-up has only been used by us [2, 3, 4,] and two other groups [5, 6] to analyze the early stages of precipitation reactions in solution. The main advantage of the tubular reactor set-up is schematically shown in Figure 1. Every position at the continuously operating reactor corresponds to a certain stage of reaction if the flow rate is constant, allowing an almost time-independent acquisition of data. Thus,

the experiment can be considered as a conversion of the time coordinate of a reaction to a spatial coordinate along the tubular reactor system.

EXPERIMENTAL METHODS

The precipitation of zinc sulphide is carried out in a flow jet cell as shown in Figure 2. The tubular reactor is represented by a liquid jet with a diameter of 80 or 50 μm which is injected into a reactive gaseous atmosphere. The liquid jet technique has several advantages compared to the set-up using tubing connected to peristaltic pumps. The use of these free ultra thin liquid jets allows the realization of very short residence times in the microsecond regime and, simultaneously, it avoids undesired effects like fouling of solid on the reactor walls or complete clogging of the reactor. The corpus of the homemade cell consists of stainless steel with polymer foil windows on each side. The liquid jet is produced by an exchangeable platinum/iridium nozzle with a diameter of 50 or 80 μm as it is used for electron microscopes. The liquid is fed with a commercial HPLC pump (Sunchrom, SunFlow 100) via a PEEK capillary with a flow rate of 3.5 or 5.5 ml/min and a resulting pressure of up to 10 bar at the nozzle. A peristaltic pump (Ismatec, MCP) is used to pump the resulting waste out of the cell. In addition to the cell and the waste bottle which are connected directly to an exhaust system, the whole apparatus is covered with a container that is ventilated to avoid gas leakage. Two different adjustments were used as standard parameters: 80 μm nozzle diameter and 3.5

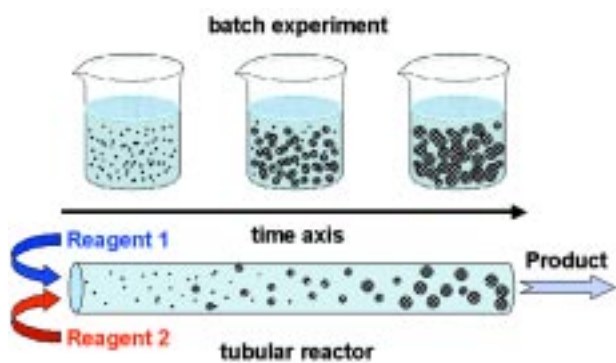


Figure 1. Schematic illustration of the tubular reactor concept

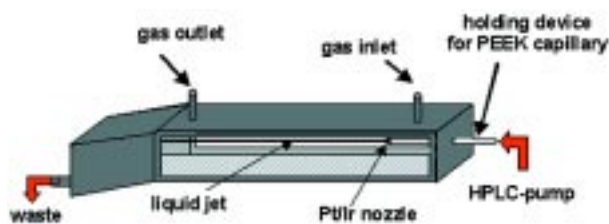
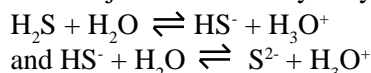


Figure 2. Schematic illustration of the flow jet cell.

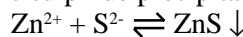
ml/min flow rate and 50 μm nozzle diameter and 5.5 ml/min flow rate due to different stability of the jet. These settings correspond to residence times of 86 μs per millimeter jet length and 21 μs per millimeter jet length, respectively. The shortest residence time achievable was 17 μs corresponding to a jet length of 0.8 mm the closest position that could be measured next to the nozzle.

For the precipitation reaction a 1 molar solution of zinc chloride (ZnCl_2) is injected into an atmosphere of hydrogen sulphide (H_2S) that is continuously delivered into the cell via a saturated

nitrogen stream. By diffusion the gas is transported into the jet where it is hydrolyzed:



The sulphide anions set free by this hydrolysis reaction are consumed by the zinc cations and the zinc sulphide precipitate is formed:



By measuring at different positions along the jet the ongoing crystallization can be followed. All measurements were carried out at the SAXS beamline of the Institute of Biophysics and X-ray Structure Research at ELETTRA.

RESULTS AND DISCUSSION

Figures 3a and b show the residence time dependent scattering curves after subtracting the background. Clearly, it can be seen that there is detectable scattering of particles at residence times as short as 17 μs . Up to 32 μs the particles scattering can be described by Guinier approximation ($qR \ll 1$) indicating small particles with Radius R which grow very fast with increasing residence time. After about 70 μs , due to a rapid growth of the initially formed moieties, the particles are so large that the observed scattering is given by the Porod approximation ($qR \gg 1$). The accessible q -range is limited mainly by the strong cell scattering close to the beamstop. From the scattering data the Porod constant (P) can be determined by the scattering vector q and the scattering intensity:

$$I(q) = \text{const.} + \frac{P}{q^4}$$

The calculated Porod constants P and the

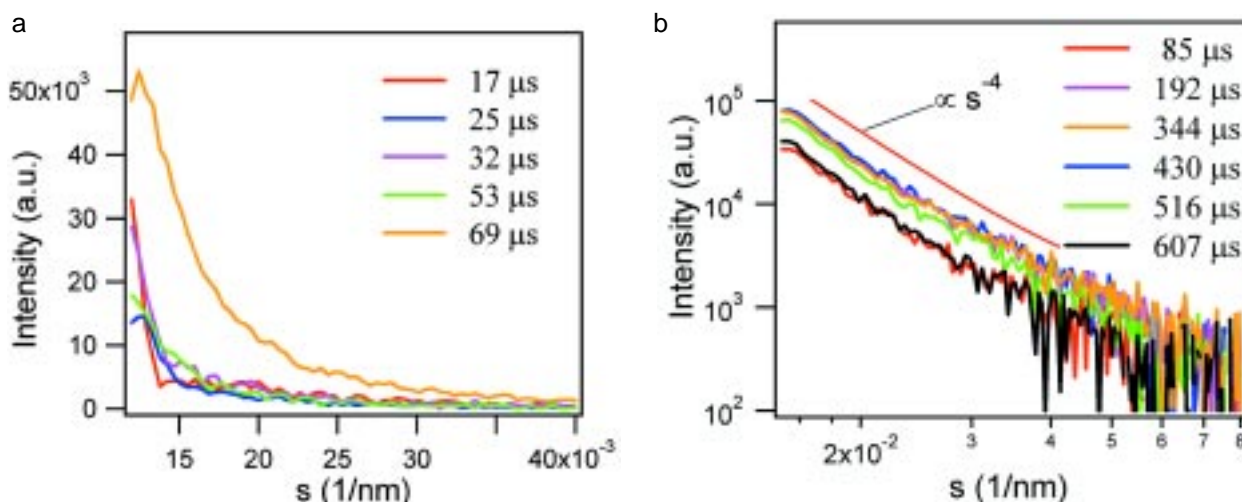


Figure 3. Scattering curves at residence times shorter than 70 μs (a) and up to 600 μs (b).

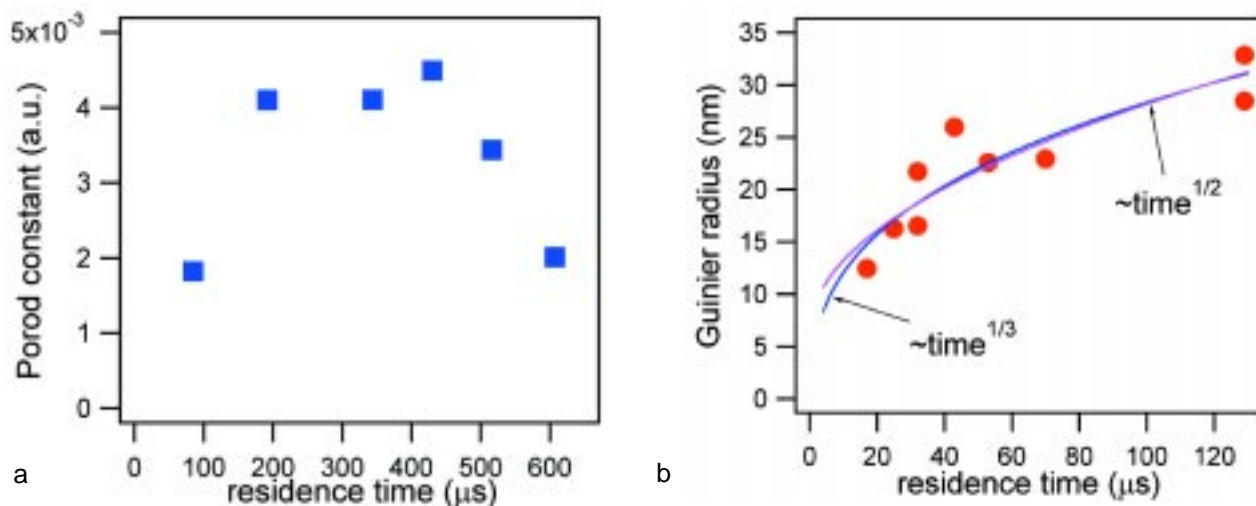


Figure 4. Calculated Porod constants (a) and Guinier radii (b).

corresponding residence times are shown in Figure 4a. The Porod constant is defined for spherical particles as:

$$P \propto \frac{p \cdot \Delta\rho^2}{R}$$

with volume fraction of particles p , difference of the electron density $\Delta\rho$ and the particle radius R . In the range from 80 to 400 μs the value of P increases due to an increase of the number density, whereas the radius remains constant. The situation changes after residence times longer than 400 μs . The value of P decreases again, indicating that the dominating parameter is rather the increase of the particle radius than increase of the volume fraction. An obvious explanation is the aggregation of the particles formed before. The Guinier treatment of the scattering data achieved at shorter residence times is shown in Figure 4b. The radius R of the particles can be calculated using the Guinier approximation:

$$\ln[I(q)]_{\infty} \sim -\frac{q^2 \cdot R_g^2}{3}$$

The calculated values for the Guinier radius R_g ($= \sqrt{3/5} \cdot R$ for spherical particles) show that even after residence times as short as 17 μs the precipitated particles are already of the size of 12 nm. Their fast growth to particles with a Guinier radius of 25 nm

after 50 μs proves the immense speed of the ongoing reaction. The growth of the particles dimension obeys either a $\text{time}^{1/3}$ – law for reaction limited aggregation (RLA) or a $\text{time}^{1/2}$ for diffusion limited aggregation (DLA) as indicated in Figure 4b. To distinguish clearly between both laws of growth further measurements need to be performed reaching a timescale below 10 μs .

CONCLUSIONS

The tubular reactor concept using the liquid jet technique in combination with small angle X-ray scattering allows the direct access to particle growth during fast precipitation reactions. The results presented above are unique for they are the first *in situ* measurements of particle growth and aggregation in solution on a microsecond time scale. The presented liquid jet technique is not limited to certain analytical methods, but can be used as a versatile tool to follow the formation of solids from solution.

ACKNOWLEDGMENTS

We would like thank H. W. Schmidt (Mülheim) for construction of the flow jet cell.

REFERENCES

- [1] P. Bussian, F. Sobott, B. Brutschy, W. Schrader, F. Schüth; *Angew. Chem. Int. Ed.*; 39, 3901, (2000)
- [2] M. Lindén, S. Schunk, F. Schüth; *Angew. Chem. Int. Ed.*; 37, 8215, (1998)
- [3] M. Lindén, S. Schunk, F. Schüth; *Stud. Surf. Sci. Catal.*; 117, 45, (1998)
- [4] M. Lindén, J. Blanchard, S. Schacht, S. Schunk, F. Schüth; *Chem. Mater.*; 11, 3002, (1999)
- [5] J. Rieger, E. Hädicke, I. U. Rau, D. Boeckh; *Tenside Surf. Det.*; 34, 430, (1997)
- [6] M. Z.-C. Hu, J. T. Zielke, C. H. Byers, J. S. Lin, M. T. Harris; *J. Mater. Sci.*; 35, 1957, (2000)

GISAXS study of cadmium sulfide quantum dots reveals clues for design optimization of electro-optical semiconductor devices

P. Dubcek, S. Bernstorff

Sincrotrone Trieste, SS 14 km 163,5, 34012 Basovizza (TS), Italy

U.V. Desnica, I.D. Desnica-Frankovic

Ruder Boskovic Institute, Bijenicka 54, 10000 Zagreb, Croatia

INTRODUCTION

Systems of small dimensions (nanocrystals or quantum dots) exhibit considerably different optical and electronic properties from bulk semiconductors due to quantum confinement. Due to the large optical non-linearity as well as fast response times, systems of semiconductor crystallites buried in glass show great promise for very interesting applications in optical devices such as wave-guides, high-speed optical switches, or bistable resonators. Thus the study of quantum dots is of enormous interest for optical and electronic applications, since the quality of working devices built by the semiconductor industries will depend on the precise control of size and density of an ensemble of quantum dots. Scattering techniques are well suited to obtain such information from a large number of objects.

The traditional method of preparing quantum dots in optical semiconductor devices is by adding semiconductor components into a glass melt. During the solidification process however, one has not sufficient control over the growth process of the nanocrystals, which results in non-ideal sample properties (defects, semiconductor surface states, dopant size fluctuations). Most of these drawbacks are overcome by the newly proposed technique of separate ion implantation into solid substrates. Using ion beams for the synthesis of nanocrystals offers exceptional flexibility in the choice of active components and underlying matrixes, as well as a good control and reproducibility of the production process [1].

EXPERIMENTAL METHODS

CdS nanocrystals were formed in SiO₂ of about 1 mm thickness by implanting separately the

constituent Cd and S atoms with a dose of 10¹⁷/cm² each. This resulted in a gaussian depth density distribution of the dopants (Fig. 1), with a peak volume concentration of about 6.3 10²¹ cm⁻³ of each of the Cd and S atoms at ca 130 nm depth, as determined by Rutherford Back Scattering. The sample was subsequently annealed at 700 °C, to provoke diffusion and synthesis of CdS crystallites. In this way, a CdS rich “film” was formed inside the SiO₂ substrate.

RESULTS AND DISCUSSION

In order to investigate the structure and distribution of CdS quantum dots synthesized in films prepared by this new method, and to determine the optimal values of the implantation parameters, the Grazing Incidence Small Angle X-ray Scattering (GISAXS) technique was applied.

The diffuse scattering from a rough surface of a simple homogenous film is usually described by distorted wave Born approximation [2]. Due to the high concentration of nanocrystalline CdS, the scattered intensity of implanted samples differs considerably from that of nonimplanted ones (Fig. 2). When electron density fluctuations in the sample are present due to randomly distributed nanoparticles, their contribution to the scattering is independent of the grazing angle, and therefore should be added to the surface contribution [3].

Supposing that the substrate surface is not drastically deformed during the implantation (most of the structural changes happen deeper in the substrate where the implanted ions are being decelerated), the change in the scattering intensity at very low angles from not implanted to implanted sample (Fig. 2) is attributed to this particle-like scattering [4]. When a simple particle scattering

GISAXS study of cadmium sulfide quantum dots reveals clues for design optimization of electro-optical semiconductor devices

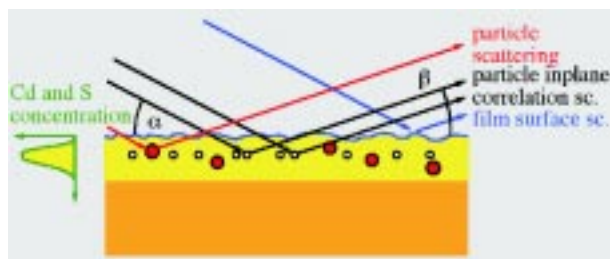


Figure 1. Scattering from a typical sample: nanoparticles are embedded in a substrate. The concentration of the particles is varying with depth as indicated. In addition to the rough surface scattering (blue), particle scattering (red) is also present. When the nanoparticles have more or less the same distance to the surface, a third, the inplane (or lateral) particle correlation contribution to the scattering (black), can be observed.

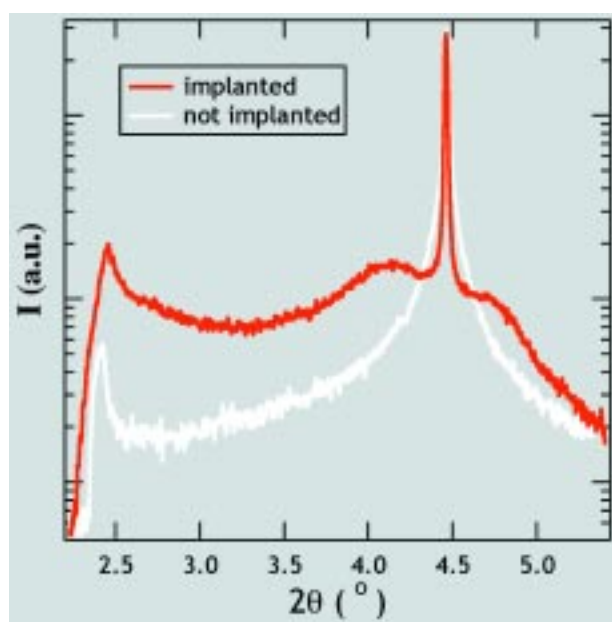


Figure 2. GISAXS from implanted and not implanted SiO_2 substrate for the same grazing angle (2.25°) vs. total scattering angle. The curves are normalized to the same specular peak intensity.

model (Guinier approximation) is applied here, a particle diameter of 4.6 nm is deduced.

However, when the nanoparticles are highly aligned laterally (parallel to the substrate surface), their contribution to the scattering has also a grazing angle dependant component, which is strongest close to the specular peak (shoulders on either side of the peak). This is attributed to the correlation of two particles (with positions offset with respect to the average depth) at a given particle-particle distance [5]. Therefore, when deconvoluting numerically the surface roughness contribution from the total scattering, the curves plotted in Figure 3 are obtained.

The position of a shoulder (or lateral peak) is then interpreted — for a given grazing angle — as a measure of the mean interparticle distance within the same sample depth. This is plotted in Fig. 4 as a function of the penetration depth for a given grazing angle.

CONCLUSIONS

In contrast to the traditional methods of preparing quantum dots in optical semiconductor devices which are suffering from significant drawbacks, a newly proposed technique of separate ion implantation into solid substrates with subsequent annealing was used to prepare CdS quantum dots in amorphous SiO_2 . In order to investigate the structure and distribution of thus prepared quantum dots, the grazing incidence small angle X-ray scattering (GISAXS) technique was used.

Due to the high concentration of nanocrystalline CdS, the scattered intensity is not following the simple models for homogenous film scattering. Apart from the surface roughness scattering, two different contributions have been identified: a) the scattering from particles randomly distributed within the film, giving an additive contribution to the scattering, and b) the inplane particle correlation contribution

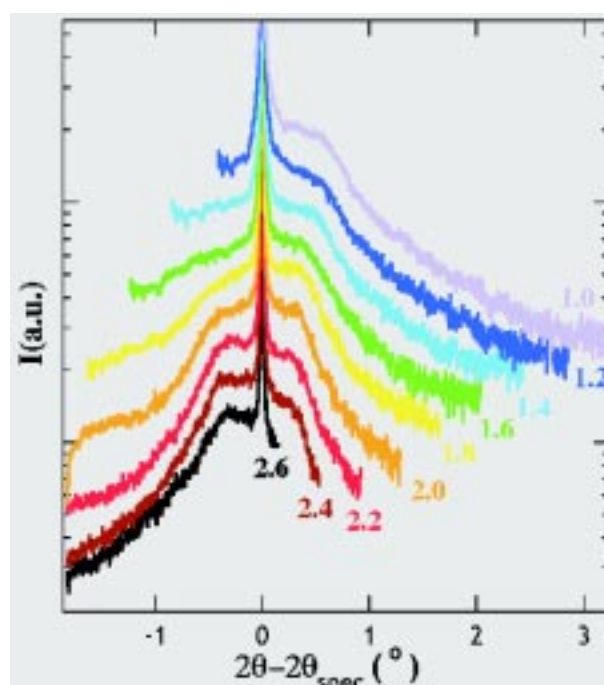


Figure 3. Inplane correlation part of GISAXS from ion (Cd and S) implanted SiO_2 vs. offset from specular angle, for diverse grazing incidence angles (in degrees, as indicated). The curves are offset vertically for clarity.

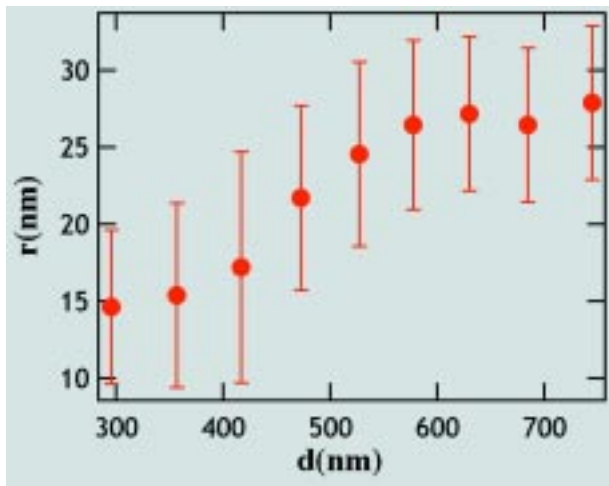


Figure 4. Inplane correlation length (mean interparticle distance) vs. X-ray penetration depth.

coming from particles which are arranged more or less parallel to the surface with respect to each other. From the first contribution, the particle diameter is

estimated to be about 4.6 nm, while the latter indicates the interparticle distance to be in the range of 15-28 nm. However, given the 20% atomic fraction of implanted Cd and S, the interparticle distance should be about 7 nm [3]. Thus the experimental values suggest that either not all of the implanted ions are taking part in CdS formation, or that CdS redistribution took place during the annealing [3].

The optical properties of quantum dots depend heavily on nanoparticle sizes and distribution. Therefore the presented results are another important and very promising step in taking full control of the production of semiconductor quantum dots with specifically aimed properties.

ACKNOWLEDGMENTS

This research was partly supported by the Ministry of Science and Technology of Croatia. The samples have been kindly provided by C.W. White from Oak Ridge National Laboratory.

REFERENCES

- [1] J.D. Budai, C.W. White, S.P. Withrow, M.F. Chisholm, J.Zhu, R.A. Zuhr, *Nature*, 390, 384 (1997).
- [2] S. K. Sinha, E.B. Sirota and S. Garoff, *Physical. Review. B* 38, 2297 (1988)
- [3] P. Dubcek, S. Bernstorff, U.V. Desnica, I.D. Desnica-Francovic and K. Salomon, *Surface Review and Letters*, in print
- [4] S. Dietrich, A. Haase, *Physical Reports*, 260, 1 (1995)
- [5] R. Stommer, U. Englisch, U. Pietsch, V. Holy, *Physica B* 221, 10 (1996)

Self-assembly of 2D-Hexagonal templated TiO₂ mesostructured films during dip-coating

D. Grosso, F. Babonneau, C. Sanchez, G. J. de A. A. Soler-Illia, E. L. Crepaldi

Chimie de la Matière Condensée, UPMC - CNRS, 4 place Jussieu, 75005 Paris, France

P.A. Albouy

Lab. de Physique des Solides, Université Paris-Sud, 91405 Orsay, France

H. Amenitsch

Institute of Biophysics and X-ray Structure Research, Austrian Academy of Sciences, Steyrergasse 17/VI, 8010 Graz, Austria

A.R. Balkenende

Philips Research Laboratories, Prof. Holstlaan 4, 5656 AA Eindhoven, Netherlands

A. Brunet-Bruneau

Laboratoire d'Optique des Solides, UPMC, 4 place Jussieu, 75 252 Paris, France

INTRODUCTION

The template method, where inorganic intermediate oligomers polycondense in presence of surfactant micelle supramolecular arrays, was first discovered by Mobil for silica based materials [1] and since then has been used for the preparation of meso-structured hybrids and mesoporous materials, using various oxide networks and templates [2, 3, 4]. Among these materials, mesoporous silica has been the most studied one. Works concerning other metal oxide based meso-structured materials are more discrete because of the synthetic difficulties related to both kinetic and coordination aspects, characteristic of metallic cations such as Ti⁴⁺ [4]. However, we recently described a highly reproducible method to prepare 2D-hexagonal TiO₂ mesoporous thin films by dip-coating, using TiCl₄ as precursor, Brij 58 as structuring agent and a water/alcohol medium [5]. Many efforts have been conducted toward the preparation of various types of mesostructured materials rather than to the comprehension of the self-assembly mechanisms taking place during dip-coating. The formation of films by dip-coating is associated with the E.I.S.A. (Evaporation-Induced Self-Assembly) process first introduced by Brinker et al. [6] This method involves the rapid evaporation of the volatile molecules, which induces simultaneously the formation of the mesophase and the polycondensation of the inorganic entities. Few studies, performed with high-flux Small Angle X-Ray Scattering (SAXS) beamlines, on the kinetics of CTAB-silicate and copolymer-silicate

self-assembly, during the precipitation of powders in solution [7, 8, 9], and during the formation of thin films [10, 11], have been recently published. These works showed that the self-assembly is a complex process that is governed by the interactions existing at interfaces between organic and inorganic phases present in the system. The present paper focuses on the in-situ study of the structural evolution during formation of 2D-hexagonal meso-structured hybrid TiO₂ films, obtained by co-assembly with Brij 58. The various steps observed along the evaporation / organization / condensation process are presented.

EXPERIMENTAL METHODS

The final molar ratios of a typical initial solution were TiCl₄: 1; Brij 58: 0.05; EtOH: 40 and H₂O: 10. Films were prepared by dip coating 8 μm thin silicon wafers at a constant withdrawal rate of 2.5 mm.s⁻¹ and at a controlled relative humidity of 53%. Micrographs of calcined films were obtained with a transmission electron microscope (TEM) JEOL 100 CXII apparatus. The time-resolved SAXS measurements were performed at the Austrian high-flux SAXS beamline [12]. The sol container was lowered while the substrate supporting the film remained fixed in order to analyse the same film region during evaporation (Fig. 1a). Substrates were placed at an angle of 2.0±0.5° with respect to the incident X-ray beam direction. Structure was deduced from the diffracted patterns collected every 2s with a X-ray sensitive CCD detector.

Interferometry measurements were simultaneously performed with the SAXS measurements. The substrate was illuminated with a monochromatic diode (440 nm) and a visible CCD camera was placed as to record the constructive and destructive interference fringes characteristic of the film thickness evolution.

RESULTS AND DISCUSSION

Figure 1b shows the TEM image of a TiO₂ based film piece scratched from the substrates and previously heat-treated at 350°C, together with a

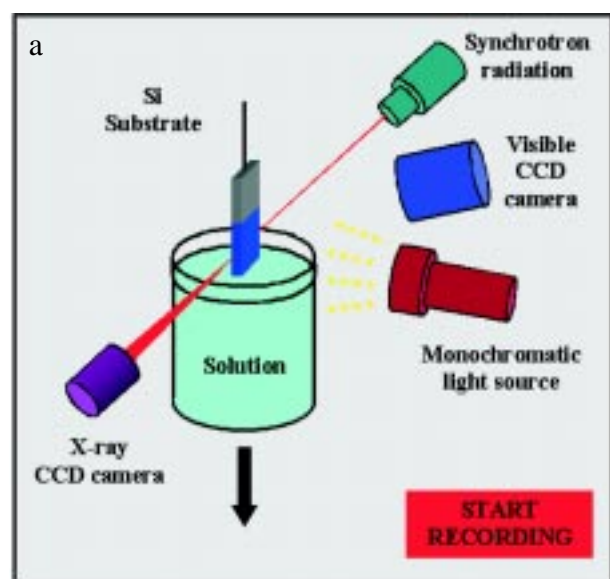


Figure 1a. Schematic representation of the in-situ time-resolved XAXS and Interferometry investigation during dip-coating.

typical 2D-XRD pattern obtained for as-prepared films (Fig. 1d $t=350s$). Both analyses clearly show that these films contain mesoporous channel pores (4-5nm), which are arranged into a p6m 2D-hexagonal structure with the c axis preferentially aligned with the surface. This system has been well described in a previous paper [5]. The HRTEM microscopy of the calcined TiO₂ film revealed the presence of anatase nano-particles as shown in Figure 1c. Figure 1d represents the in-situ time-resolved study of TiO₂ based film formation during dip coating as revealed by simultaneous SAXS and interferometry analyses. 15s after the starting of the deposition process, the film is still drying (presence of interference fringes) and no diffraction is observed. The drying line (attributed to the last fringe) is

reached after 110s, which suggests that most of the liquid phase has departed the system after this point. The first diffraction signal is a low intense and homogeneous ring that starts to appear at 135s (25s after the drying line) and grow in intensity up to 70s after the drying line. This latter diffraction ring is characteristic of a worm-like structure where the organic micelles are elongated and randomly oriented within the film. From 190s, the ring is progressively replaced by diffraction spots and the whole transformation process lasts around 20s. The diffraction spot positions are characteristic of a p6m 2D-hexagonal structure (lattice parameter $a = 6.5nm$) for which the micelles are hexagonally compacted and preferentially aligned with the surface. The diffraction spot intensity increases continuously during several minutes following their appearance. The last phenomenon that is observed is the contraction of the normal to the surface deduced from the extension of the diffraction pattern in the corresponding direction.

The mechanisms involved in the formation of P6m films can be modelled as shown in Figure 1e. The first stage corresponds to the evaporation of the liquid phase up to the drying line. During the second period, the evaporation rate is lower and, eventually, micelles start to form first at the air/film interface. The resulting worm-like structure progresses toward the film/substrate interfaces as the concentration in surfactant molecules increases with time and from the bottom to the surface of the film. During the third period, the film thickness does not significantly decrease anymore, and the worm-like structure progressively transforms into 2D-hexagonal structure. Such a transformation is not only due to the interaction existing at the interface between micelles and the inorganic network, promoting the

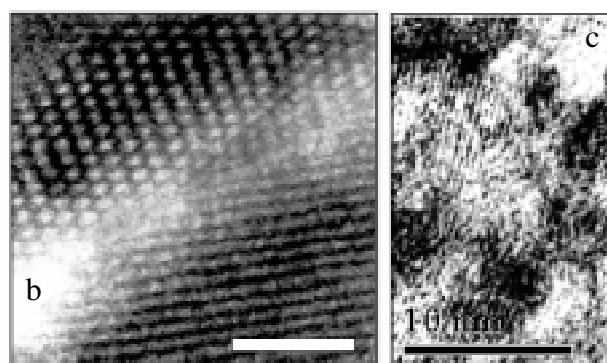
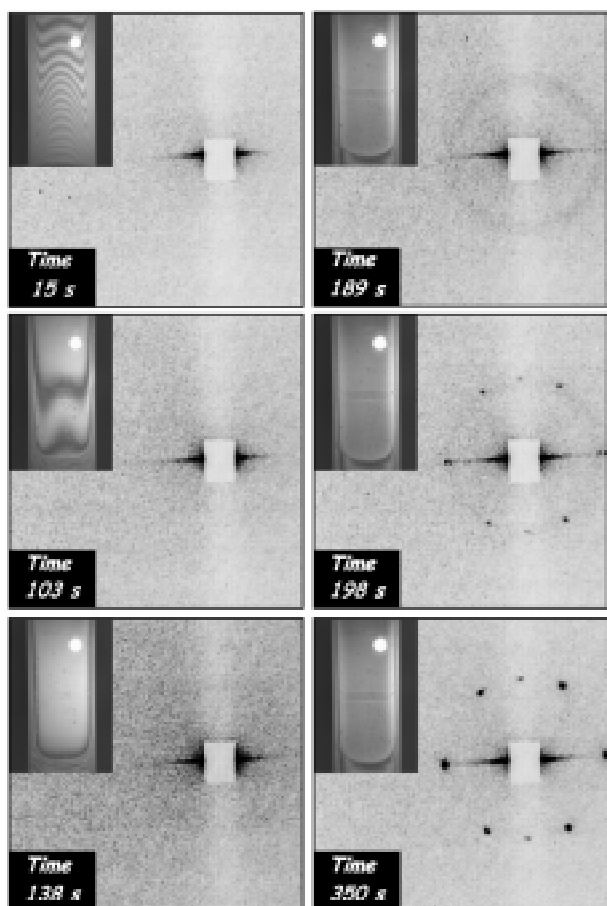


Figure 1b. TEM image of a treated TiO₂ film showing the 2D-hexagonal arrangement of pores.

Figure 1c. HRTEM image of a treated TiO₂ film showing anatase planes.



d

Figure 1d. In-situ time-resolved interferometry and SAXS data obtained during TiO₂ based film formation.

formation of elongated micelles, but also due to the presence of air/film and film/substrate interfaces that favours the alignment of the micelles. The 2D-hexagonal structure grows thus from the interfaces towards the film centre by re-organisation alignment of micelles. Once the organised structure is formed, films continue to dry and condense, inducing the uniaxial contraction of the structure always observed with such films.

CONCLUSIONS

Despite the difference of chemistry, the same mechanism applies during the preparation of films by dip-coating. TiO₂ mesostructured film formation is governed by the competition taking place between the rapid evaporation of the liquid phase, the self-assembly of micelles with the inorganic phase, and the rate of hydrolysis condensation. In addition, the formation of P6m structure takes place after the drying line. It thus requires direct interaction of surfactant with the inorganic phase and also the presence of film/air and film/substrate interfaces that force the micelles to align and to reorganise in the characteristic p6m compact hexagonal structure. One should not forget that the self-assembly process involved during E.I.S.A strongly depends on critical parameters such as the surfactant concentration, the pH, the water content, the solution age, the relative humidity, which will be discussed in a forthcoming paper.

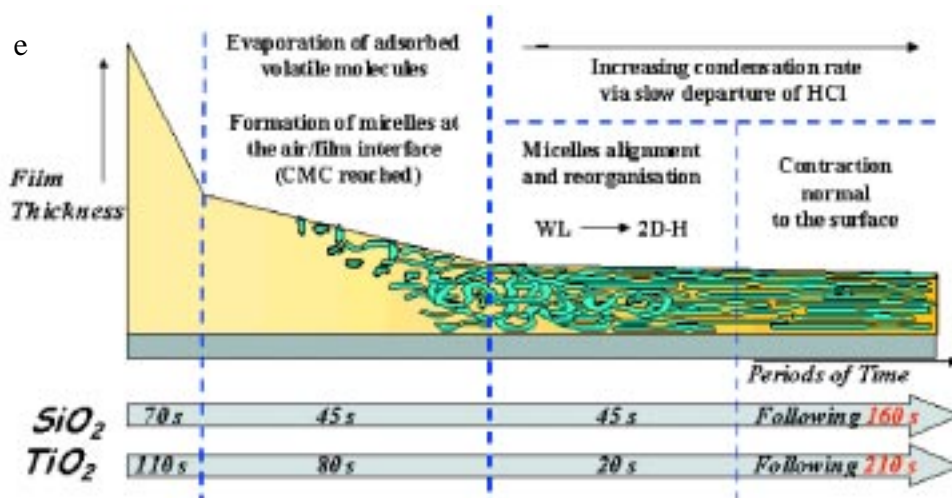


Figure 1e. Model of 2D-hexagonal mesostructure formation.

REFERENCES

- [1] J.S. Beck, J. C. Vartuli, W. J. Roth, M. E. Leonovicz, C. T. Kresge, K. D. Schmidt, C. T-W. Chu, D. H. Olson, E. W. Sheppard, S. B. McCullen, J. B. Higgins, and J. L. Schlenker, *Journal of American Chemical Society* 114, 10834 (1992).
- [2] D. Zhao, Q. Huo, J. Feng, B. F. Chmelka, and G. D. Stucky, *Journal of American Chemical Society* 120, 6024 (1998).
- [3] U. Ciesla, and F. Schuth, *Microporous and Mesoporous Materials* 27, 131 (1999).
- [4] J. Y. Ying, C. P. Mehnert, and M. S. Wong, *Angew. Chem. Int. Ed.* 38, 56 (1999).
- [5] D. Grosso, G. J. de A. A. Soler-Illia, F. Babonneau, C. Sanchez, P. A. Albouy, A. Brunet-Bruneau, and A. R. Balkenende, *Advanced Materials*, in press (2001).
- [6] C. J. Brinker, Y. Lu, A. Sellinger, and H. Fan, *Advanced Materials* 11, 579 (1999).
- [7] P. Agren, M. Linden; B. Rosenholm, J. Blanchard, F. Schuth, and H. Amenitsch, *Langmuir* 16, 8806 (2000).
- [8] M. Linden, P. Agren, S. Karlson, P. Bussian, and H. Amenitsch, *Langmuir* 16, 5831 (2000).
- [9] C. C. Landry, S. H. Tolbert, K. W. Gallis, A. Monnier, G. D. Stucky, P. Norby, and J. C. Hanson, *Chemistry of Materials*, 13, 1600 (2001).
- [10] D. Grosso, A. R. Balkenende, P. A. Albouy, H. Amenitsch, and F. Babonneau, *Chemistry of Materials* 13, 1848 (2001).
- [11] D. Grosso, F. Babonneau, P.A. Albouy, H. Amenitsch, A.R. Balkenende, A. Brunet-Bruneau and J. Rivory, *Chem. Mat.*, (submitted).
- [12] H. Amenitsch, S. Bernstorff and P. Laggner, *Rev. Sci. Instrum.* 66, 1624 (1995).

Investigation of the LMM Auger spectra of Fe in ultrathin Fe films grown on Cu(100): variations in the lifetime of 3d hole states

S. D'Addato, P. Luches

Istituto Nazionale di Fisica della Materia and Dipartimento di Fisica, Università di Modena e Reggio Emilia, Via G. Campi 213/a, 41100 Modena, Italy

R. Gotter, L. Floreano, D. Cvetko, A. Morgante

Laboratorio TASC-INFN, SS 14 Km 163.5, 34012 Trieste, Italy

A. Newton, D. Martin, P. Unsworth, P. Weightman

Surface Science Research Centre, The University of Liverpool, PO Box 147, Liverpool L69 3BX, UK

INTRODUCTION

The correlation effects in 3d transition metals and their compounds have been studied extensively with electron spectroscopy techniques. A particularly well studied effect is the presence of “satellites” at low kinetic energies in the X-ray excited $L_3M_{45}M_{45}$ Auger spectra of the elements Fe, Co, Ni, Cu and Zn [1-3]. They are due to the $L_3M_{45}-M_{45}M_{45}$ transitions arising from double ionised initial states. This notation refers to a transition between an initial double ionised state with holes in the L_3 and M_{45} levels and a final state with three M_{45} holes in the final state. The M_{45} level is of course the 3d band of the condensed phase and a study of such processes can provide information on the localisation of 3d holes. The initial double hole states can be created by several mechanisms, notably $L_1-L_{23}M_{45}$ and $L_2-L_3M_{45}$ Coster-Kronig transitions and L_3M_{45} shake up and shake off processes (see inset in figure 1). The intensity and spectral profiles of these satellites have been shown to depend on chemical environment [4-7]. For instance, synchrotron radiation studies found that in pure Fe the intensity of the $L_3M_{45}-M_{45}M_{45}$ Auger vacancy satellite transition is negligibly small because of a high degree of delocalisation of the 3d spectator hole prior to the decay of the L_3 core hole [4,7], whereas in FeAl this transition has significant intensity due to the localisation of the 3d spectator hole, an effect which was attributed to the reduction in the density of states at the Fermi energy in the alloy [7].

In an investigation of this phenomena we performed a detailed study of the Fe LMM Auger profile of Fe ultrathin films grown on Cu(100). The investigation was carried out with two methods:

a) Auger spectra were measured at different photon energies below and above the Fe L_2 photoionisation threshold with the aim of detecting any differences in the lineshape caused by the opening of the L_2 ionisation channel, which is the origin of the $L_2-L_3M_{45}$ and subsequent $L_3M_{45}M_{45}$ decay. This method was applied to films of different thickness, from 0.3 to 10 ML.

b) We also performed an Auger photoelectron coincidence spectroscopy (APECS) experiment on 1 ML of Fe grown on Cu(100), looking at the coincidence signal between the Fe LMM line with the $2p_{3/2}$ and $2p_{1/2}$ photoemitted electrons. The resulting coincidence spectra arise from the Auger decay of a hole produced respectively in the $2p_{3/2}$ and $2p_{1/2}$ core levels. This work demonstrates the feasibility of such an experiment on ultrathin solid films.

RESULTS AND DISCUSSION

All the experiments were performed on the ALOISA beamline at ELETTRA [8]. Figure 1 shows the Fe $L_3M_{45}M_{45}$ Auger spectra obtained from the different films. The photon energy used to excite the 2p core levels involved in the Auger decay process was 840 eV, much higher than the L_3 and L_2 ionisation edge, that are 706.8 and 719.9 eV respectively. The spectra were taken from 0.3 monolayer (ML) Fe/Cu(100), 1 ML Fe/Cu(100), 10 ML Fe/Cu(100) and from a 1 ML Fe film grown with the substrate held at a temperature $T=150^\circ\text{C}$. This latter temperature was chosen to improve the smoothness of the film without significant interdiffusion phenomena. The spectra are similar in shape with the low energy region below the main peak being significantly more

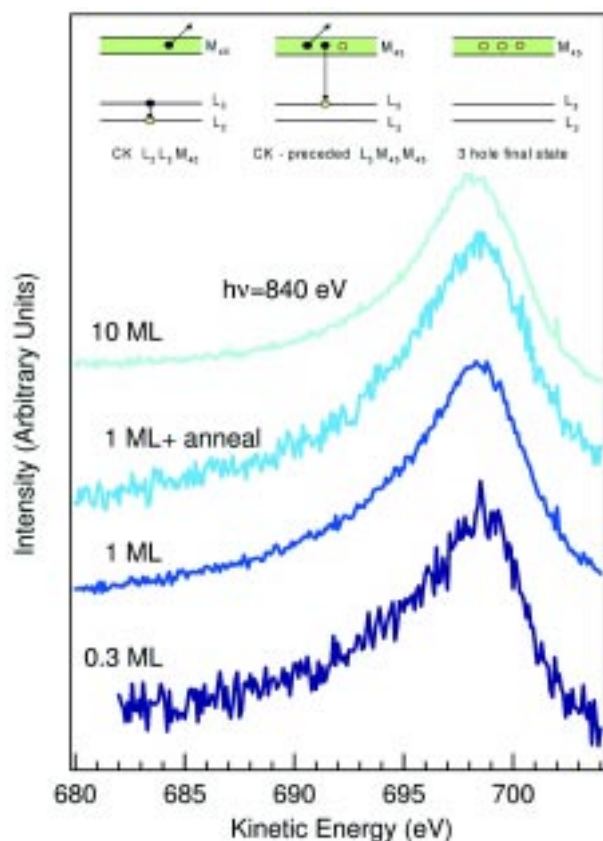


Figure 1. Fe $L_{3}M_{4.5}M_{4.5}$ Auger spectra taken from Fe films of different thickness. All the spectra have been normalised to the intensity difference between the maximum and the background at higher kinetic energies. The photon energy used was $h\nu=840$ eV. Inset: Energy diagram showing the Auger transitions leading to the $M_{4.5}M_{4.5}M_{4.5}$ final state

intense for the 10 ML coverage. The main peak in the spectrum obtained from the 10 ML film is also shifted by 0.8 eV to lower kinetic energy than the peak in the other films. We note that the changes observed in the spectrum from the 10 ML film may be associated with a change in the structure since this coverage is very close to the thickness values where the whole Fe film is claimed to undergo a transition from the face centred cubic (fcc) phase, obtained for ultrathin Fe films of coverage less than 12 ML, to the ordinary body centred cubic (bcc) phase [9].

In order to search for satellite features in the $L_{3}M_{4.5}M_{4.5}$ lineshape, caused by the spectator hole produced by the $L_{2} - L_{3}M_{4.5}$ transition, we took the Auger spectra at different photon energies around the Fe L_{2} absorption edge (719.9 eV). Our results show that for both the 0.3 ML and 10 ML coverages the spectral region to low energy of the main peak is higher in relative intensity when excited by photons above the Fe L_{2} absorption edge. In contrast the spectra obtained from the 1 ML coverage are almost

independent of the energy of the exciting photons. Figure 2 shows the results obtained for the 10 ML coverage by subtracting the spectrum excited by 714 eV photons from the spectra excited by higher energy photons. Some variations in the low kinetic energy region are clearly visible and a broad structure grows in this energy range at increasing photon energies. Finally, Figure 3 shows the APECS data acquired on a 1 ML Fe film deposited on Cu(100). The $L_{2,3}M_{4.5}M_{4.5}$ Auger spectra detected in coincidence with $2p_{1/2}$ and $2p_{3/2}$ photoemission electrons are shown, together with the Auger singles spectrum. The Fe $L_{2,3}M_{4.5}M_{4.5}$ Auger spectrum detected in coincidence with $2p_{3/2}$ photoelectron shows the main $L_{3}M_{4.5}M_{4.5}$ contribution, while, as expected, the coincidence count rate is close to zero in the $L_{2}M_{4.5}M_{4.5}$ energy region in this spectrum. The Fe $L_{2,3}M_{4.5}M_{4.5}$ Auger spectrum detected in coincidence with $2p_{1/2}$ photoelectron shows a significant count rate in the $L_{2}M_{4.5}M_{4.5}$ energy region, which is to be expected, and also shows a contribution to the intensity in the region of the main $L_{3}M_{4.5}M_{4.5}$ peak and to the lower kinetic energy side of this peak.

We are seeking information on the degree of localisation of d holes on Fe sites in these thin film systems. The key issue is the lifetime of the spectator $M_{4.5}$ hole in the initial $L_{3}M_{4.5}$ state. If this remains localised for longer than the lifetime of the L_{3} hole then the decay of the L_{3} hole will contribute to the intensity in the satellite region of the spectrum. However if the spectator hole delocalises before the

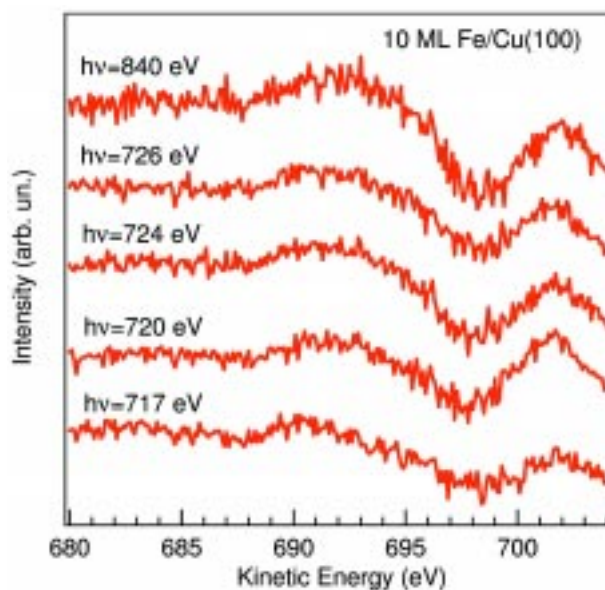


Figure 2. Difference curves between the Fe $L_{3}M_{4.5}M_{4.5}$ Auger spectra from 10 ML Fe/Cu(100) taken at different photon energies and the same spectrum taken at $h\nu=715$ eV, lower than the Fe L_{2} ionisation edge.

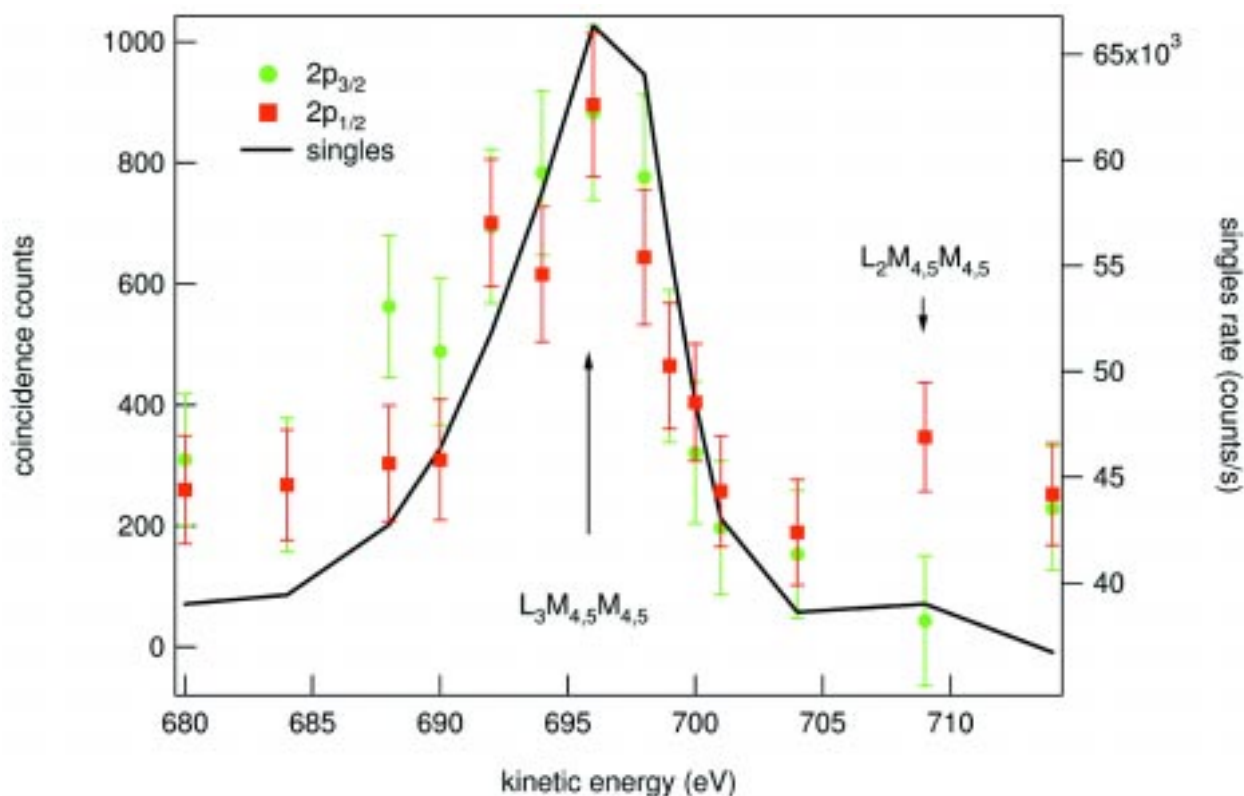


Figure 3. Fe $L_{23}M_{4,5}M_{4,5}$ spectra taken in coincidence with the $2p_{3/2}$ (full circles) and $2p_{1/2}$ (squares) photoelectrons. The solid line is the singles spectrum which is also determined from the same set of raw data.

decay of the L_3 hole then this intensity will appear in the main $L_3M_{4,5}M_{4,5}$ peak. The L_3 hole lifetime has been estimated to be $\sim 2 \times 10^{-15}$ s [10,11]. If the $L_3M_{4,5}M_{4,5}$ transitions are observed then the $M_{4,5}$ hole states are localised for longer than $\sim 2 \times 10^{-15}$ s. If these transitions are not observed then the $M_{4,5}$ hole states hop away in a shorter time.

For the lowest coverage of 0.3 ML of Fe on Cu(100) the results indicate that once the photon energy is high enough to excite the L_2 hole state, and hence to give rise to L_2 - $L_3M_{4,5}$ Coster-Kronig transitions, the relative intensity in the satellite region is increased indicating that the $M_{4,5}$ hole state is localised. The localisation of the $M_{4,5}$ hole for this submonolayer coverage is probably due to the low number of Fe neighbors and the low density of states at the Fermi energy.

The results for the 1 ML coverage indicate that most of the $M_{4,5}$ hole states created by the L_2 - $L_3M_{4,5}$ Coster-Kronig delocalise before the decay of the L_3 hole state. We attribute this reduction in the localisation of the $M_{4,5}$ hole state with increasing coverage to the increase in the number of Fe-Fe neighbours and an increase in the density of states at the Fermi energy in this system. In fact, Fe islands have been shown to form an interconnected domain at the nominal thickness of 1 ML [9].

The experimental results for the 10 ML coverage shown in Figure 2 indicate that the $M_{4,5}$ hole state is localised in this system as there is a significant increase in the relative intensity of the satellite region once the photon energy is high enough to excite the L_2 state. The relative intensity of the satellite continues to grow with increasing photon energy (Fig. 2) probably due to a corresponding increase in the L_2 photoemission cross-section. In seeking an explanation for this behaviour we note that at this coverage Fe undergoes a phase change from the fcc structure, the magnetic behaviour of which is complex [12,13], to the magnetic bcc structure. This phase change results in a reduction of the Fe nearest neighbors from 12 to 8 and tends to increase the localisation of the $M_{4,5}$ hole. However we have seen that in pure Fe the low number of nearest neighbors in the bcc structure is not sufficient to localise the $M_{4,5}$ hole. The difference between the results obtained for the 10 ML Fe/Cu(100) system and those of pure Fe may be due to the incomplete formation of the magnetic band structure in the thin film. The onset of magnetism arises from a splitting of the d band into minority and majority spin states. For a thin film the density of states at the Fermi energy for one and possibly for both of the spin states may be too low to allow the $M_{4,5}$ hole to hop away rapidly. Also, some

role can be played by the additional reduced average Fe coordination, as the relaxation caused by the fcc - bcc transition gives rise to a substantial amount of roughness in the film texture [9].

Finally we consider the results of the coincidence experiment for the 1 ML Fe/Cu(100) system (fig. 3). As observed earlier the trivial expectation that L_3 hole states correlate with the $L_3M_{4,5}M_{4,5}$ spectrum and L_2 hole states correlate with the $L_2M_{4,5}M_{4,5}$ spectrum is borne out by the results. However it is also clear that the decay of L_2 hole states contribute to the intensity in both the region of the $L_3M_{4,5}M_{4,5}$ main line and in the satellite region ~ 680 eV to 690 eV. The observation that L_2 hole states contribute to the spectral intensity in both these regions of the spectrum is consistent with the results of Auger singles spectra taken at different photon energies (not shown here) which show only a small increase in the relative intensity of the 685 eV to 695 eV region once L_2 holes are excited. These results indicate that the lifetime of the $M_{4,5}$ holes is comparable to the lifetime of the L_3 hole state at this coverage. For some of the $L_3M_{4,5}$ hole states created by L_2 - $L_3M_{4,5}$ Coster-Kronig transition the $M_{4,5}$ hole hops away before the L_3 hole decays leading to intensity in the $L_3M_{4,5}M_{4,5}$ region of the spectrum. For other $L_3M_{4,5}$ hole states the $M_{4,5}$ remains localised until after the decay of the

L_3 hole state giving rise to intensity in the $L_3M_{4,5} - M_{4,5}M_{4,5}M_{4,5}$ satellite region of the spectrum.

CONCLUSIONS

This work thus demonstrates a coverage dependent localisation of the $M_{4,5}$ (3d) holes. For 0.3 ML of Fe on Cu(100) the 3d holes are localised on Fe sites due the low number of Fe-Fe nearest neighbours and the low density of Fe states at the Fermi energy. As the coverage increases the number of Fe-Fe nearest neighbours and the density of states at the Fermi energy both increase facilitating the delocalisation of 3d holes. These effects are sufficient to delocalise 3d holes in a 1 ML thick film. We attribute the localisation observed for the 10 ML film to the fcc to bcc phase change, accompanied by a dramatic roughness increase which lowers the atomic coordination number, and to the onset of magnetic behaviour.

ACKNOWLEDGMENTS

We acknowledge the significant support for this work provided by NATO and by INFM.

REFERENCES

- [1] P.Weightman, Rep. Prog. Phys. 45 (1982) 753.
- [2] H.W. Haak *et al.*, Phys. Rev. Lett. 41 (1978) 1825.
- [3] D.D. Sarma, *et al.*, Phys. Rev. Lett. 63 (1989) 656.
- [4] D.D. Sarma *et al.*, Phys. Rev. B48 (1993) 6822.
- [5] S.R. Barman and D.D. Sarma, J. Phys.: Condensed Matter 4 (1992) 7607.
- [6] G. Currò *et al.*, Phys. Rev. B46 (1992) 15652.
- [7] P. Unsworth *et al.*, J. El. Spectrosc. Rel Phen. 72 (1995) 205.
- [8] L. Floreano *et al.*, Rev. Sci. Instr. 70 (1999) 3855.
- [9] J. Giergel *et al.*, Phys. Rev. B52 (1995) 8528.
- [10] M.H. Chen *et al.*, Phys. Rev. A24 177 (1981).
- [11] J.C. Fuggle and S. F. Alvarado, Phys. Rev. A22 1615 (1980).
- [12] M. Wuttig *et al.*, Surf. Sci. 331 (1995) 659.
- [13] V.L. Moruzzi *et al.*, Phys. Rev. B34 (1986) 1784; Phys. Rev. B39 (1989) 6957.

Low-dimensional electronic structures on In-terminated InAs(001)-c(4x4) and -(4x2)c(8x2) surfaces

P. De Padova, P. Perfetti, C. Quaresima

CNR-ISM, via Fosso del Cavaliere, 100, 00133 Roma, Italy

C. Richter, M. Zerrouki

LMPS, Université de Cergy-Pontoise, Neuville/Oise, 95031 Cergy-Pontoise, France

K. Hricovini

LMPS, Université de Cergy-Pontoise, Neuville/Oise, 95031 Cergy-Pontoise, France

LURE, Bat. 209 D., 91 898 Orsay, France

INTRODUCTION

Studies of InAs(001) surfaces have been promoted by their potential interest for spin electronics and due to low-dimensional features which give rise to quantum-effects.

The confinement of the electrons in systems at low-dimension produces new physical effects on the electronic structures which are particularly interesting to observe in photoemission spectroscopy experiments. Presently, most studies of state-solid physics are focused on the understanding of the electronic states behaviour of simple One- and Two-dimension (1D, 2D) systems.

Unlike GaAs(001) and InSb(001) [1, 2], where a complicated phase diagram of the surface reconstructions was identified, the In-terminated InAs(001) surface exhibited minor mixture of surface atomic configurations [3]. An ideal (001) surface consists of either III or V group atoms. Real (001) surfaces of compound semiconductors are never ideally terminated, but show several reconstructions and stoichiometries. By using Ar-Ion bombardment annealing (IBA) or Molecular Beam Epitaxy (MBE), the composition and reconstruction of (001) surfaces may be controlled from anion- to cation-rich by adjusting the substrate temperature and the ratio of the respective fluxes.

In this contribution we take advantage of the fact that In-terminated InAs(001) surfaces exhibit well ordered atomic low-dimensional structures, and we explore the valence band electronic properties by angular-resolved photoelectron spectroscopy (ARPES), completing our studies by core level spectroscopy and LEED analysis.

EXPERIMENTAL METHODS

ARPES experiments were carried out in ultra high vacuum (UHV) conditions (base pressure 8×10^{-11} mbar) at the VUV beamline. We worked with s-polarised light (the angle between the photon beam and the normal to sample surface was $\sim 10^\circ$), and collected the electrons *in-* and *-off* the plane of incidence. The surface of the sample was oriented with the In-chains, which are located along the [011] direction, perpendicular to the photon electric field. Valence band photoemission spectra were measured after cooling the sample to ~ 150 K using an angle-resolved hemispherical (acceptance 2°) electron energy analyser. The photon energies were chosen between 19 eV and 200 eV, and the total energy resolution was better than 50 meV. The Fermi level was measured on a gold-foil in electrical contact with the sample, all spectra are presented as a function of relative binding energy.

Undoped InAs(001) ($3.5 \Omega \cdot \text{cm}$) single crystals were used for all the measurements. The In-terminated InAs(001) surfaces were prepared after several cycles of Ar-ion bombardment first at room temperature then at ~ 620 K (hot-IBA), followed by an additional annealing at ~ 570 K and at ~ 750 K. Two surface reconstructions were obtained for these temperatures: twinned c(4x4) (570 K) and untwinned In-rich 4x2-c(8x2) (750 K) respectively. Hereafter for simplicity, we will refer to the latter reconstruction as (4x2). Concerning the structure of the In-terminated InAs(001) surface only the 4x2-c(8x2) reconstruction was observed before [3, 4], while the c(4x4) reconstruction was never reported. The sample temperatures were measured by an infrared

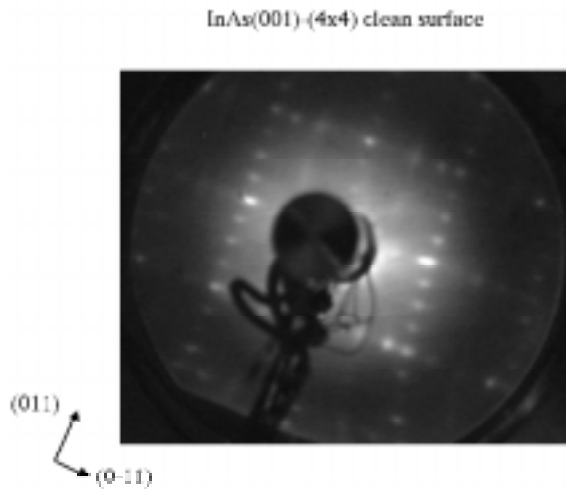


Figure 1. LEED pattern of $c(4 \times 4)$ clean InAs(001) surface, ($E_p = 60$ eV).

pyrometer and a thermocouple. The surface reconstructions were observed by low energy electron diffraction (LEED).

RESULTS AND DISCUSSION

Figure 1 shows the LEED pattern of an InAs(001) surface prepared by hot-IBA. The sharp fourth-order spots in both [011] and [0-11] directions on the whole area of the (001) surface, clearly prove the presence of a $c(4 \times 4)$ reconstruction. The brightness and sharpness of the spots, and the low background intensity indicate that the surface is highly ordered and smooth, with a very large coherence length. The lattice of the $c(4 \times 4)$ arrangement in the real space, as reported in [5] for GaAs(001) As-terminated surface, can be considered such as chess-board with the dimer atoms occupying rectangular units.

Since the desorption of As atoms from InAs(100) surface occurs in the temperature range between about 520 K and 740 K, and a molecular flux of As is needed to obtain the As-terminated surface [6, 7, 8], we argue that the hot-IBA procedure used to reconstruct our samples is likely to give an In-terminated surface, in agreement with the calculations of the photoemission intensity ratio between the In 4d and As 3d peaks.

Figure 2 shows photoelectron spectra collected on an InAs(001) unreconstructed sample, InAs(001)- $c(4 \times 4)$ and $-(4 \times 2)$ surface reconstructions, which probe the energy region between the upper part of the valence band and the bottom of the conduction band. Spectra were collected at a photon energy of 31 eV with the electron analyser normal to the surface ($K_{\parallel} = 0$) in the incidence plane. In the case of InAs(001)- (4×2) the In-rows ([011] direction) were perpendicular to the photon electric field.

In the valence band spectra shown in Figure 2 we observe a sharp peak labelled n located at binding energy of -2.9 eV, a broader peak B at -6.2 eV, and a shoulder S_1 at lower binding energy (-0.84 eV). The latter two peaks were attributed to InAs bulk emission, and to surface states related to the 2×1 (the unit cell is $8.6 \text{ \AA} \times 17 \text{ \AA}$) surface reconstruction of InAs(001)- (4×2) [1,2,9], respectively. The strong surface state emission n appeared only when the LEED pattern showed the $c(4 \times 4)$ and (4×2) reconstructions and was obviously absent on the unreconstructed surface, which does not show any surface feature. It is worth noting that the observation of acute peaks on confined structures has not been reported for one-dimensional structures although Loly and Pendry [10] point out in their theoretical study that photoemission from thin films should reveal a set of sharp peaks. Measurements performed at normal emission (not reported here) for photon energy range from 20 to 200 eV confirmed that S_1 and n are surface state derived peaks.

In order to get the dispersion of peaks n , we performed ARPES measurements by scanning K vector *in*- and *off* the plane of incidence. Figures 3a and 3b, report the k -dispersion of n peak collected on InAs(001)- (4×4) reconstruction along [0-11] and [011] directions respectively at $\pm 1^\circ$, $\pm 2^\circ$ and $\pm 3^\circ$. The spectra at higher angles showed the same behaviour. Surprisingly no dispersion was observed for the peak n for both k - directions. This non-dispersive behaviour of peak n can be tentatively

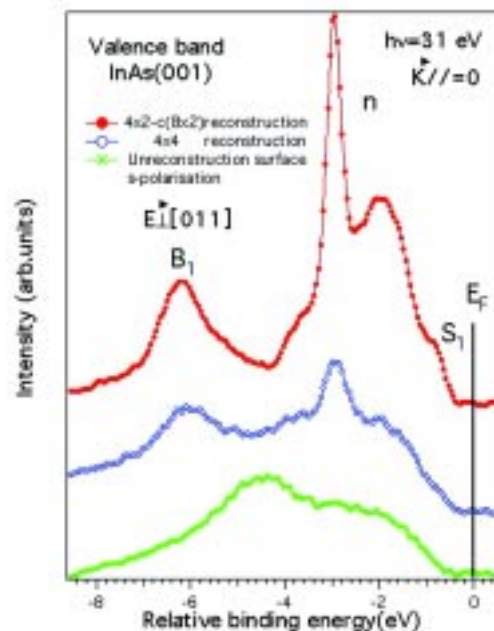


Figure 2. Valence band photoelectron spectra collected on the InAs(001) unreconstructed sample, InAs(001)- $c(4 \times 4)$ and $-(4 \times 2)$ surface reconstructions at photon energy of 31 eV. The Fermi level energy is indicated.

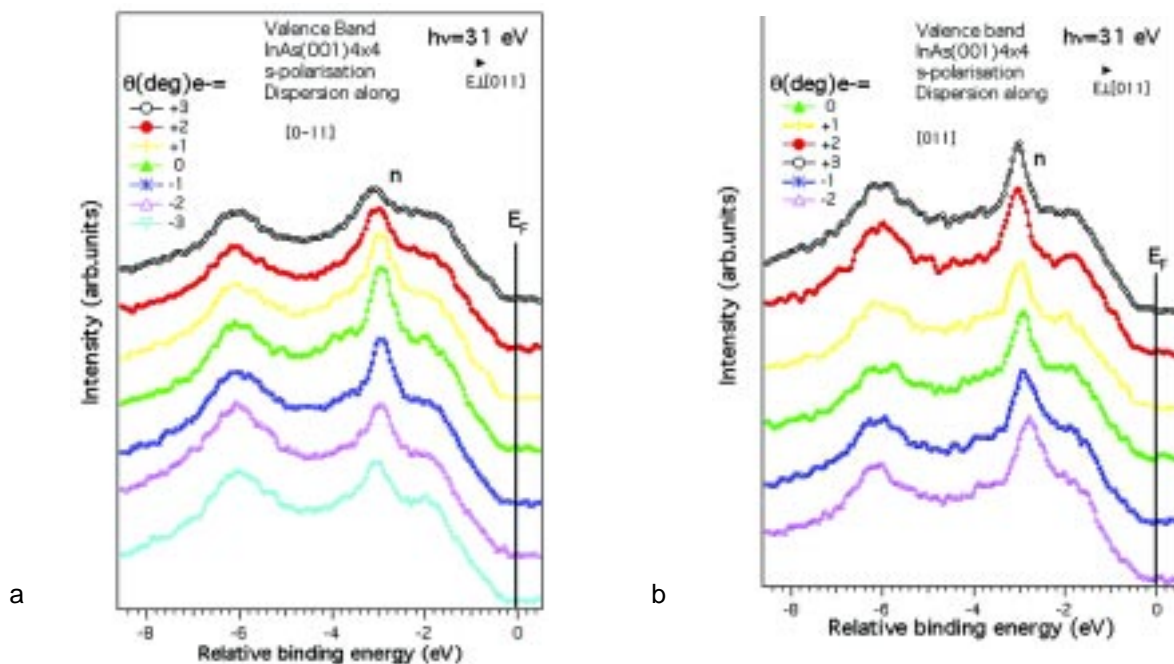


Figure 3. ARPES spectra collected on the InAs(001)-c(4x4) clean surface. *K*-dispersion of peak along [0-11] (a), and along [011] direction (b). The Fermi level energy is indicated.

explained by c(4x4) chess-board-like atom arrangement suggesting that the electron motion is confined by the short length of the surface structure.

At variance, in the case of InAs(001)-(4x2) surface *k*-dispersion of *n* peak (not reported here) shows a non-dispersive behaviour along the [0-11] direction which is perpendicular to the In-rows, and a *free electron-like* dispersion travelling toward the Fermi level in [011] direction (parallel to the rows). This behaviour is typical for the one-dimensional structures [11,12], as expected for the rows of In atoms present in the InAs(001)-(4x2) surface reconstruction. Applying the well known equation $K_{||} = 0.512 \sqrt{E_{kin}} \sin(\vartheta_e)$ to calculate the *lattice parameter* connected to the periodicity of this dispersion, we obtain $a = 3.6 \text{ \AA}$ which is in good

agreement with the value obtained by STM measurements [1] for the distance between the In atoms in rows on the InAs(001)-(4x2) surface.

CONCLUSIONS

In conclusion, two reconstructions of clean In-terminated InAs(001) surfaces were studied by LEED, high-resolution core-level and valence band spectroscopies. A new InAs(001)-c(4x4) In-terminated reconstruction was identified, and original photoemission structures associated to the emission from low-dimensional structures were observed.

The authors thank the staff of ELETTRA and that of the VUV beamline.

REFERENCES

- [1] P. Drathen, W. Ranke, K. Jacobi, Surf. Sci. 77 (1978) L162
- [2] C.F. McConville et al., Phys. Rev. B, 50 (1994) 14965
- [3] C. Kendrick, et al., Phys. Rev. B, 54 (1996) 17877
- [4] P. De Padova et al. Surf; Sci. 482 (2001) 587
- [5] D. K. Biegelsen et al. Phys. Rev. B. 41 (1990) 5701
- [6] H. Yamaguchi and Y. Horikoshi, Phys. Rev. B, 48 (1993) 2807
- [7] M. J. Ekenstedt, H. Yamaguchi and Y. Horikoshi, Appl. Phys. Lett. 67 (1995) 3848
- [8] J. Noreika, M. H. Francombe, and C. E. C. Wood, J. Appl. Phys. 52 (1981) 7416
- [9] M. C. Håkansson et al. Surf. Sci. 374 (1997) 73
- [10] P. D. Loly, and J. B. Pendry, J. Phys. C: Solid State Phys. 16 (1983) 423
- [11] S. Segovia et al. Nature, 402 (1999) 504
- [12] C. Pampuch et al. Phys. Rev. Lett. 85 (2000) 2561

Strong spin-filter effects observed in high-resolution photoemission from Cu(100) with circularly polarized light

R. Frömter

Institute of Applied Physics, University of Hamburg, Germany

S. Legner, S.V. Borisenko, M.S. Golden, F. Matthes, C.M. Schneider

Institute of Solid State and Materials Research IFW Dresden, Germany

S. Zennaro, S. Turchini

ICMAT-CNR, Italy

INTRODUCTION

The detailed electronic structure of solids is substantially affected by spin-dependent interactions. This holds even for nonmagnetic materials where spin-dependent effects come about by spin-orbit coupling. Usually, these effects are thought to be relevant mostly for heavy elements (high atomic number Z) where the spin-orbit coupling is large. The spin-orbit coupling leads to characteristic band splittings and may also hybridize states of different spatial symmetry characters. In addition, it provides also a unique spectroscopic approach, which is known as *optical spin orientation* and basically relates to a spin-dependence of the optical interband transition matrix elements [1]. This phenomenon forms the basis of spin-resolved photoemission experiments from nonmagnetic materials [2]. Circularly polarized (c.p.) light has been shown to be a suitable tool to excite spin-polarized electrons in nonmagnetic crystals [1] and to study these effects. However, the influence of the electron spin is not limited to the photoexcitation step only. It has been demonstrated that the probability for an excited photoelectron to pass through a surface on its way to the detector may also markedly depend on the spin. This phenomenon is known as spin dependent transmission (SDT) [3] and is associated with the matching of the half-space Bloch waves in the crystal to the free-electron states in the vacuum in the presence of spin-orbit coupling. As a peculiar feature, studying SDT or *spin-filter* effects yields access to spin-dependent phenomena in the electronic structure on the basis of simple *intensity measurements*. On Pt(111) surfaces transmission (intensity) asymmetries in excess of 45 % along low symmetry directions have been found [4]. However, for metals with small

spin-orbit coupling like Cu so far only intensity asymmetry values of $\sim 3\%$ have been reported [5]. Because in the latter case the spin-orbit induced energy splitting of the states is small, the small asymmetry value may be due to a limited energy resolution in these experiments (~ 250 meV), or to a weak spin-dependent scattering at the surface.

EXPERIMENTAL METHODS

In order to clarify this situation we performed systematic k -space mapping experiments on a clean Cu(001) surface using a high-resolution analyzer (Scienta SES-100) at the electromagnetic wiggler/undulator beamline 4.2 R. The instrument provides simultaneous mapping of an 8° wide angular slice and was set to give an angular resolution of 0.3° with an energy resolution of 30 meV.

RESULTS AND DISCUSSION

The data shown below represent angular intensity distribution plots taken at 17.5 eV photon energy at emission angles away from high-symmetry directions. ϕ denotes the azimuthal rotation relative to the $\langle 110 \rangle$ in-plane surface direction and J the polar angle with respect to normal emission. The panels on the left hand side compare intensity spectra taken with left- (I^+) and right c.p. light (I^-), respectively. The bright bands in the angular map can be attributed to the excitation of distinct initial state bands in the Cu band structure dispersing with k . Already from the intensity spectra a marked difference is conceivable: In the I^\pm spectrum one of the two bands around 2.5 eV binding energy is largely missing. This

can be seen in more detail in the asymmetry map (reflecting directly the (E, ϑ) variation of the intensity difference, or equivalently, the SDT effect) and the extracted line scan in the right hand panel.

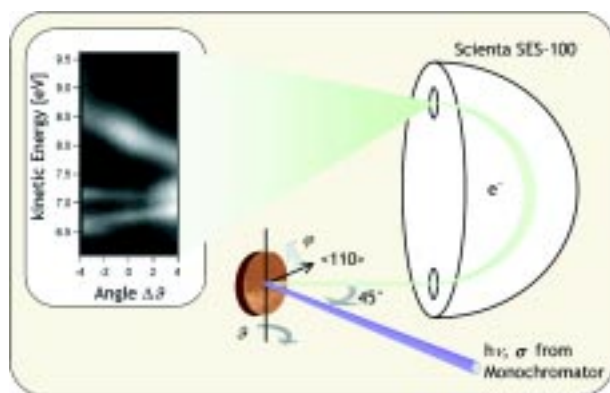


Figure 1. Schematic sketch of the experimental setup

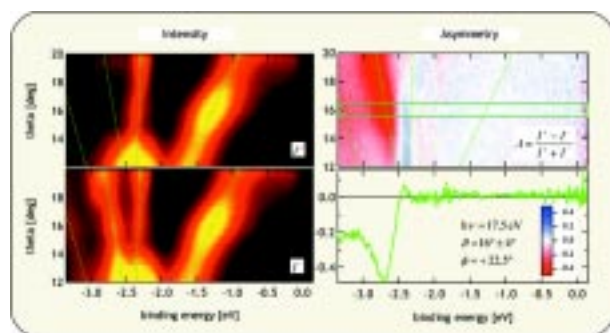


Figure 2. Angular maps of the intensity distribution for left and right circularly polarized light together with a calculated asymmetry map enhancing the intensity differences. The profile is taken from the marked region of the asymmetry map.

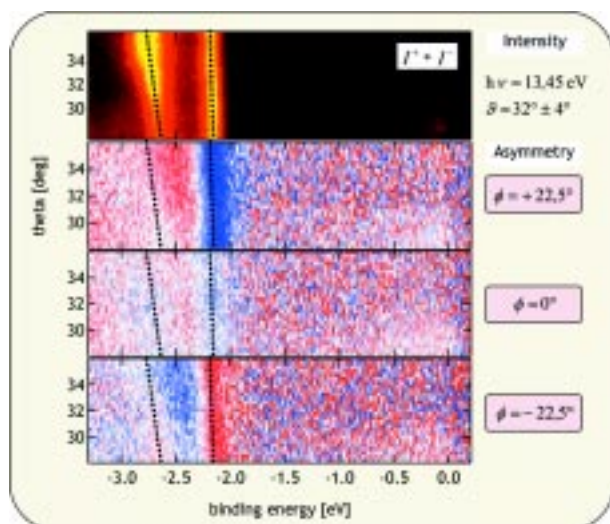


Figure 3. The effect of azimuthal rotation on the intensity asymmetry, reflecting the symmetry properties of the effect.

While the strongly dispersing structure at 1.5 eV binding energy, which mainly involves sp -type initial states and is thus not affected by spin-orbit coupling, shows no asymmetry at all, we find huge changes up to 50 % asymmetry in the states around 2.5 eV binding energy. These transitions predominantly involve d -like initial states, which are split and hybridized by spin-orbit coupling. Following the angular variation of the bands, the two states at around 2.5 eV binding energy can be traced to a spin-orbit split pair of bands of Δ_6^5 and Δ_7^5 relativistic symmetry along the $\langle 001 \rangle$ direction. Considering the degree of circularity of the incoming photons, which at these photon energies is about 70 %, the original effect in the asymmetry must be even larger. We also note that at some regions the asymmetry changes sign along a band within less than 1° of change in J . The origin of these changes is not yet clear, but is attributed to electronic hybridizations close to a band crossing.

The second panel of data shows an experiment in which the azimuth φ is varied around the in-plane $\langle 110 \rangle$ high-symmetry surface direction which represents a mirror plane. At the emission angle and photon energy chosen only the two d -state transitions mentioned above show up in the intensity map. Of these two features the one located at around 2.2 eV exhibits a pronounced asymmetry of about 40 % when viewed at $\phi = 22.5^\circ$. This contrast can be largely eliminated by rotating the sample into the mirror plane, and it is found to be inverted by a further rotation to $\phi = -22.5^\circ$. Such a behavior is in accordance with the predicted behavior of the spin-filter effect due to symmetry arguments: the intensity asymmetry A becomes maximum for emission directions in between mirror planes and vanishes for emission angles within the mirror plane [4].

From these symmetry considerations follows immediately another property of the intensity asymmetry A : for a fixed azimuthal angle ϕ the asymmetry should change sign when going from J

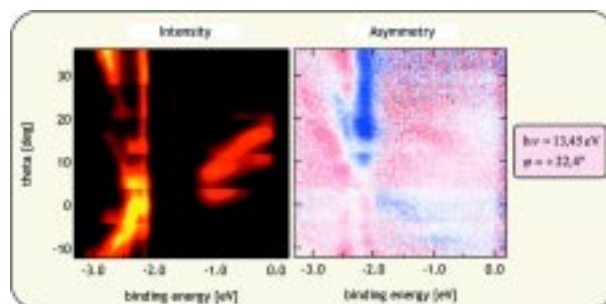


Figure 4. The effect of continuously varying the emission angle ϑ .

to $-\vartheta$. This inversion was verified by a series of angular maps with a continuous variation of ϑ and crossing the Γ -X line at normal emission.

CONCLUSIONS

The use of circularly polarized radiation together with high-resolution angular mapping spectroscopy

promises unprecedented insight into the band structure of matter and provides high-quality experimental data for the detailed comparison with advanced numerical methods. The results for Cu(001) prove that the various spin-dependent effects in photoexcitation and surface scattering are very important also in low- Z materials. They can give rise to huge intensity modulations if an appropriate energy resolution is available in the experiment.

REFERENCES

- [1] F. Meier and D. Pescia, in *Optical Orientation*, ed. by F. Meier and B.P. Zakharchenya (North-Holland, Amsterdam, 1984), p. 296
- [2] C.M. Schneider and J. Kirschner; *Critical Reviews in Solid State and Materials Sciences*; 20, 179, (1995)
- [3] H.P. Oepen, K. Hünlich and J. Kirschner; *Physical Review Letters*; 56, 496, (1986)
- [4] J. Garbe and J. Kirschner; *Physical Review B*; 39, 9859, (1989)
- [5] D. Venus, W. Kuch, A. Dittschar, M. Zharnikov, C. M. Schneider and J. Kirschner; *Physical Review B*; 52, 6174, (1995)

Photoemission lineshape at finite temperature

Ch. Søndergaard, Ch. Schultz, Ph. Hofmann

Institute for Storage Ring Facilities, University of Aarhus, 8000 Aarhus C, Denmark

S. Moreno, J.E Gayone, M.A. Vicente Alvarez, G. Zampieri

Centro Atómico Bariloche and Instituto Balseiro, Comisión Nacional de Energía Atómica, 8400 Bariloche, Argentina

S. Lizzit, A. Baraldi

Sincrotrone Trieste S.C.p.A, 34012 Trieste, Italy

INTRODUCTION

Recent experimental progress in photoemission has led to such an improvement of the achievable resolution that it is now possible to directly access the lineshape of the photoemission features without having to worry about experimental broadening. This lineshape can be linked to one of the most fundamental properties in solid state physics, the so-called spectral function [1]. The analysis of photoemission features in terms of a spectral function has led to important new insight into the physics of some systems, in particular materials with strong electron-phonon coupling and high temperature superconductors [2]. Very recently, it has even become possible to measure high-resolution photoemission data at high photon energies [3]. In this regime, the electron mean free path is long and the contribution of the surface electronic structure to the spectra becomes small, a highly desired effect if one is interested in bulk properties.

As we shall see in more detail below, the photoemission intensity and lineshape at high energies and/or high temperature is severely influenced by phonon scattering, i.e. by the interaction of the outgoing photoelectron with the vibrations of the lattice. It is easy to see the reason why this happens: Photoemission can be viewed as a scattering process. Constructive interference gives rise to so-called direct transition peaks in the photoemission intensity which can be used to map the band structure of the solid. At finite temperature, the photoelectron wave sees a lattice which is distorted by the vibrations of the atoms and this destroys the interference conditions. The effect of the distortion is increased by larger vibrational amplitudes (higher temperature) or a shorter wavelength of the photoelectron (a higher kinetic energy) or both.

Here we present a combined experimental and

theoretical study of the energy and temperature-dependent photoemission intensity from Al(100). It turns out that our calculations are quantitatively describing the experimental findings. Furthermore,

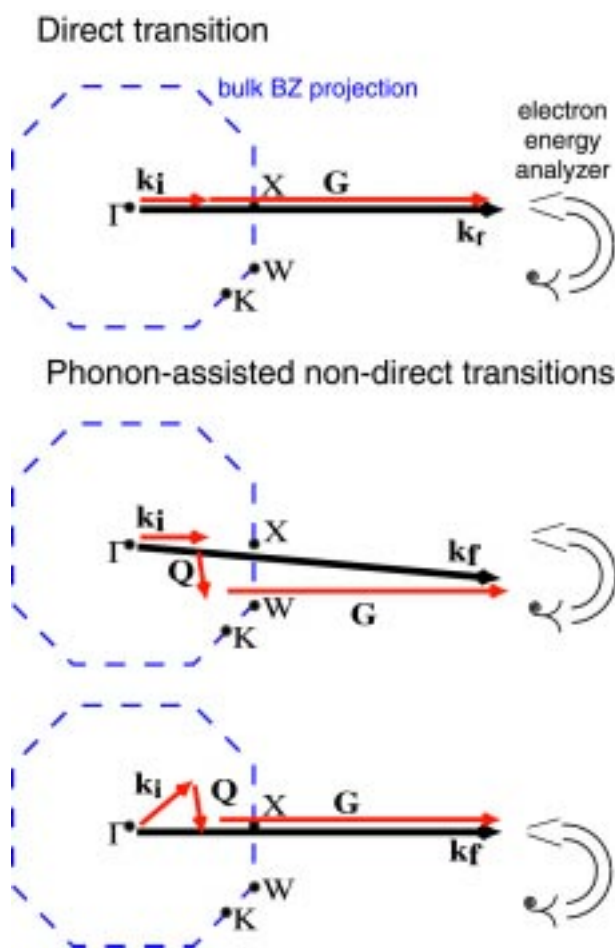


Figure 1. Possible processes when considering the possibility of phonon scattering in the photoemission event. Top: direct transition without phonon scattering. Middle: phonon scattering event which diminishes the direct transition intensity. Bottom: event which scatters states from other parts of the Brillouin zone into the emission direction and increases the intensity of non-direct transitions.

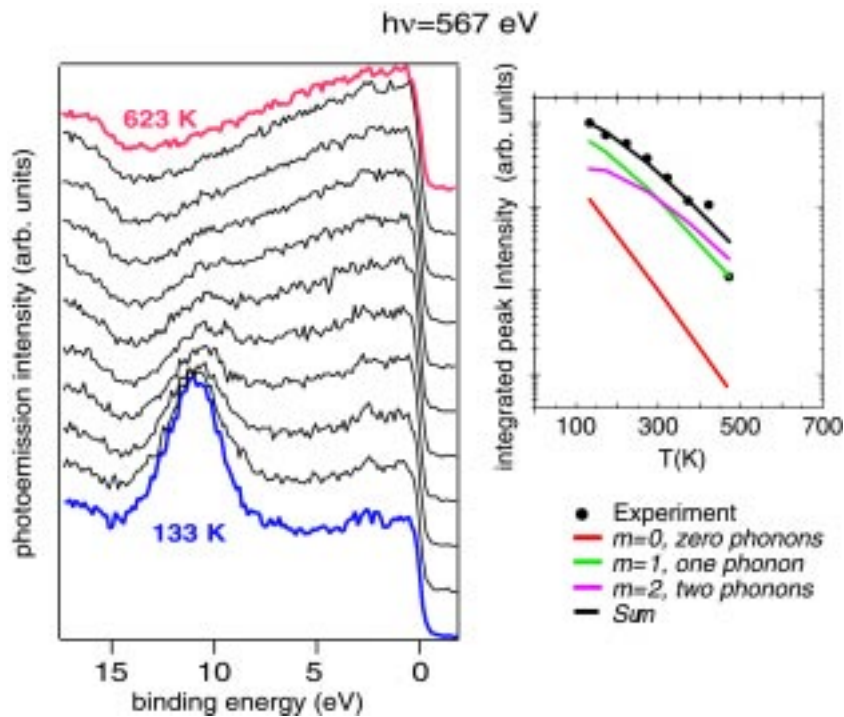


Figure 2. Left: photoemission spectra in normal emission from Al(100) taken as a function of temperature. Right: Integrated peak intensity from this data (points) compared to the calculated intensity for photoemission involving $m=0, 1, 2$ phonon scattering events, as well as to the sum of all three.

it is found that phonon scattering can have a severe effect on the photoemission lineshape at high energies and/or high temperatures. The details of this study are published in ref. [4].

PHONON SCATTERING IN PHOTOEMISSION

In Figure 1 we show what can happen if a photoelectron is scattered by the phonons of the crystal. The energy of the phonons is negligible in this context and so we just concentrate on the scattering in momentum space. An angle-resolved electron analyser is placed at normal emission above the (100) surface of an fcc crystal, i.e. such that the emission direction corresponds to the G-X direction in the bulk Brillouin zone. In the topmost part of the figure, an electron with momentum \mathbf{k}_i on the Γ -X line is excited by a photon and emitted along this direction. The momentum difference between \mathbf{k}_i and the final state wave vector \mathbf{k}_f is provided by the lattice in form of a reciprocal lattice vector \mathbf{G} . This process causes the so-called direct transition peaks in photoemission. In the lower part of the figure, two photoemission processes involving scattering from a phonon with wave-vector \mathbf{Q} are shown. In the first case, the phonon scatters the electron out of the emission direction. This process decreases the direct

transition intensity. In the second case, an electron with a \mathbf{k}_i not in the Γ -X direction is scattered by a phonon such that it is emitted in normal emission and detected by the analyser. This type of process increases the so-called non-direct transition intensity. Of course, there are also more complicated processes involving many phonons. Qualitatively, however, increasing the importance of phonon scattering via

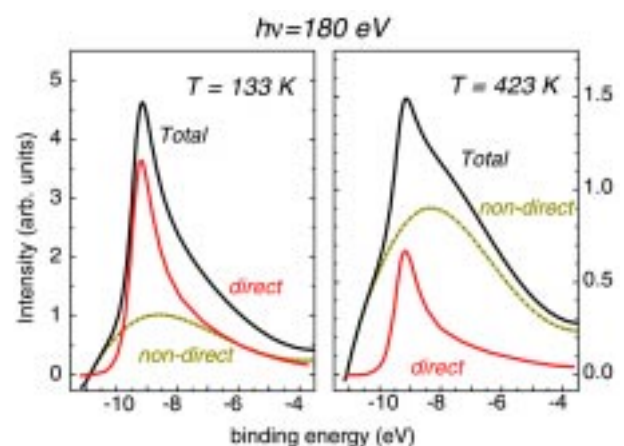


Figure 3. Calculated spectra corresponding to photoemission from Al(100) in normal emission for two different temperatures. Along with the spectra we present their decomposition into the contribution from direct and non-direct transitions.

the temperature or energy leads to an increase of the non-direct transition intensity at the expense of the direct transitions. This can be described roughly by a Debye-Waller factor [5].

RESULTS AND DISCUSSION

The experiment was carried out at the SuperESCA beamline of ELETTRA. The left part of Figure 2 gives the result of a temperature-dependent photoemission measurement in normal emission from Al(100) at a photon energy of 567 eV. The spectra taken at low temperature show a pronounced peak at about 11 eV binding energy. This is the so-called direct transition peak. As the temperature is raised, the peak is decreasing and eventually vanishing. We have simulated this using a model that allows to calculate the photoemission intensity for transitions with the simultaneous excitation/absorption of $m=0, 1, 2$, etc. phonons [6]. The right part of Figure 2 shows the comparison between the measured peak intensity and this calculation. The agreement between the experimental data and the calculated direct-transition intensity, i.e. the $m=0$ component, is not very good since the zero phonon result falls off much too fast. However, a good agreement between experiment and theory can be achieved by comparing the measured intensity to the sum of the zero phonon calculation and the calculated intensity involving one and two phonon scattering events. This seems to suggest that the so-called direct transition peak in photoemission actually contains a considerable contribution from transitions involving the scattering by one or two phonons, i.e. transitions which are non-direct.

We have checked this by simulating actual photoemission spectra, i.e. by calculating the photoemission intensity for a certain photon energy and temperature as a function of binding energy. Figure 3 shows the result of such a calculation for a photon energy of 180 eV and two temperatures, 133 K and 423 K. The spectra have been decomposed into the intensity which is caused by direct transitions and the sum of all non-direct transitions. As expected,

the relative intensity of the non-direct transitions increases with temperature such that at 423 K the spectrum is dominated by non-direct transition intensity. At the same time, however, it is clearly visible that the non-direct part of spectrum is not flat but rather shows a peak at an energy similar to that of the direct transition. A further decomposition of the non-direct intensity into contributions from 1,2,3... phonons shows that this peak is mainly caused by the scattering events involving one and two phonons. This finding explains why we had to take the sum of the $m=0,1,2$ phonon intensity in order to satisfactorily reproduce the measured direct transition peak intensity in Figure 1.

While this result seems to be surprising at first sight, it can be explained in very simple terms. The most important phonon scattering events involve phonons near the centre of the Brillouin zone, i.e. close to the Γ point [5]. These phonons do not only have a very small energy, their momentum Q is also very small. Figure 1 reveals that in such a case the direction of the photoelectron is almost unchanged and the phonons will scatter states into the emission direction which are very close and similar to the state producing the direct transition peak. Indeed, these processes are very similar to a direct transition which could also be viewed as a phonon scattering process, namely with a phonon of zero energy at the Γ point (or a reciprocal lattice vector).

CONCLUSIONS

The main conclusion from this work is that the so-called direct transition peak in photoemission contains contributions from transitions which involve the scattering by one or two phonons, i.e. transitions which are actually indirect. At high temperatures and/or high photon energies these contributions may even become dominant. This can have a major influence on the photoemission lineshape, as seen in Figure 3. The strong contributions of non-direct transitions to the so-called direct transition peak change its apparent position, width and lineshape.

REFERENCES

- [1] G. D. Mahan and E. W. Plummer in *Handbook of Surface Science* (eds. K. Horn and M. Scheffler) Elsevier Science Pub., (2000).
- [2] A. Lanzara, P. V. Bogdanov, X. J. Zhou, S. A. Kellar, D. L. Feng, E. D. Lu, T. Yoshida, H. Eisaki, A. Fujimori, K. Kishio, J.-I. Shimoyama, T. Nodak, S. Uchidak, Z. Hussain and Z.-X. Shen; *Nature*; 412, 510 (2001) and references therein.
- [3] A. Sekiyama, T. Iwasaki, K. Matsuda, Y. Saitoh, Y. Ônuki and S. Suga; *Nature*; 403, 396 (2000)
- [4] C. Søndergaard, P. Hofmann, C. Schultz, M. S. Moreno, J. E. Gayone, M. A. V. Alvarez, G. Zampieri, S. Lizzit and A. Baraldi; *Phys. Rev. B*; 63, 233102 (2001)
- [5] N. J. Shevchik, *Phys. Rev. B*; 16,3428 (1977)
- [6] M. A. Vincente Alvarez, H. Ascolani and G. Zampieri, *Phys. Rev. B*; 54, 14703 (1996)

Direct experimental evidence of insensitivity of local Schottky barriers to lateral chemical inhomogeneity in case studies of metal/GaN(0001) interfaces

A. Barinov, L. Gregoratti, B. Kaulich, M. Kiskinova
Sincrotrone Trieste, 34012-Trieste, Italy

Our spectromicroscopy studies have been motivated by reports in which lateral variations of the electronic properties of metal/GaN interfaces, induced by the defect structure of the GaN films, are held responsible for the unstable performance of technologically important GaN-based devices [1]. X-ray photoelectron spectroscopy with submicrometer spatial resolution is capable of probing both the local composition of the metal/semiconductor interface, monitoring the evolution of the metal, Ga and N photoelectron spectra and the corresponding band bending at the surface, monitoring the energy shift of the N 1s and/or Ga 3d core levels of the GaN substrate.

Figure 1 shows selected images of defect regions at Ni/GaN and Ti/GaN interfaces [1, 2]. The two metals behave quite differently when they interact chemically with GaN: Ti forms nitride compounds, whereas Ni alloys with Ga and forms gallides. In both cases the best fingerprint for the local reactivity is the amount of the released Ga, which is easily distinguished as a new component, R-Ga, in the Ga 3d spectra. Depending on the annealing temperature, the nitrides and gallides at the interface change their stoichiometry, best reflected by the binding energy and relative weight of the R-Ga component. The images in Figure 1 clearly manifest the presence of chemical heterogeneity. In both cases more vigorous interfacial reaction has occurred at the ‘defect’ areas, which also become enriched with Ni or Ti.

The most peculiar finding is that we measured negligibly small SBH lateral variations despite the composition difference between the defect and non-defect areas. The negligible influence of the chemical lateral heterogeneity on the local band bending appears to be a characteristic feature of metal/GaN interfaces, and was also observed most recently at composite Au, AuTi interfaces, where the Au and AuTi metallic layers were in contact [2-5].

None of the existing models can easily explain the lateral variations of the microscopic morphology on both the metal and semiconductor sides of the interface, on a length scale larger than the width of the depletion zone, and the almost homogeneous band bending. We tentatively interpret our findings in terms of charge redistribution leading to homogenization of the SB fluctuations at the semiconductor surface. The driving force for such event can be the potential bias created between the

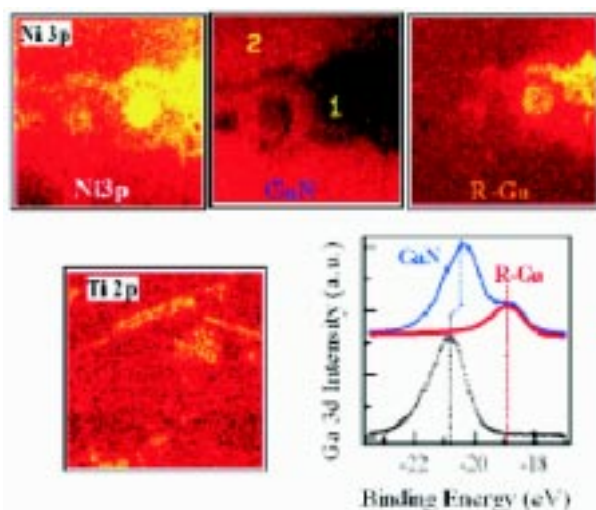


Figure 1. 25x25 μm² images of defect regions at Ni/GaN (top) and Ti/GaN (bottom) interfaces, illustrating the local enrichment with metal and the higher local reactivity, manifested by mapping the R-GaN component. The Ga 3d spectra below are measured for a clean GaN and on a reacted Ni/GaN interface. The shift of the Ga 3d component corresponding to GaN reflects the band bending, whereas the interfacial interaction leads to an appearance of R-Ga component.

Direct experimental evidence of insensitivity of local Schottky barriers to lateral chemical inhomogeneity in case studies of metal/GaN(0001) interfaces

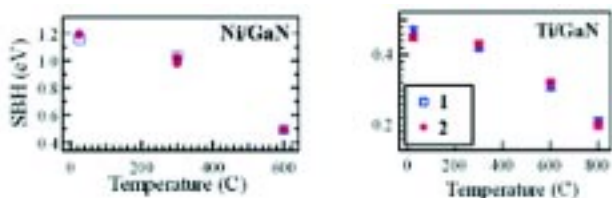


Figure 2. Schottky barriers as a function of temperature measured in defect (1) and non-defect areas (2) of Ni/GaN and Ti/GaN interfaces.

adjacent areas with different Schottky barriers. In the presence of sufficient free carriers at the surface, which can be expected for a metallized semiconductor interface a charge exchange will occur tending to reduce the potential difference. It should

be noted that our method is extremely surface sensitive and probes the band-bending at the semiconductor surface. For the doping levels of our samples the width of the charge space layer is of the order of 100 Å, so that we do not exclude different potential contour profiles of the space charge region below the semiconductor surface. This simple ‘charge transfer across the surface’ scenario implies a lack of Fermi-level pinning within the GaN band gap, which is in accordance with the recent theoretical studies of metal/GaN interfaces [6].

Systematic investigations of other metal/semiconductor systems are necessary to find out if the insensitivity of band bending at semiconductor surfaces to the microscopic interfacial morphology is limited to metal/GaN interfaces or is a more general phenomenon.

REFERENCES

- [1] S.C. Jain et al, J. Appl. Phys. 67, 965 (2000).
- [2] A. Barinov et al, Phys. Rev. B 63, 85308 (2001).
- [3] A. Barinov et al, Appl. Phys. Lett. (in press).
- [4] A. Barinov et al, submitted.
- [5] A. Barinov et al, in preparation.
- [6] S. Picozzi et al, Phys. Rev. B 61, 16736 (2000).

Coherence and correlation effects in indirect double photoionization

S. Rioual and B. Rouvellou

UFR Sciences and Techniques, Université de Brest, France

L. Avaldi, G. Battera, R. Camilloni

CNR-IMAI, Area della Ricerca di Roma, Italy

G. Stefani

Unita' INFN and Dipartimento di Fisica, Università di Roma Tre, Roma, Italy

G. Turri

INFN TASC and Dipartimento di Fisica, Politecnico di Milano, Italy

INTRODUCTION

The description of the dynamics of few charged particles in the continuum and the study of coherence are two amongst the most debated topics in quantum mechanics. The former, even in its simplest case of three Coulomb-interacting particles in the continuum, is a very challenging theoretical problem. As far as the latter is concerned, observations of coherence can be performed in atomic physics when

the interaction between an atom and a photon proceeds through indistinguishable channels leading to the same final state. Here the experimental challenge is to achieve an overall energy resolution comparable with the width Γ of the intermediate states. This is mandatory in order to observe the interference effects typical of coherence. The process of indirect double photoionization (DPI) offers the opportunity to investigate these two topics in the same experiment.

Quantum coherence

Coherence and quantum entanglement are subjects currently under intense discussion. They can arise from the “democratic” nature of quantum mechanics, that is, that quantum particles such as electrons are exactly equal and indistinguishable. The only way of telling them apart is to give them different “identity cards” or quantum numbers. Then a high energy electron can be distinguished from a low energy electron, one spinning fast from one spinning slowly, etc. However, interesting things can happen due to this indistinguishability if an experimenter creates two coherent electrons.

This has been tried at ELETTRA by photoemission, in which a photoelectron is ejected from the core of an atom. Very shortly afterwards, in fact a few femtoseconds later, the atom gets rid of its excess energy by

ejecting a second electron, the Auger electron, which has a fixed energy. For most photon energies, these two electrons have different kinetic energy and so one can identify the Auger electron (of fixed kinetic energy) and the photoelectron (whose energy varies with the photon energy). Synchrotron light is tunable, and so at one particular photon energy, the energy of the photoelectron can be adjusted to be equal to that of the Auger electron. Now it is no longer clear which is the Auger and which is the photoelectron, and the spectrum changes suddenly – the two electrons interfere, as described in the research below. This shows that the electrons are ejected coherently, that is, that there is a relationship between the wave functions of the two electrons that are moving away from the atom.

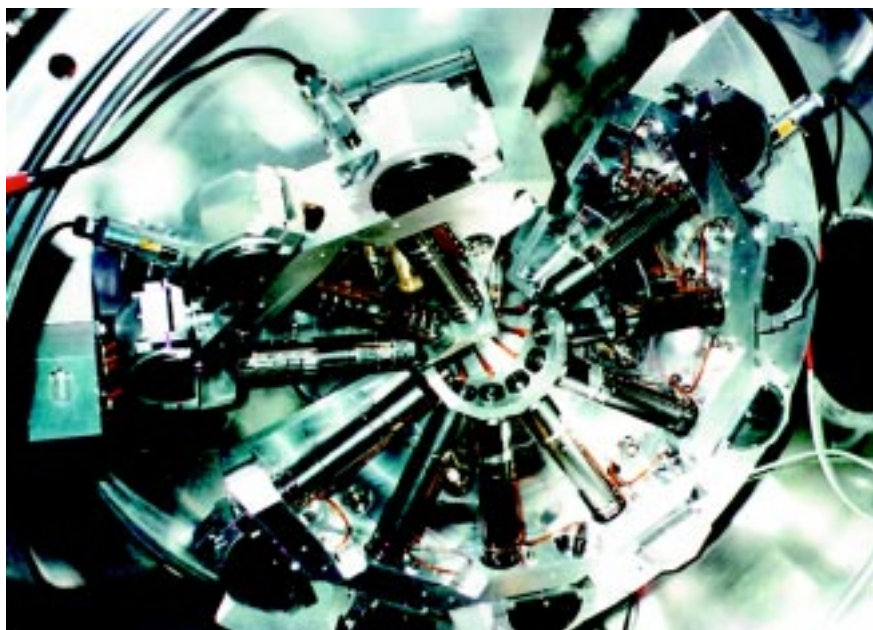
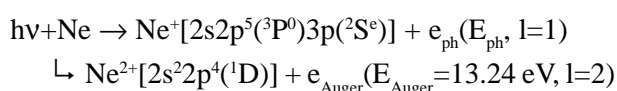


Figure 1. The multicoincidence end-station with the two turntables and the electron spectrometers.

DPI involves three charged interacting particles in the final state, thus it represents a typical three-body Coulomb problem. The indirect DPI is characterized by the formation of an excited state of the singly charged ion that may decay into the double continuum. Usually the emission of the photoelectron and the Auger electron is treated within the two-step model, made up by two incoherent successive processes. A rather interesting case emerges by considering the tunability of synchrotron radiation which allows the production of photoelectrons with a kinetic energy close to the energy of the Auger electrons. In this case, due to electron exchange, strong interference effects are expected in the angular and energy distributions of the two outgoing electrons [1]. The two electrons can not be specified as photoelectron or Auger electron. The two-step model does not hold any more and the intermediate state has to be considered as a resonance embedded in the double continuum. Moreover when electrons of nearly the same energy are ejected at small mutual angles, their angle and energy distributions can be seriously distorted by the Coulomb interaction in the final state. This phenomenon is known in the literature as Post Collision Interaction (PCI) [2].

The most suited experiment to investigate the effects of coherence and PCI in indirect DPI is a measurement in which the two free electrons are detected in coincidence after energy and angular selection. We have studied a selected case of indirect double photoionization of Ne



In our coincidence experiments the photo- and Auger-electron pair was measured when the two electrons have nearly equal energy and at different mutual angles in order to enhance the interference and PCI effects.

EXPERIMENTAL METHODS

The measurements have been performed at the Photoemission Gas Phase beamline using the electron-electron multicoincidence end-station [3]. The light source of the beamline is a 4.5 m undulator of 12.5 cm period. The beamline is equipped with a variable angle spherical grating monochromator which provides radiation over the range 20-1000 eV with a resolving power higher than 10000. The multicoincidence end station houses two independently-rotatable arrays of electrostatic electron energy analysers located in the plane perpendicular to the photon beam direction and containing the polarisation vector (fig. 1). Each analyser is composed of two four-element lenses, a hemispherical deflector and a channeltron electron multiplier. The lenses focus the electrons from the target region onto the entrance slits of the hemispherical deflector. The energy resolution in the non coincidence measurements was about 75 meV. This value, smaller than the natural width of the $\text{Ne}^+ [2s2p^5(^3P^0)3p(^2S^e)]$ state ($G = 155 \text{ meV}$ [4]), complies with the condition stated to observe interference effects in coincidence experiments [1]. The experimental set-up allows us to simultaneously collect in coincidence up to 21 pairs of electrons with

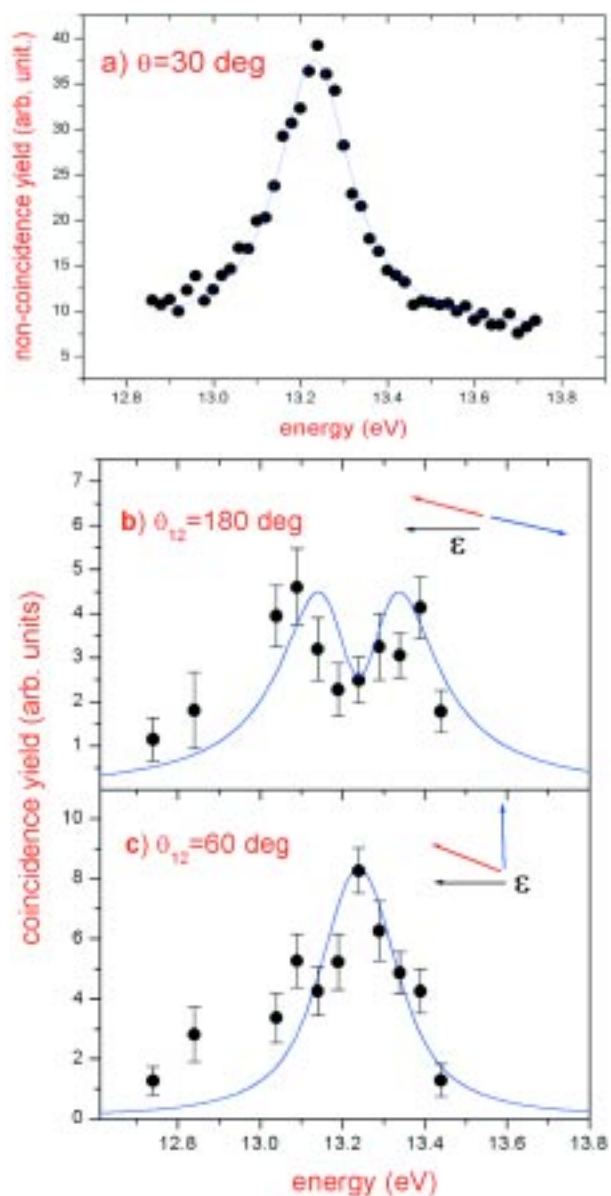


Figure 2. Non coincidence electron spectrum at $h\nu=92.21$ eV (a). Photoelectron-Auger electron coincidence spectrum at the same photon energy for $\vartheta_{12}=180^\circ$ (b) and 60° (c). The lines are a fit with a Voigt lineshape to the experiments in (a) and with the general formula by Vegh and Macek [1] convoluted with the apparatus function in (b) and (c).

the mutual J_{12} angle varying from 30° to 180° . Thus, while scanning the kinetic energy of the two electrons, both energy and angular coincidence distributions can be simultaneously measured.

RESULTS AND DISCUSSION

In the first experiment a photon energy of 92.21 eV has been chosen. The binding energy of the Ne^+ [$2s2p^5(^3P_o)3p^2S_o$] state is 78.97 eV so in this

experiment the kinetic energies of the two electrons are equal, i.e. $E_{\text{ph}}=E_{\text{Auger}}=13.24$ eV. Figure 2a shows the non-coincidence electron spectrum measured at this photon energy and at $\vartheta=30^\circ$ with respect to the direction of the polarisation of the incident light. The shape of the feature, due to the overlap of the photoelectron and Auger peaks, as well as its position does not change with the detection angle. Figures 2b and 2c show the coincidence energy distribution measured at $\vartheta_{12}=180^\circ$ and 60° , respectively. In the measurements the kinetic energies of the two electrons were varied according to the relationship: $h\nu\text{-IP}[\text{Ne}^{2+}(^1D)]=E_1+E_2$, where E_i ($i=1,2$) is the kinetic energy of one of the two electrons. Despite the statistical uncertainty the data display a quite different shape at the two ϑ_{12} . The spectrum taken at $\vartheta_{12}=180^\circ$ clearly shows a minimum when $E_1=E_2=13.24$ eV $=E_{\text{Auger}}$. According to the model of Vegh and Macek [1] this behaviour can be qualitatively understood as the signature of the interference effect, which depends on the total spin and parity of the

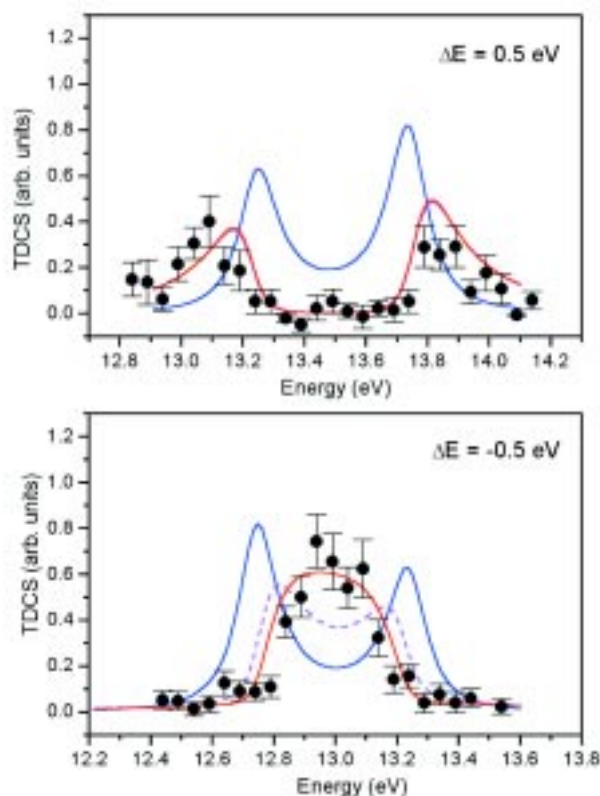


Figure 3. Photoelectron-Auger electron coincidence spectra at $h\nu=92.71$ eV, i.e. $\Delta E=0.5$ eV (top), and $h\nu=91.71$ eV, i.e. $\Delta E=-0.5$ eV (bottom), for $\vartheta_{12}=30^\circ$. The experiment is compared with the calculations without PCI effects (blue line), with PCI effects without interference effects (dashed red line) and with both effects (red line).

electron pair. In the LS coupling scheme, for the Ne^{2+} ($^1\text{D}^o$) final state only three ($^1\text{P}^o$, $^1\text{D}^o$, $^1\text{F}^o$) electron pair configurations are allowed. They are of unfavoured type and lead to a node for antiparallel emission. Therefore the theoretical description predicts destructive interference for antiparallel emission ($\vartheta_{12}=180^\circ$) and constructive interference for the opposite condition of parallel emission. These predictions (full line in fig. 2a and b) are completely consistent with our experimental observation.

The second set of measurements has been devoted to investigate the combination of PCI and interference effects. To the purpose the photon energy has been fixed to select a detuning $\Delta E = E_{\text{ph}} - E_{\text{Auger}} = +0.5$ or -0.5 eV and the mutual angle to the minimum achievable value, i.e. $\vartheta_{12}=30^\circ$. The same experimental procedure used in the previous experiment has been adopted. The results are shown in Figure 3a and b for the case of $\Delta E = +0.5$ and -0.5 eV, respectively. In such a coincidence energy distribution, when interference and PCI effects are not taken into account, one would expect two peaks centred at energy positions of the photo-line (13.74 eV) and Auger-line (13.24 eV). These two structures appear in the experimental spectrum of Figure 3a, with an asymmetric lineshape and shifted by about 100 meV towards either lower or higher energies in the case of the first and the second peaks, respectively. The experimental results are compared with calculations [5]. The blue line, which represents the calculation without PCI effects, predicts two structures centred at the nominal energies of the photoelectron and Auger peaks. The results of the calculation which includes PCI effects (red line in Figure 2) account very well for the gain/loss in energy of the photoelectron and Auger electron, respectively. The calculation with PCI and without interference effects (dashed line) is superimposed on the full line.

This shows that at this ΔE value the contribution of interference effects is negligible.

The experimental observation is completely different when $\Delta E = -0.5$ eV (Fig. 3b). Here only a feature located between the two expected peaks is observed. Again the experimental observation is well reproduced by the calculation which accounts for PCI. The remarkable increase in intensity in this energy region can be understood as follows. PCI at small mutual angles leads to an energy loss of the Auger electron compensated by an energy gain of the photoelectron. This results in a strong overlap of the two energy distributions in the region between the two original peaks. Then, due to the indistinguishability of the two electrons in this region, strong interference occurs. On the contrary to the back-to-back kinematics ($\vartheta_{12}=180^\circ$), where the interference is destructive, it becomes constructive at small mutual angle. This produces a relatively narrow structure centred at about 13 eV instead of a broad one corresponding only to a shift of both peaks. Such a behaviour was predicted [5], but never observed experimentally.

CONCLUSIONS

In summary, the high resolution and flux achievable at the Gas Phase Beamline and the selectivity of the electron-electron coincidence techniques have enabled us to unravel experimentally the basic effects of coherence and continuum correlation in the double photoionization process. Moreover it is also interesting to note that these coincidence experiments, where the tunability of the incident radiation enables us to tune “coherence/incoherence” effects, are the formal analogue of the quantum optics experiments devoted to the study of mesoscopic superposition of quantum states [6].

REFERENCES

- [1] L. Vegh and J.H. Macek, *Phys. Rev. A* 50, 4031 (1994)
- [2] M. Yu Kuchiev and S. A. Sheinermann, *J. Phys. B* 21, 2027 (1988); *Sov. Phys. Usp.* 32, 569 (1989)
- [3] R.R. Blyth et al. *J. Electron Spectrosc. Relat. Phenom.* 101-103, 959 (1999).
- [4] S.J. Schaphorst et al. *J. Phys. B* 29, 1901 (1996).
- [5] S. A. Sheinerman and V. Schmidt, *J. Phys. B* 30, 1677 (1997); *J. Phys. B* 32, 5205 (1999).
- [6] J.M. Raimond et al. *Phys. Rev. Lett.* 79, 89 (1997); S. Haroche et al. *Phys. Script.* T76, 159 (1998).

X-ray structure of non-covalent calixarene-porphyrin supramolecular complexes with pH tuned stoichiometry

L. Di Costanzo, S. Geremia, L. Randaccio

Centro di Eccellenza di Biocristallografia, Dipartimento di Scienze Chimiche, Università di Trieste, 34127 Trieste, Italy

R. Purrello

Dipartimento di Scienze Chimiche, Università di Catania, 95125 Catania, Italy

“Supramolecular chemistry is the chemical approach to nanotechnology. Many studies have been devoted to the possible application of supramolecular species in fields such as photosynthetic systems, non-linear optical materials, molecular wires or sensors. Porphyrin aggregates have been widely used to obtain sensors, thanks to their peculiar spectroscopic properties. However, well characterized porphyrin assemblies in aqueous solution, are limited to dimeric species. In fact, porphyrin self-aggregation, driven by non-covalent interactions, leads to species with ill-defined stoichiometry. Other molecules, useful to build sensors are calixarenes. Their molecular cavity has been exploited for sensing alkaline or alkaline earth ions and lanthanides. Calixarene-porphyrin conjugates are proposed as a new class of multi-functional sensors. However their structure is difficult to be determined because of the usually poor quality of the single crystals and the large quantity of disordered solvent molecules within the very large channels formed in the crystal. In the present study X-ray structural determinations was made possible (even if at the limits) thanks to the use of synchrotron radiation.”

INTRODUCTION

The rich chemistry of calixarenes and porphyrins, as (polytopic) receptors and photoactive species, respectively and the enormous possibility of functionalising the periphery of these molecules have boosted the synthesis of their covalent conjugates as potential molecular devices [1]. It has recently been shown, for example, that covalent porphyrin-calixarene conjugates behave as molecular tweezers [2]. Formation of non-covalent complexes has been reported but no structural data on such supramolecular species have so far been presented [3.]

Spectroscopic results suggested that the cationic porphyrin (H_2T_4 , Fig. 1) and the *cone* conformation of the anionic sulphonated calixarene bearing carboxylic functions [4] (C_4TsTc , Figure 1), form in aqueous solution supramolecular species whose stoichiometry is tuned by the protonation state of C_4TsTc carboxylates. Particularly, the analysis of the plot of the absorbance of porphyrin vs its molar ratio evidenced a large difference between the complex formation ratio with pH. At pH 2.2 the break point at a porphyrin molar fraction of 0.44 underlines the formation of species in a 4:3 calixarene to porphyrin ratio, whereas at pH 6 the break point at 0.56 of the

porphyrin molar fraction indicates the formation of species with a 4:5 C_4TsTc to H_2T_4 ratio.

We were able to obtain single crystals of the H_2T_4/C_4TsTc complexes, from solutions at pH \approx 2 (**1**) and at pH=6 (**2**), respectively [5] However, both type of crystals deteriorate quickly and gave a very poor diffraction pattern when collected with a conventional X-ray source. Therefore, data were collected at ELETTRA X-ray Diffraction beamline from frozen crystals [6].

RESULTS AND DISCUSSION

In the asymmetric unit of crystals obtained at pH \approx 2 (**1**) [6], the $H_2T_4/(C_4TsTc + H_2T_4)$ molar ratio is 0.43 (two tetranionic C_4TsTc , 1.5 tetracationic H_2T_4 and two sodium ions). Here, the “central” H_2T_4 unit of a trimeric porphyrin ensemble is arranged on a crystallographic symmetry centre (1/4, 1/4, 0) and each of its methylpyridinium moieties is included into a tetra-anionic C_4TsTc molecule from the sulphonate side (Fig. 2). The ditopic nature of C_4TsTc allows also to host one sodium ion on the carboxylate side. The sodium ions are enclosed in an inorganic cage structure formed

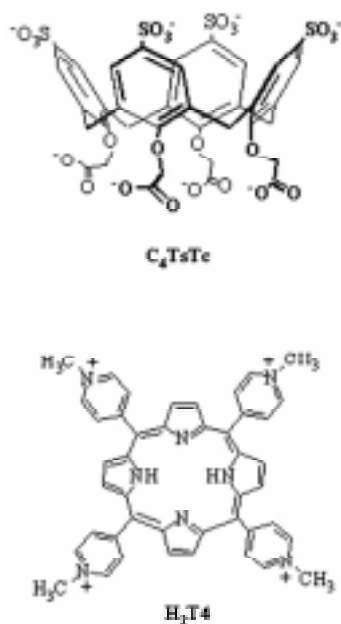


Figure 1. Schematic structure of 5,11,17,23-tetrakisulfonato-25,26,27,28-tetrakis(hydroxycarbonylmethoxy)calix[4]arene (C_4TsTc cone conformation) and meso-tetrakis(*N*-methylpyridinium-4-yl)porphine (H_2T4).

by the hydroxycarbonylmethoxy groups of the C_4TsTc host. The Na^+ ions are co-ordinated by the O atoms of the hydroxy-methylmethoxy residues at distances in the range 2.1–2.6 Å. The centrosymmetric unit of Figure 2 is sandwiched by two porphyrins, rotated by 45° with respect to the central one. The resulting

neutral supramolecular complex is characterised by a distance of 4.2 Å, between the mean planes of the nearly planar porphyrins (Fig. 3). The crystal is built up by these supramolecules in such a way to create large channels (19 × 32 Å), running along the *z* axis. 44% of the unit cell volume is available to solvent. However, only 22% is occupied by disordered pattern of the water molecules crystallographically determined.

Differently from the crystals of **1**, the asymmetric unit of the crystals obtained at pH 6 contains two hepta-anionic calixarenes, three tetra-cationic porphyrins and two sodium ions, with a $H_2T4/(C_4TsTc + H_2T4)$ molar ratio of 0.6, *i. e.* a C_4TsTc/H_2T4 ratio of 4:6. Seemingly, this result disagrees with the 4:5 ratio obtained in solution. Yet, a closer look to the structure of **2** explains readily the difference. In fact, the same trimeric ensemble observed in **1**, still arranged on a crystallographic symmetry centre (1/4, 1/4, 0), is also present in **2** [11]. But now, due to the deprotonation of the carboxylic groups, the synthon trimeric “core” is piled with *two* additional porphyrins, one above and one below, each rotated by 45° with respect to the external H_2T4 molecules of the trimeric core unit, leading to the 4:5 complex of Figure 4. The nearly planar five porphyrins are separated by a distance of 4.5 Å. The sixth tetracationic porphyrin - arranged on the crystallographic twofold axes (0, *y*, 1/4) - is indeed, isolated with respect to the 4:5 core and essentially balances the charge of the tetra-anionic supramolecule. In contrast with the other porphyrins, the electron density map of the isolated one indicates a significant

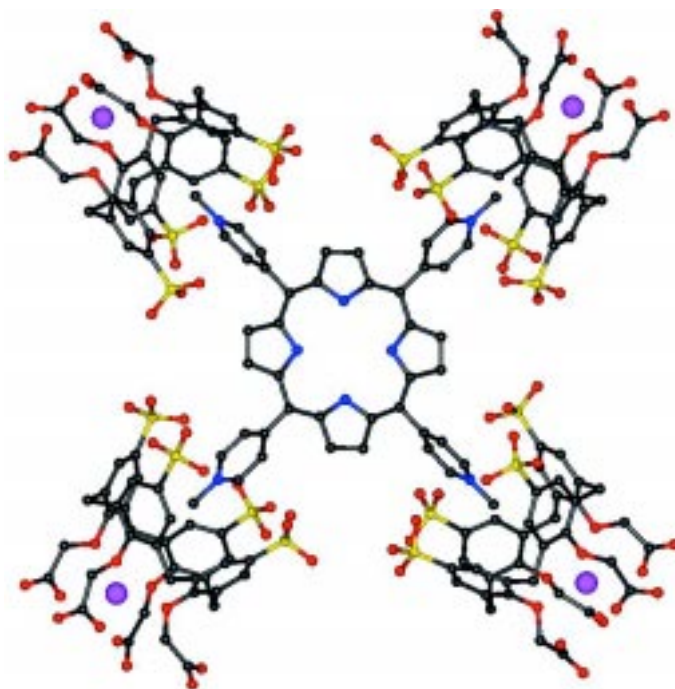


Figure 2. The host-guest interactions in the centrosymmetric unit formed by the central porphyrin tetracation, with calixarene anions and Na^+ ions (violet circles).

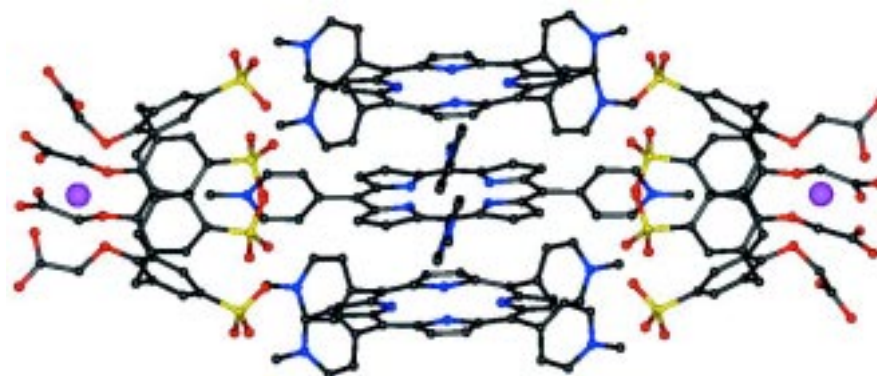


Figure 3. Side view of the neutral supramolecular complex 1. The crystallographic symmetry centre is in the middle point of the central porphyrin. The two calixarene anions hosting the central porphyrin above and below the plane of the figure, have been omitted for sake of clarity.

bent (*umbrella*) conformation. The isolated porphyrins and the supramolecular anion are packed, in such a way to form two series of interconnected channels, one along the x and the other along the z crystallographic axis. The solvent molecules occupy these channels in a disordered manner. The portion of the unit cell, available to solvent is 32% of the cell volume and the crystallographically determined water molecules occupy 20%.

Both complexes are then stabilised by a synergistic network of weak-interactions: i) electrostatic interactions between the positive residues of porphyrins and the anionic sulphonate groups, ii) stacking interactions between porphyrins and iii) CH- π interactions between the $>N^+-CH_3$ groups and the hosting C_4TsTc molecules [10] Quite

intriguingly, the stoichiometry of the species in solid state is preserved in the solution, suggesting that the stoichiometric ratio, spectroscopically determined, coincides with the actual complex stoichiometry. It testifies for a remarkable stability of the complexes.

CONCLUSIONS

In conclusion, the ditopic nature of C_4TsTc turned out to be crucial. The presence of four sulphonated groups and four carboxylate moieties on the upper and lower rim, respectively, allows for i) organisation of cationic porphyrins by shielding their like-charge repulsion and providing various sites (the cavity and the anionic groups) for different kinds of weak-

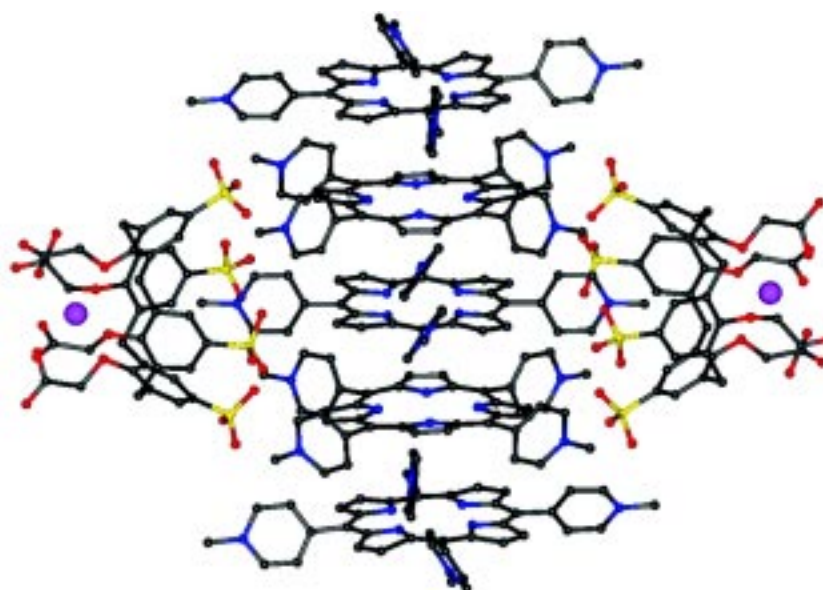


Figure 4. Side view of the the anionic supramolecular complex 2. The crystallographic symmetry centre is in the middle point of the central porphyrin. The two calixarene anions hosting the central porphyrin above and below the plane of the figure, have been omitted for sake of clarity.

interactions, and ii) modulation of the number of complexed cationic porphyrins (by changing with pH the protonation state of the carboxylic groups).¹⁰ The final result is the formation of stable aqueous porphyrin self-aggregates having a well-defined and tunable stoichiometry. This point is relevant considering that, with a few exceptions [11], usually porphyrin self-aggregation in water leads to species having ill-defined stoichiometry.

Further studies are in progress to fully investigate the dependence on pH, ionic strength and the metal inclusion within the porphyrin.

ACKNOWLEDGMENTS

We thank MURST for financial support (PRIN MM003185591)

REFERENCES

- [1] a) R.G. Khoury, L. Jaquinod, K. Aoyagi, M.M. Olmstead, A.J. Fisher, K.M. Smith, *Angewandte Chemie Int. Ed. Eng.* 1997, 36, 2497-2500; b) R. Milbradt, J. Weiss, *Tetrahedron Lett.*, 1995, 36, 2999-3002, c) T. Nagasaki, H. Fujishima, M. Takeuchi, S. Shinkai, *J. Chem. Soc. Chem. Trans. 1*, 1995, 1883-1888, d) D. M. Rudkevich, W. Verboom, D. Reinhoudt, *Tetrahedron Lett.*, 1994, 38, 7131-34.
- [2] T. Arimura, S. Ide, H. Sugihara, J. L. Sessler, *New J. Chem.* 1999, 23, 977-979
- [3] a) F. Gulino, R. Lauceri, R. Purrello, D. Sciotto, Proceedings "4° Congresso di Chimica Supramolecolare", 5-8 Settembre 1999, Catania (Italy), pag. 115; b) K. Lang, P. Kubát, J. Mosinger, V. Král, P. Lhoták, D. M. Wagnerová, Virtual Poster Session (<http://www.photobiology.com/confhall.htm>) IUPAC Symposium on Photochemistry "Photochemistry into the New Century", July 22-27, 2000; c) R. Fiammengo, P. Timmerman, F. de Jong, D. Reinhoudt, *Chem. Commun.* 2000, 2313-2314.
- [4] A. Casnati, Y. Ting, D. Berti, M. Fabi, A. Pochini, R. Ungaro, D. Sciotto, G. G. Lombardo, *Tetrahedron*, 1993, 49, 9815-22.
- [5] The supramolecular complexes were prepared and crystallised by the vapour diffusion method with hanging-drops at 18 °C, under controlled conditions.
- [6] Crystals of 1 and 2 do deteriorate quickly when left in air. However they deteriorate slowly enough to allow the X-ray data collection with synchrotron radiation, when cryoprotected. Data collection performed at the X-ray diffraction beamline at ELETTRA on a 345 MAR image plate with crystals mounted in loop and frozen to 100 K. The structures were solved by direct methods (SHELXS-97) and refined by full-matrix least-squares methods [7] on F² (SHELXL-97). Crystal data for 1: formula C₂₇₆H₁₉₄N₂₄O₉₆S₁₆Na₄ (36 H₂O), Mr=6441, monoclinic space group C2/c; a=48.34 Å, b=35.47 Å, c= 25.59 Å, β=109.03°, V=44720.9 Å³, Z=4, r_{calcd}=0.860 gcm⁻³, F(000)=15264.0, m=0.16 mm⁻¹; 1017 parameters/501 restraints; max./min. residual electron density 0.97/0.26 eÅ⁻³. Total reflections collected 14172 (resolution 1.43 Å), unique 6312 (R_{merge}=10.2). Final R1=0.231 and wR2=0.544, S=4.1 for 5064 observed reflections (I > 2σ(I)). Crystal data for 2: formula C₄₀₈H₃₁₂N₄₈O₉₆S₁₆Na₄ (50 H₂O), Mr=8940, monoclinic space group C2/c, a=52.05 Å, b=30.32 Å, c=36.10 Å, β=114.03°, V= 51985.8 Å³, Z=4, r_{calcd}=1.220 gcm⁻³, F(000)=17676.0, m=0.14 mm⁻¹. Total reflections collected 15404 (resolution 1.03 Å), unique 7684 (R_{merge}=8.0). Final R1=0.285 and wR2=0.640, S=4.0 for 5462 observed reflections (I > 2σ(I)); 1355 parameters/626 restraints; max./min. residual electron density 1.19/0.37 eÅ⁻³. The large values of R1 and wR2 are common for supramolecular complexes having very large unit cells [8] and huge amount of mostly solvent disordered molecules. Several examples of these structures with values of R1 about 0.20 and above have been reported [9]. In addition, the scarce quality of the single crystals and the slow crystallinity loss during the X-ray exposure did not allow collections of good diffraction pattern. Despite the relatively high R values, the crystallographic results are conclusive as to the general shape of the supramolecules and their packing.
- [7] Shelx: G. M. Sheldrick, *SHELXL-93* 1993.
- [8] F. A. Cotton, C. Lin, C. A. Murillo, *Inorg. Chem.*, 2001, 40, 575 and references therein.
- [9] See for example: H. G. M. Edwards, E. Lawson, M. de Matas, L. Shields, P. York, *J. Chem., Perkin Trans. 2*, 1997, 1985; D. Whang, K. Kim, *J. Am. Chem. Soc.*, 1997, 119, 451; S. L. Hendershot, J. C. Jeffery, P. A. Jellis, D. F. Mullica, E. L. Sappenfield, F. G. A. Stone, *Inorg. Chem.*, 1996, 6561.
- [10] R. Purrello, S. Gurrieri, R. Lauceri, *Coord. Chem. Rev.* 1999, 190-192, 683-706.
- [11] C. Endisch, J. H. Fuhrhop, J. Buschmann, P. Luger, U. Siggel, *J. Am. Chem. Soc.*, 1996, 118, 6671-6680.

Carbon nanotubes

A. Goldoni, M. Kiskinova

Sincrotrone Trieste S.C.p.A., s.s. 14 Km 163.5, 34012 Trieste, Italy

Carbon nanotubes are fullerene-related structures, consisting of graphitic sheets wrapped into cylinders [1, 2]. Depending on the number of coaxial cylinders, they are classified as single-wall or multi-wall. In the last decade the interest for carbon nanotubes has grown exponentially, because they have been recognized as an excellent material for nanotechnological applications, where the dimensions of the device components are reduced to nanometer and molecular scales. Single-wall carbon nanotubes, in particular, combine excellent mechanical properties with unique electronic properties, e.g. depending on their helicity (or chirality) and diameter they can behave as metals or semiconductors, with a specific electronic structure at the tips of the nanotubes, where the graphene cylinders can be either closed by hemispherical fullerene caps or open. A

distinct feature is that the electronic structure of the single-wall nanotubes can be easily tuned by distortion, introducing defects and functionalization of the tips and/or sidewalls with foreign atoms [2, 3]. This is placing increasing demands to understanding the detailed spatial electronic structure of these compounds. Photoelectron microscopy is emerging as an excellent experimental tool capable to probe the electronic structure of pure and functionalized nanotubes at the mesoscopic scale. The first experiments performed at ELETTRA with the scanning photoelectron microscope at the ESCA microscopy beamline demonstrate that both valence band and core level spectra are excellent fingerprints, and can be used as a sensitive probe of the local environment, mechanical actions and chemical interactions.

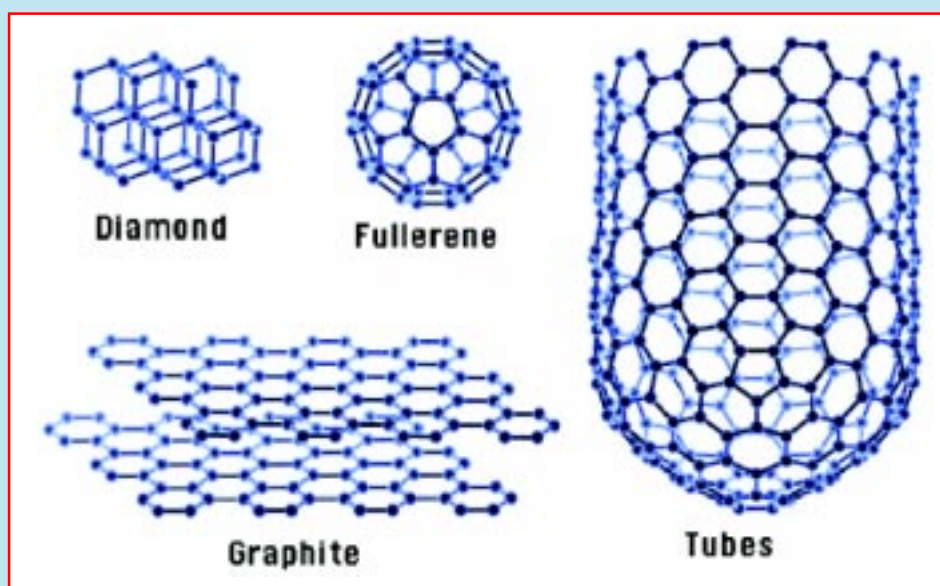


Figure. Allotropic forms of carbon.

REFERENCES

- [1] S. Iijima, *Nature* 354, 56 (1991); S. Iijima, and T. Ichihashi, *Nature* 363, 603 (1993)
- [2] R. Saito, G. Dresselhaus and M.S. Dresselhaus (Eds.), *Physical Properties of Carbon Nanotubes*, Imperial College Press, London (1998) and references therein.
- [3] M.S. Dresselhaus, G. Dresselhaus, Ph. Avouris (Eds.), *Carbon Nanotubes*, *Topics Appl. Phys.* 80 (2001)

X-ray photoelectron microscopy of the C1s core level of free standing single-wall carbon nanotubes

A. Goldoni, L. Gregoratti, B. Kaulich, M. Kiskinova

Sincrotrone Trieste S.C.p.A., s.s. 14 Km 163.5, 34012 Trieste, Italy

R. Larciprete

Sincrotrone Trieste S.C.p.A., s.s. 14 Km 163.5, 34012 Trieste, Italy

ENEA - Divisione Fisica Applicata, Via E. Fermi 45, 00044 Frascati (RM), Italy

L. Sangaletti, F. Parmigiani

INFN - Dipartimento di Matematica e Fisica, Universita' Cattolica del Sacro Cuore, via dei Musei 41, 25121 Brescia, Italy

INTRODUCTION

Here we report a key example of the potential of X-ray core level photoemission microscopy at the 3rd generation synchrotrons, for the investigation of single-wall carbon nanotubes (SWCNTs).

While an intense effort has been directed toward the synthesis of these new carbon materials, and great progress has indeed been made in recent years [1-3], further progress in any device application requires a deep knowledge of the electronic structure, in order to tailor in a controlled manner the properties of SWCNTs. Specifically, the band theory has predicted that SWCNTs can be either metallic or semiconducting, depending on their diameter and chirality [2]. These predictions were verified by scanning tunneling microscopy and spectroscopy [2-4]. Moreover, the electronic properties of SWCNTs, as well as their chemical activity, are predicted to strongly depend on mechanical deformations like stress, torsion, compression or bending [5]. For example, semiconducting SWCNTs can be made metallic, and *vice versa*, by bending the tube. Despite these predictions, there is still a paucity of reliable experimental information regarding the electronic structure of SWCNTs and in particular regarding its dependence on mechanical action or on doping. This is mainly due to the fact that the electron spectroscopies, that have played a crucial role in surface science, solid state physics and chemistry, in order to give reliable information need good crystalline materials, free of unwanted contaminants. Till now, electron spectroscopies have never been applied to SWCNTs materials with these

characteristics [6]. Photoemission spectroscopy, in particular, has been seldom used on nanotube materials. Only few photoemission studies are available and they solely report valence band and core level photoemission experiments on multi-wall nanotubes or on thick films made by disordered tangles of SWCNTs (bucky-papers) of different diameters and chiralities [7, 8]. On these bucky-papers, which were typically affected by a 20% of amorphous carbon material, the performed photoemission experiments probed a very large area (some mm²), superimposing the signals from all kinds of nanotubes and from the amorphous carbon material.

Much more detailed studies on the electronic structure of SWCNTs could be performed if well ordered and clean materials will become available. Remarkably, SWCNTs self-organize into bundles, or ropes, that can be formed by less than a hundred of tubes disposed in a regular lattice [9]. Therefore an isolated bundle of SWCNTs, possibly free-standing, is an ideal candidate for the application of electron spectroscopies in order to obtain reliable information on the electronic structure of these systems. On the other hand, photoemission measurements on free-standing isolated bundles of a few SWCNTs are very difficult since an X-ray microprobe with a suitable photon flux ($>10^8$ photons/s) is required, in order to get a useful signal to noise ratio.

Here we demonstrate, for the first time, that the C 1s core level photoemission spectrum of a free standing bundle of few single-wall carbon nanotubes can be measured thanks to the high-flux of a soft X-ray spectro-microscope, a unique tool to study the electronic structure of such systems.

EXPERIMENTAL METHODS

High quality purified SWCNTs [10], originally produced by laser vaporization of carbon with Ni/Co catalyst (which is known to generate material rich in metallic nanotubes [9]), was first sonically dispersed in toluene, then sonically dispersed in acetone and finally deposited, *via* evaporation of the solvent, on a clean copper grid (2.5 mm diameter), formed by a $15 \times 15 \mu\text{m}^2$ square mesh. The grid was inserted in the ultra-high vacuum experimental chamber of the ESCA microscopy beamline [11] and annealed in UHV at 500 K in order to remove the residual solvent and contaminants from the deposit. All measurements were performed with a photon energy of 750 eV and an overall spectral resolution of 350 meV. Imaging was made by scanning the sample while collecting, within a selected energy window, the photoelectrons emitted from a nanospot (diameter of 100 nm). As reference, a bucky-paper [10] made by SWCNTs of the same quality was also measured.

RESULTS AND DISCUSSION

Figure 1a shows an image of the grid, obtained by measuring the C 1s photoemission signal and scanning a $50 \times 50 \mu\text{m}^2$ area. A similar image was obtained measuring the Cu 3p photoemission signal. Nanotubes tangles have the tendency to form near the corners of the square mesh and on the copper network, while the majority of the holes remain empty. When images are taken scanning a smaller sample area with higher acquisition times, in order to enhance the signal to noise ratio, some new features appear. Figure 1b is a $20 \times 20 \mu\text{m}^2$ image taken around the middle square hole on the right side of Figure 1a. After playing with the cut-off of the color scale and enhancing the contrast (white = minimum signal, red = maximum signal), apart from the tangle of nanotubes visible in the left-high corner as a grey/dark shadowed region, some grey stripes appear in the mesh hole, where apparently there was no material. Their shape is reminiscent of filaments and the width (~ 150 nm) is consistent with the dimension of the beam spot. Considering that the average diameter of our SWCNTs is 1.5 nm, as obtained using Raman spectroscopy [12], these filaments can originate from isolated bundles of SWCNTs. To exclude that these stripes are artifacts and to probe their possible nanotube origin, we have measured in detail the C 1s photoemission signal in different points of the grid (indicated with circles in Figure 1b) and we have compared the measured intensity and lineshape with those measured on the

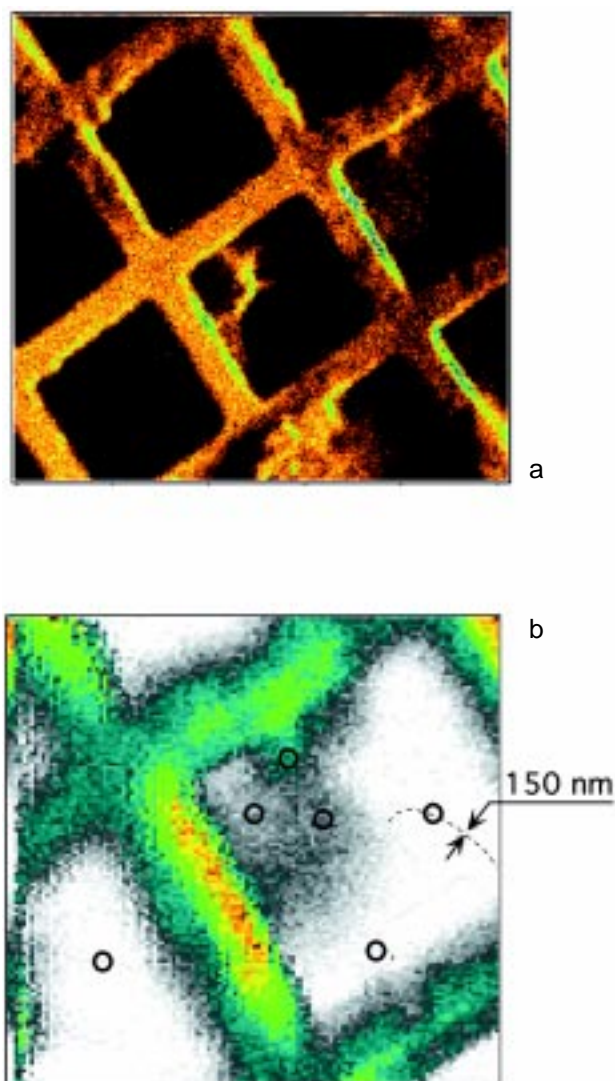


Figure 1. **a)** $50 \times 50 \mu\text{m}^2$ image of SWCNTs deposited on a TEM grid. Note, in particular, the presence of SWCNT tangles inside some mesh holes. **b)** $20 \times 20 \mu\text{m}^2$ image taken around the middle square hole on the right side of (a). Note the presence of filament shaped structures inside the hole - one of them highlighted with a dashed line. The circles indicate points where C 1s photoemission spectra have been measured in detail (Fig. 2).

reference bucky-paper.

The C 1s photoemission signal on the stripe was 15 counts/s, against a dark background signal of 1 ± 1 counts/s. This value must be compared with the photoemission intensity of 3500 counts/s measured onto the dense nanotubes tangle or on the reference bucky-paper. Considering the average diameter of our SWCNTs and the photoelectron escape depth, the C 1s signal measured on the stripes visible inside

the mesh holes is compatible with the presence of an isolated free-standing bundle of less than 15 SWCNTs within the probed microscopic area.

Figure 2 shows the C 1s spectra measured on the reference bucky-paper (top spectra), in correspondence to one stripe inside the holes (points, bottom) and on the SWCNTs tangle (crosses superimposed to the bottom spectrum). The spectra are normalized to the same intensity for the sake of comparison. It is worth noting that, within our energy resolution, the C 1s spectra obtained on the tangle, on the bucky-paper (low binding energy peak) and on the free standing isolated SWCNTs bundle are very similar, supporting the interpretation that the observed stripes originate from SWCNTs. The only notable difference between the two spectra superimposed in Figure 2 is a small bump on the high binding energy side of the C 1s spectrum of the SWCNTs tangle (crosses). This feature may originate from residual solvent or from residual amorphous carbon material trapped in the tangle.

It is also interesting that in different positions on the bucky-paper two C 1s peaks can be clearly detected, characterized by a different binding energy (0.22 eV shift) and a slightly different lineshape. The inset, shows a $6 \times 6 \mu\text{m}^2$ image taken on the bucky-paper tuned to the low binding energy C 1s peak, where the topographic features originating from surface roughness have been removed dividing by the corresponding image tuned on the background signal. The obtained image contrast reflects a concentration contrast (or density contrast), indicating areas where the low binding energy C 1s emission becomes negligibly low (dark/purple areas). Indeed, the C 1s spectrum measured in the dark/purple areas is shifted by 0.22 eV to a higher binding energy, which accounts for the observed concentration scale. The ratio between the red/yellow area (where the high binding energy component dominates) and the dark/purple area (where the low binding energy component is dominant) is about 2.5. The existence of two kinds of carbon signals in the bucky-paper has also been confirmed by conventional (large spot size) high-resolution core level photoemission at the SuperESCA beamline [13], where the two signals have been unambiguously assigned to SWCNTs, excluding possible amorphous or graphitic carbon as signal source.

The presence of both semiconducting and metallic SWCNTs in the bucky-paper can be a possible explanation for the two kinds of C 1s photoemission signal observed. In addition because of the production method of these SWCNTs, the bucky-paper should be enriched in metallic SWCNTs [9]. According to these observations and to the fact that for metallic SWCNTs the core hole is expected to be

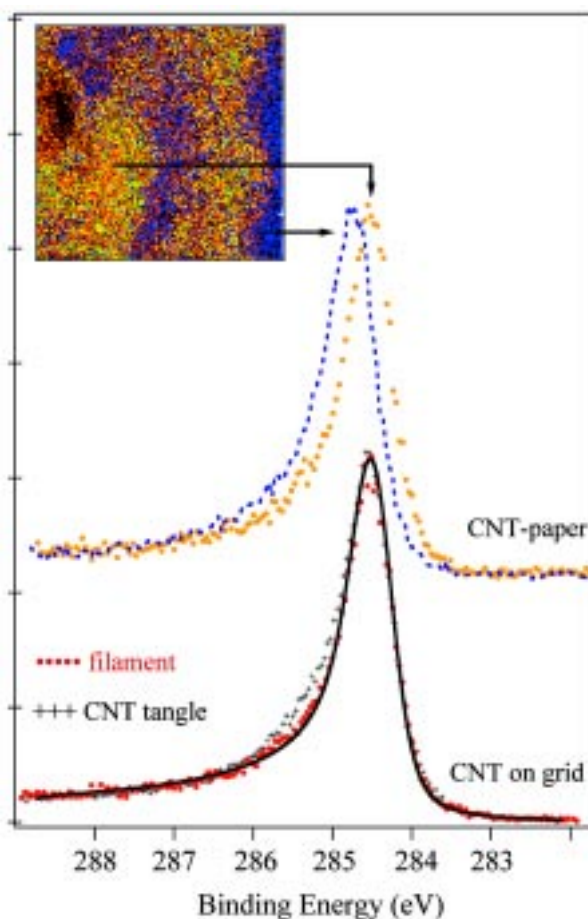


Figure 2. C 1s photoemission spectra measured on the reference bucky-paper (top), on the SWCNT tangle (crosses, bottom) and on the filament-shaped features (points, bottom) visible in Fig. 1b. The fit of the spectrum measured on the filament-shaped features is superimposed as solid line. **inset** $6 \times 6 \mu\text{m}^2$ image taken on the reference bucky-paper collecting electrons in correspondence of the high binding energy peak maximum, where the contrast due to topographic features has been removed. The arrows indicate where the two spectra on top have been measured, showing that the image contrast reflects also a chemical contrast.

better screened, the lower binding energy peak could correspond to metallic nanotubes, while the high binding energy peak to semiconducting tubes.

The lineshape of the C 1s spectrum measured on the free-standing bundle is clearly asymmetric when compared with the symmetric lineshape obtained on an insulating C_{60} single crystal with comparable energy resolution (not shown). The spectrum measured on the bundle shows a typical Doniach-

Sunjic tail [14], reminiscent of the graphite C 1s lineshape, largely because the bundle can be formed by metallic or small gap semiconducting SWCNTs. In Figure 2, superimposed to the spectrum of the free-standing SWCNTs, there is also the best fit obtained using a Doniach-Sunjic function convoluted with a Gaussian function (solid line) that accounts for phonon and experimental broadening. From the fit we obtained a total Gaussian width of 0.45 eV, a Lorentzian width (core hole lifetime) of 0.22 eV and an asymmetry parameter $\alpha=0.19$. The value of the core hole lifetime and the asymmetry parameter are the same as those obtained by high-resolution photoemission [13]. The Lorentzian width is equal to that obtained by fitting the graphite C 1s spectrum, in agreement also with the value reported in literature for graphite [15], and is a typical value for solid carbon, while it is a factor of two larger than for C₆₀ (Lorentzian width 110 meV). This indicates that the C 1s core hole lifetime in SWCNTs and, therefore, the de-excitation processes are more similar to those of a solid rather than to those of molecules. On the other hand, the asymmetry parameter is about twice that of graphite [16], in agreement with the expected higher density of states near the Fermi level in metallic SWCNTs.

CONCLUSIONS

In conclusion, we have successfully performed core level photoemission experiments on a free-standing bundle of SWCNTs. The obtained good signal-to-noise ratio for the C 1s emission provided information on fundamental quantities such as the core-hole lifetime, the binding energy and the photoelectron scattering effects, free from uncontrolled interactions between the nanotubes and the substrate or unwanted contaminants. Besides we have shown that on a bucky-paper, due to the use of a nanoprobe, we are able to distinguish two different photoemission signals related to nanotubes.

The present experimental methodology and results can be considered an onset to further important experiments on carbon nanotubes concerning, in particular, the doping and the interaction between isolated nanotubes and metal or gases under controlled UHV conditions. They also open unique opportunities to probe in-situ the response of the nanotube electronic properties to mechanical actions, since a free-standing tangle of SWCNTs mounted between two nano-tips can be mechanically bended, stretched or compressed while under the photoemission microscope.

REFERENCES

- [1] S. Iijima, *Nature* 354, 56 (1991); S. Iijima, and T. Ichihashi, *Nature* 363, 603 (1993)
- [2] R. Saito, G. Dresselhaus and M.S. Dresselhaus (Eds.), *Physical Properties of Carbon Nanotubes*, Imperial College Press, London (1998) and references therein.
- [3] M.S. Dresselhaus, G. Dresselhaus, Ph. Avouris (Eds.), *Carbon Nanotubes*, Topics Appl. Phys. 80 (2001)
- [4] C. H. Olk and J. P. Heremans, *J. Mater. Res.* 9, 259 (1994); L. C. Venema et al., *Phys. Rev. B* 61, 2991 (2000).
- [5] A. Rochefort, D. R. Salahub and P. Avouris, *Chem. Phys. Lett.* 297, 45 (1998); D. Tekleab et al., *Phys. Rev. B* 64, 035419 (2001); P. G. Collins et al., *Science* 287, 1801 (2000).
- [6] J.H. Fink and P. Lambin, *Topics Appl. Phys.* 80, 247 (2001)
- [7] P. Chen et al., *Phys. Rev. Lett.* 82, 2548 (1999); S. Suzuki, *Appl. Phys. Lett.* 76, 4007 (2000).
- [8] S. Suzuki et al., *Phys. Rev. B* 63, 245418 (2001); S. Suzuki et al., *J. Electron Spect. Related Phenom.* 114-116, 225 (2001).
- [9] A. Thess et al., *Science* 273, 483 (1996).
- [10] www.carbolex.com
- [11] L. Casalis et al, *Rev. Sci. Instrum.* 66, 4870 (1995).
- [12] L. Sangaletti, R. Larciprete, S. Lizzit, F. Parmigiani and A. Goldoni, unpublished.
- [13] S. Lizzit, R. Larciprete, C. Cepek and A. Goldoni, in preparation.
- [14] S. Doniach and M. Sunjic, *J. Phys. C: Solid State Phys.* 3, 285 (1970).
- [15] F. Sette et al., *Phys. Rev. B* 41, 9766 (1990).

Electronic structure of aligned carbon nanotubes studied by photoemission microscopy

S. Suzuki, Y. Watanabe, T. Ogino

NTT Basic Research Laboratories, Atsugi, Kanagawa, 243-0198 Japan

S. Heun, L. Gregoratti, A. Barinov, B. Kaulich, M. Kiskinova

Sincrotrone Trieste, Basovizza, 34012 Trieste, Italy

W. Zhu

Bell Laboratories, Lucent Technologies, Murray Hill, New Jersey 07974 USA

C. Bower, O. Zhou

Department of Physics and Astronomy and Curriculum in Applied and Materials Science, University of North Carolina at Chapel Hill, North Carolina 27599 USA

Photoemission microscopy has been used to investigate the position dependence of the electronic structure of aligned multi-walled carbon nanotubes (MWNTs) grown on Si substrates by microwave plasma-enhanced chemical vapor deposition (MPE-CVD). The study is motivated by the fact that a specific electronic structure is expected at the nanotube tips, where the graphene cylinders are closed by hemispherical caps. Such investigation has

become possible because the high spatial resolution of the ESCA microscope has allowed us to select spots along the axes of the nanotubes and perform systematic measurements of the valence band and C 1s core level spectra; fingerprints for lateral variations in the electronic structure.

All measurements were carried out with the scanning photoemission microscope at the ESCA microscopy beamline with lateral resolution of 90 nm, energy resolution of 0.3 eV, and photon energy of 497.0 eV.

Figure 1 shows a typical cross-sectional C 1s image of a cleaved sample with approximately 10 μm long nanotubes. Since the C 1s emission was practically insensitive to the spatial position, we were able to distinguish the nanotube bundles and select the areas for systematic spectroscopic measurements thanks to the surface topography, caused by inclination and bending of the MWNTs.

The valence band spectra in Figure 2a were measured in spots along the nanotube axis as indicated in Figure 2b. The spectra show that the emission in the energy range down to approximately 1 eV below the Fermi edge is substantially enhanced in the spectra taken in the two different top-tip positions. This is clear evidence that the tips possess a higher density of states in the vicinity of the Fermi level than the sidewalls, which is in fair agreement with the conclusions made on the basis of previous conventional photoemission measurements [1]. The C 1s spectra (not shown) from the tips underwent a reproducible very small shift to lower binding energy by about 50 meV, which might be due to a band

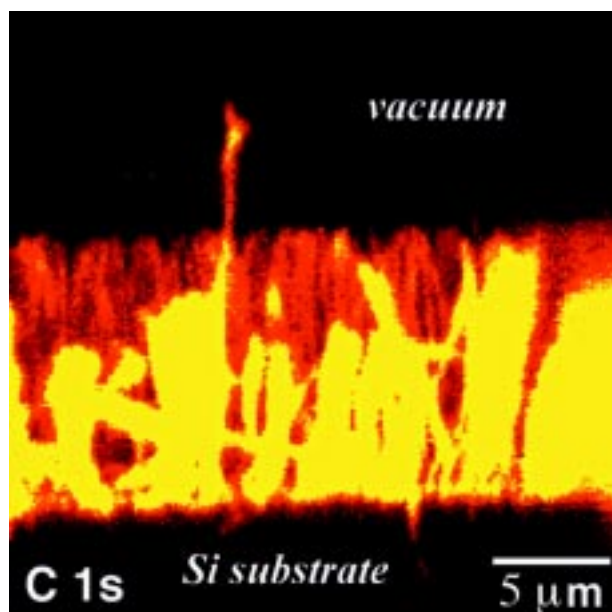


Figure 1. Cross-sectional C 1s image of the aligned multi-walled nanotube sample.

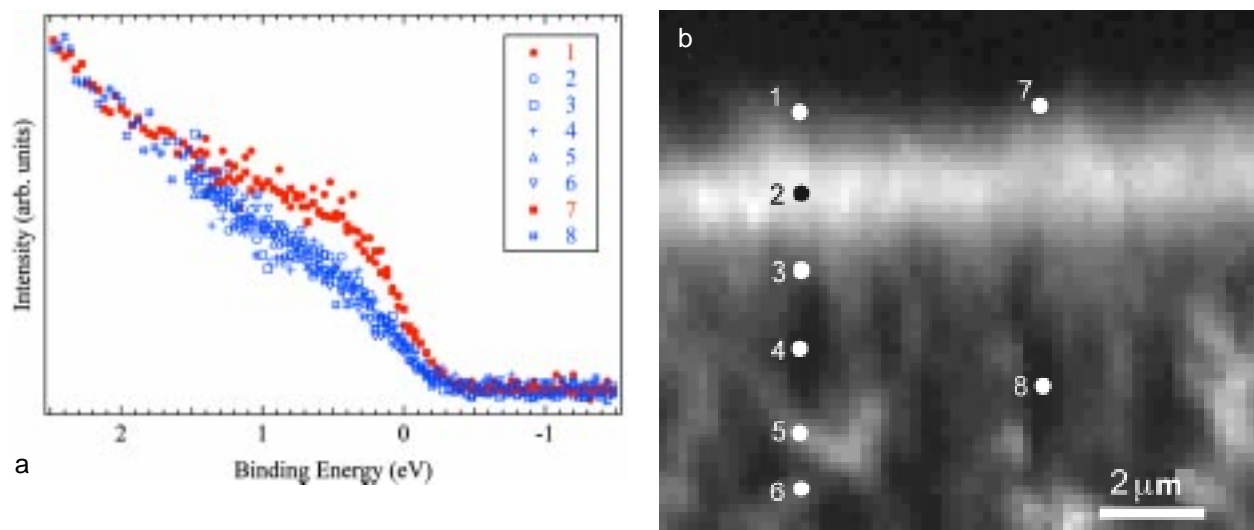


Figure 1. (a) valence band photoemission spectra in the vicinity of the Fermi level from spatially selected regions. The position of the measurements are shown in the C 1s photoelectron spectromicroscopy image in (b).

bending near the tips. This shift is, however, too small to explain the observed large spectral difference between the tips and the sidewalls shown in Figure 2a as due to band bending.

The obtained results can be interpreted assuming a higher density of broken bonds at the tips, considering the defective nature of the MWNTs evidenced by TEM [2]. Thus, the reported difference in the photoemission spectra can be attributed to the strong influence of structural defects on the local

electronic properties of MWNTs, namely the higher dangling bond density at the spherically curved tips than at the cylindrically curved sidewalls. This should naturally lead to an enhanced emission near the Fermi level. The shift of the C 1s core level energy by 50 meV between the tips and the sidewalls can also be considered as a consequence of the different local electronic structures, because localized dangling bond states may cause a slight chemical shift of the C 1s level.

REFERENCES

- [1] S. Suzuki, Y. Watanabe, T. Kiyokura, K. G. Nath, T. Ogino, S. Heun, W. Zhu, C. Bower and O. Zhou, Phys. Rev. B 63, 245418 (2001).
- [2] S. Suzuki and M. Tomita, J. Appl. Phys. 79, 3739 (1996).

A UHV compatible hybrid circuit for multichannel data acquisition systems

S. Carrato

D.E.E.I. - University of Trieste, via Valerio, 10 - 34100 Trieste, Italy

G. Cautero, M. Cautero, C. Fava, D. Giuressi, B. Krastanov, P. Lacovig, R. Sergio, R. Tommasini

ELETTRA Synchrotron Light Laboratory, 34012 Basovizza, Trieste, Italy

The recent availability of third generation synchrotron radiation sources is opening many new opportunities in various fields of experimental sciences.

These opportunities, however, can be exploited only if suitable new acquisition hardware is developed.

A fundamental improvement in acquisition systems is given by the use of parallel readout architectures, which strongly increase the efficiency of detection systems in many kinds of spectroscopic techniques.

As an example, in photoelectron spectroscopy experiments such as ESCA (Electron Spectroscopy for Chemical Analysis), one of the most popular surface science techniques, an electrostatic energy analyser is used to disperse photo-emitted electrons with different kinetic energy [1]. Recently, multichannel readouts have been developed to speed up the acquisition and to exploit the possibilities of fast measurements offered by the third generation synchrotron radiation sources [2, 3].

Unfortunately, the number of channels in these detectors is limited, at the moment, to less than about 100 [2]. This is due to practical limitations related to the interface between the detector, which is under ultra-high vacuum conditions, and the acquisition electronics, which is generally outside the experimental chamber.

In particular, ultra-high vacuum compatible feed-throughs are large and expensive, so that their use is not practical for a number of channels of the order of one hundred or more.

The number of channels could be high enough if the goal is to have a 1D detector, but becomes unacceptable if 2D detection is required.

For all these reasons we have realised a UHV compatible electronic circuit (Fig. 1 and 2) which

embodies two ASIC (Application Specific Integrated Circuit): a preamplification VLSI (Very Large Scale of Integration) component [4] and a mixed analogue/digital VLSI circuit which has been specifically designed to overcome these limitations [5].

The basic idea is to move the whole data acquisition system from outside to inside the acquisition chamber.

In this way data already pre-processed are transmitted outside instead of raw data, thus significantly simplifying the interface between ultra-high vacuum and air.

In particular, the mixed analogue/digital IC is

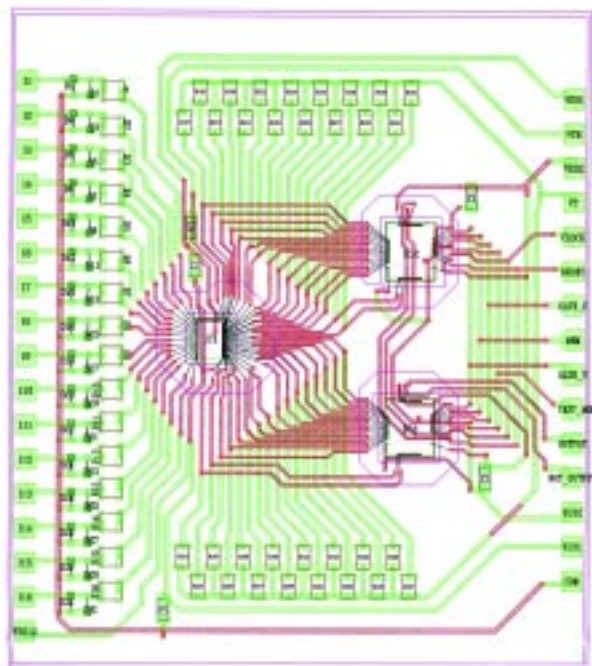


Figure 1. Drawing of the hybrid circuit.

composed of a set of counters, which collect preamplified data coming from the multichannel detector, and some circuitry which is able to transmit the cumulated data onto a fast serial link; consequently, a very simple feed-through can be used, independently on the number of channels.

It is important to notice that the IC, although it will be first used in the ESCA experiment, may be fruitfully exploited in any experiment where parallel readout, two dimensional detection and fast acquisitions are key issues.

The hybrid circuit was long and successfully tested in a UHV chamber where we injected the signal from the outside and counted the pulses coming out from the serial output without any deterioration of the vacuum (10^{-10} mbar).

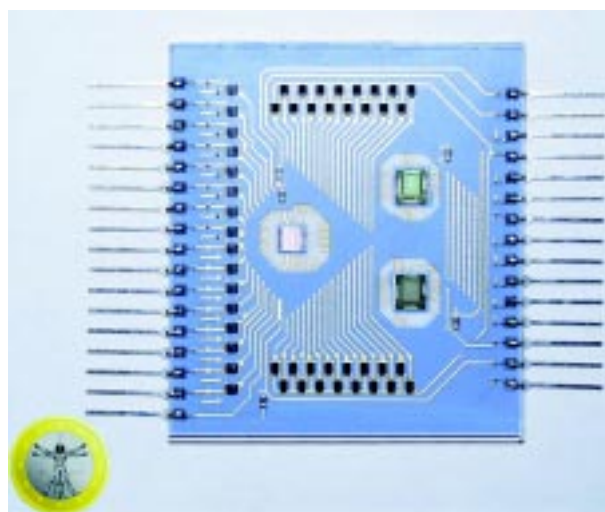


Figure 2. Photograph of the UHV compatible hybrid circuit: on the right side the digital VLSI circuits are visible while the 16 inputs and the preamplification VLSI circuit are visible on the left side.

REFERENCES

- [1] G. Hertl, J. Koppers, Electron Spectroscopy for Surface Analysis, Verlag Chemie, Weinheim, 1974.
- [2] L. Gori, R. Tommasini, G. Caufero, D. Giuressi, M. Barnaba, A. Accardo, S. Carrato, G. Paolucci, Nucl. Instr. and Meth. A 431 (1999) 338
- [3] L. Gregoratti; M. Marsi; G. Caufero; M. Kiskinova; G.R. Morrison; A.W. Potts, Nucl. Instr. and Meth. A 467-468 (2001) 884
- [4] C.C. Enz, F. Krummenacher, R. Bellazzini, Nucl. Instr. and Meth. A 332 (1993) 543

Novel Zone Plate Doublet for Differential Interference Contrast Microscopy Fabricated by means of Electron Beam Lithography

E. Di Fabrizio, B. Kaulich

ESCA microscopy, ELETTRA - Sincrotrone Trieste, S.S.14, km 163.5 in AREA Science Park, I-34017 Basovizza-Trieste, Italy

S. Cabrini

Istituto di Elettronica dello Stato Solido, Via Cineto Romano 42, 00158 Rome, Italy

F. Romanato, T. Wilhein

Rheinahrcampus Remagen, University of Applied Physics, Suedallee 2, D-53424 Remagen, Germany

J. Susini

ID21 X-ray microscopy beamline, ESRF, BP 220, F-34073 Grenoble Cedex, France

TASC-INFN at ELETTRA – Sincrotrone Trieste, S.S.14, km 163.5 in AREA Science Park, I-34017 Basovizza-Trieste, Italy

Electron beam lithography was used to fabricate for the first time a novel X-ray optical element to perform X-ray imaging in differential interference contrast (DIC) with sub- μm optical resolution. With a proper fabrication process it was possible to generate a doublet of zone plates (ZP), on both faces of a 2 μm thick silicon nitrate membrane which were displaced by 100 nm within their optical resolution.

Figure 1 shows the working principle of wave front division.

The use of ZP doublets for visible light interferometry [1], metrology and optical sensing dates back to a few decades ago. The principle of using ZP doublets for interferometry with multi-keV X-rays was described only recently [2, 3]. We demonstrate, similarly to differential imaging in visible light microscopy, a marked increase in image contrast for low absorbing specimen using both a full-field imaging X-ray microscope and a scanning X-ray microscope at a photon energy of 4 keV. Figure 2 reports the comparison between the test pattern image of PMMA resist 2 μm thick as viewed by a single zone plate (bright field) and by the doublet.

This contribution demonstrates the feasibility of X-ray DIC generated by a doublet of two zone plates fabricated by electron beam lithography.

The ZPs are, transversely to the optical axis, displaced of 100 nm, that is, within their optical resolution that is about 200 nm. This means that also the Airy disks of their focal spots are displaced within the optical resolution. Thus, the wavefront division by the ZP doublet can be used for differential imaging

with X-rays intrinsically taking advantage of the high optical resolution reachable with ZPs.

The fabrication process consists of several exposures/depositions of the alignment system and the double side fabricated (doublet) zone plates. The good reproducibility of the fabrication indicates the possibility of fabricating zone plate doublets with resolution around 50 nm. In figure 3 is reported a lithographic image obtained by X-ray lithography that highlights the interferences between the double sided zone plates fabricated on both sides of a silicon nitrate membrane.

The doublet was optically tested at the microscope ID21 at the European Synchrotron Radiation Facility (ESRF) in Grenoble. Figure 4 shows the spatial resolution of about 160 nm on a Siemens star test pattern.

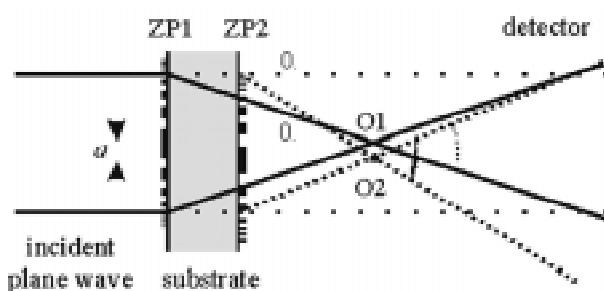


Figure 1. Working principle of wave front division.

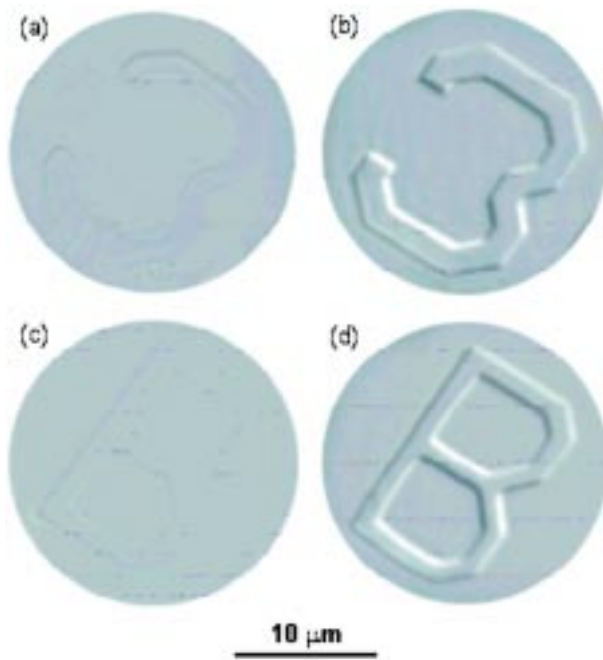


Figure 2. Comparison between the test pattern image of PMMA resist 2 μm thick as viewed by a single zone plate (a, c) and by the doublet (b, d).

We point out the following advantages of using a ZP doublet for X-ray DIC imaging: (1) The alignment of the ZP doublet is fairly simple and similar to that of a single ZP. (2) This DIC technique is usable for both complementary X-ray imaging techniques, i. e. the full-field imaging and the scanning type. (3) The image acquisition does not require data processing and images are visible on-line. (4) The doublet can be fabricated for a wide energy range: from soft to hard X-rays.

In the next future we will extend the energy range application of the doublets and a systematic application to biological samples combined with fluorescence measurements.

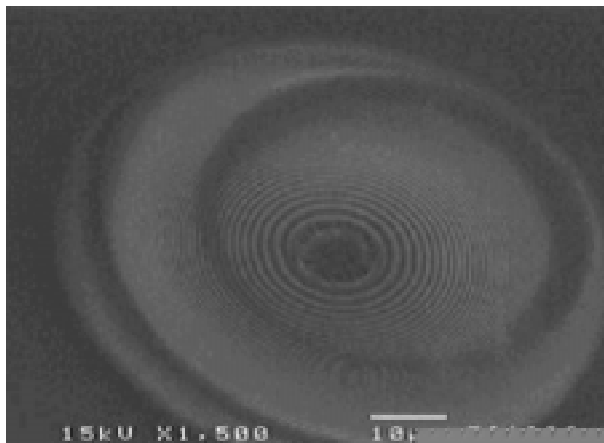


Figure 3. X-ray lithographic image showing the interferences between the ZP fabricated on both sides of a silicon nitride membrane.

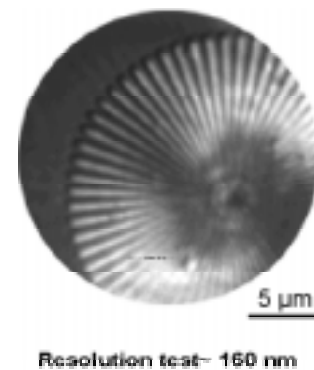


Figure 4. Siemens star test pattern indicating a spatial resolution of about 160 nm.

REFERENCES

- [1] R. F. Stevens, "Zone plate interferometer", *J. Mod. Opt.* 35, 75-79 (1988).
- [2] T. Wilhein, B. Kaulich, and J. Susini, "Common path zone plate interferometry at 4 keV photon energy", submitted to *Opt. Comm.*
- [3] T. Wilhein, B. Kaulich, E. Di Fabrizio, S. Cabrini, F. Romanato, J. Susini "Differential interference contrast x-ray microscopy with sub-micron resolution", *Appl. Phys. Lett.* Vol.78 (2001) n.14, pp. 2082-2084.
- [4] B. Kaulich, T. Wilhein, E. Di Fabrizio, F. Romanato, M. Altissimo, S. Cabrini, B. Fayard, and J. Susini, "Differential interference contrast X-ray microscopy with twin zone plates", *JOSA A*, accepted for publication.

Deep X-Ray Lithography at ELETTRA

F. Pérennès

Sincrotrone Trieste, in AREA Science Park S.S. 14, Km 163,5, 34012 Trieste, Italy

F. De Bona

Universita' di Udine, Via delle Scienze 208, 33100 Udine, Italy

Deep X-ray Lithography (DXRL) allows the production of high aspect ratio three dimensional polymer structures with quasi perfect side-wall verticality and optical quality roughness. These structures can then be used as templates to mass-produce microparts made out of a large variety of metals, alloys or ceramics. It opens a wide variety of potential application in the field of microelectromechanical systems (MEMs), fibre and integrated optics, microfluidic devices and interconnection technology.

A beamline completely dedicated to DXRL was recently commissioned at ELETTRA (Fig. 1). At 2 GeV the critical energy of the radiation produced by a bending magnet at 1.2 T is 3.2 keV and the spectrum extends from 2 to 20 keV after the beryllium

windows. This allows the etching of resist thickness up to a few millimeters. The small divergence induces a maximum lateral shift in the resist wall of 75 nm per millimetre of resist edges.

Microstructures have been produced using two different types of resist, one of positive tone (Polymethylmethacrylate-PMMA) and one negative (Epoxy resin SU-8).

E-beam writer and gold electrodeposition bath facilities are now available to start our in house DXRL mask production in collaboration with the LILIT (Laboratory for Interdisciplinary LITHography). Nickel and copper electrodeposition baths are also in an optimisation phase to produce metallic 3D microparts out off the resist moulds.

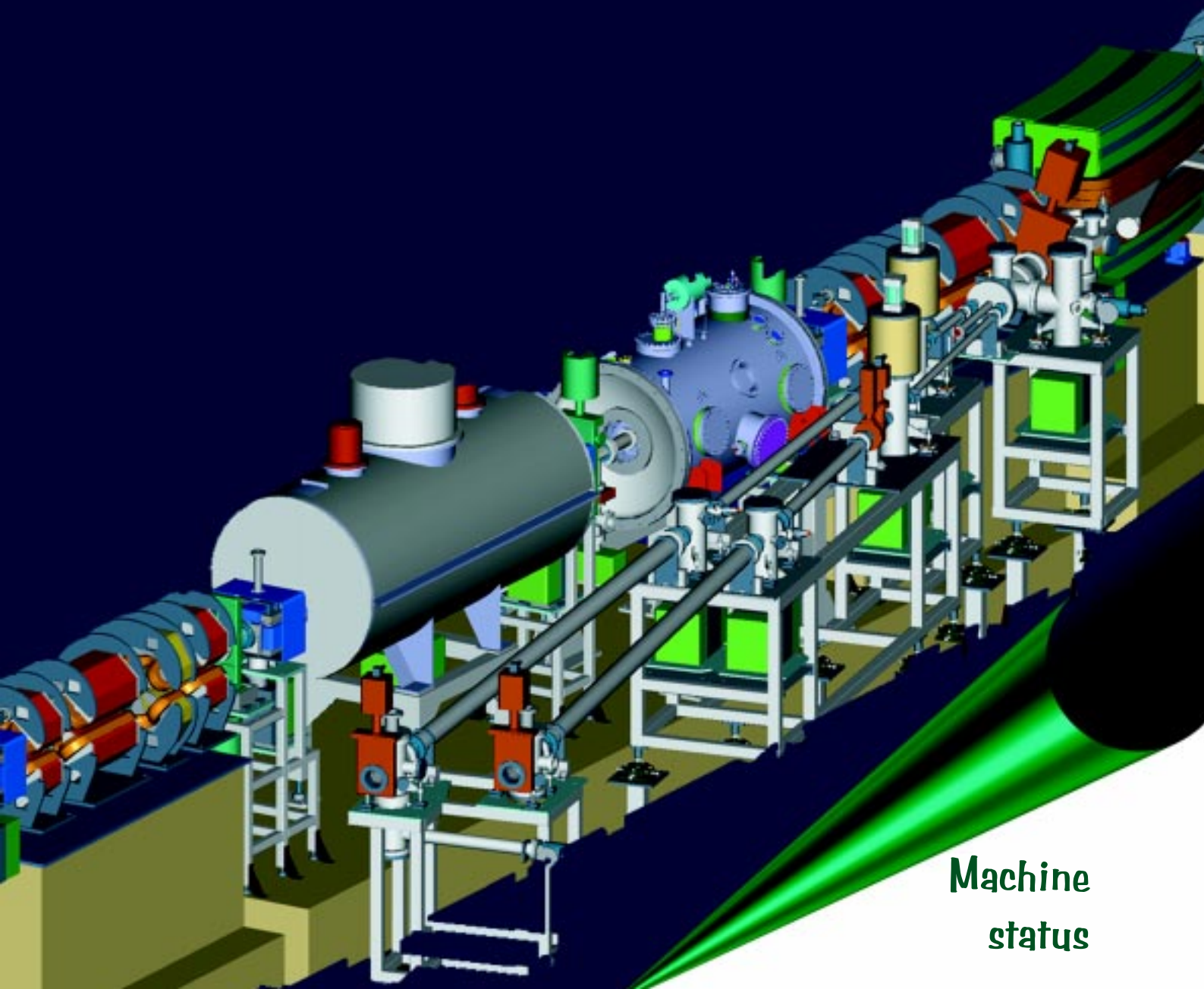


Figure 1. View of the DXRL beamline.



Figure 2. Examples of high aspect ratio PMMA test microstructures produced at ELETTRA.

76 Operational Status and developments
81 The ELETTRA Transverse Multi-Bunch Feedback System
86 Commissioning results of the Low Gap BPM system
90 Progress with the European Storage Ring Free-Electron Laser Project at ELETTRA



Machine
status

Operational Status and developments

C. J. Bocchetta

Sincrotrone Trieste -ELETTRA- S.S. 14 Km.163.5 in AREA Science Park 34012 Basovizza, Trieste, Italy

For both 2000 and 2001 the planned operating time has been close to 6500 hours each year of which more than 5000 hours a year have been allotted to User measurements. During 2000 the light source operated for a total of 6484 hours and 77.5% (5026 hours) of this time was dedicated to the User community and the rest to machine studies, system optimisation and conditioning. The efficiency of systems during 2000 resulted in a User uptime of 91.3% excluding external sources of disturbance such as storms and power-supply interruptions. Including these sources the overall uptime was 89%. The major contributions to the downtime were due to storms and power interruptions (21%), the water system (12%) and the radio frequency (rf) system (9%). The operating schedule for 2001 consists of six runs for a total of 6504 hours of which 5016 are designated to the experimental Users. Part of this time, 25%, is delivered with a beam energy of 2.4 GeV and the remainder at the nominal energy of 2.0 GeV. The User uptime for the first half of 2001 is 95%. As in previous years normal operation for Users involves one injection per day with a starting beam current of 320 mA (8 hours lifetime) that decays to ~100 mA (33 hours lifetime) after roughly 24 hours. Injection is nominally performed at 1.0 GeV, but may also be done at lower energies down to 0.75 GeV. At the higher operating energy (2.4 GeV) the maximum beam current is limited to 140 mA (26 hours lifetime) to contain the thermal load on the vacuum chamber at acceptable values. This current decays to ~70 mA (52 hours lifetime) after 23 hours. The usual mode of operation is multibunch with 90% filling.

The major ongoing developments address improvements to the brightness, stability and lifetime of the photon source. These include new insertion devices, better electron beam position monitors, multi-bunch feedbacks and a third harmonic cavity for bunch lengthening. An upgrade to the rf system is also underway in view of the future increase in the number of installed insertion devices. The multi-phase upgrade involves the replacement of two of the four present 60 kW plants by 180 kW systems. During the first phase an rf cavity will be upgraded and a single plant substituted. The input power to the cavity will be limited to 120 kW and the wasted power in the cavity to 60 kW (~900 kV peak gap voltage) to assure reliable operation. The new cavity will be similar to the ones furnished to the Swiss

Light Source and INDUS-II.

Nine long straight sections are currently filled with insertion devices, including the initial 5 linearly polarized permanent magnet devices: undulators U5.6, U8.0, two U12.5 and the hybrid wiggler W14.0, an elliptical electromagnetic wiggler (EEW) and the most recent series of variably polarized permanent magnet APPLE-II devices. The EEW [1] was designed to produce circular and elliptically polarized radiation in undulator and wiggler modes, with rapidly variable helicity. At present the device is operational in d.c. mode, with user control of horizontal and vertical currents for slow photon energy and polarization changes, and also in a fixed trapezoidal mode at 0.1 Hz, with 0.8 s current ramp and 4.2 s flat-top. A DSP system generates the main current waveform and in synchronism also drives 4 sets of correction coils in a feed-forward mode to maintain residual closed orbit variations at the level of 1-2 μm rms. Future work will extend the operation to higher frequency (up to 100 Hz) in trapezoidal and sinusoidal modes using the same feed-forward correction method but based on correction settings derived from orbit data acquired dynamically using the BPM electronics described below.

The remaining two long straight sections will be filled next year with a superconducting multipole wiggler (SCW) and a Figure-8 undulator. The SCW is designed to produce a high flux and brightness source in the 10-25 keV range for the second Diffraction beamline. The main parameters of the device are given in Table 1. A factor of 3^{14} higher flux will be produced compared to the existing 57-pole 1.6 T wiggler (W14.0) at 12.5 keV (25 keV). A further significant improvement is gained from the smaller source size resulting from the shorter wiggler length (1.4 m instead of 4.5 m) [2]. The detailed design and manufacture of the wiggler is now in progress at the Budker Institute of Nuclear Physics, Novosibirsk. Installation is scheduled for June 2002. The wiggler has a cold-bore design with internal 20 K copper liner to efficiently absorb the thermal load from scattered photons and rf heating.

The future Inelastic Ultra-Violet Scattering (IUVS) beamline requires a high flux of linearly polarized photons in the 5-10 eV range. To overcome the problems of a very high on-axis power density that a conventional undulator would generate with such a low photon energy a Figure-8 structure [3]

has been adopted. The main parameters are listed in Table 2. Such a design [4] achieves a very strong reduction of the on-axis power density: 40 W/mrad² compared to 1700 W/mrad² for a conventional vertical-field undulator with the same fundamental photon energy, period length and number of periods. Similarly the power transmitted by a pinhole of a size sufficient to collect the majority of the fundamental flux (0.6 mrad x 0.6 mrad) at 5 eV is much reduced: 20 W compared to 360 W. The reduction in the flux however is only very small, about 3 %. The permanent magnets have been ordered, the mechanical design has been completed and components will be ordered soon. Installation is foreseen in August 2002.

With the prospect of filling all eleven long ID straights in the near future, attention turned to the possibility of installing short IDs, with a maximum length of about 1 m, in the dispersive regions of the lattice [1]. Such devices can provide about 20 times more flux and 200-300 times more brightness than a bending magnet source. To test the feasibility a prototype device has been constructed using existing magnetic arrays, and a new, simplified, carriage design. The elliptical stainless steel vacuum chamber with an internal (external) vertical dimension of 18 (22) mm, consistent with a minimum undulator gap of 23 mm, was installed in March 2001, followed by the short-ID in June. Initial tests show minimal effects on orbit and tunes. More extensive measurements will be made before the end of 2001 before offering this possibility for future beamlines.

Eight vacuum chambers fabricated from aluminium have been installed in recent years

replacing the usual stainless steel chambers [2]. In the case of the bending magnet (BM) chambers, aluminium was chosen in order to handle the increased thermal load due to the new variably polarized undulators. A fifth chamber will shortly be produced for the figure-8 undulator beamline. A simple aluminium extrusion was also chosen for the new ID vacuum vessels for high mechanical accuracy, higher conductivity and cheapness. Whereas the experience with the new BM vessels was positive, the ID vessels showed a longer conditioning time and higher residual Bremsstrahlung rates. To overcome this problem tests are currently being carried out with NEG coated aluminium chambers. One chamber has been mounted on a test beamline at the ESRF and preliminary outgassing data are encouraging. The mounting of a second chamber in ELETTRA is planned for January 2002.

Transverse coupled-bunch instabilities can be observed at ELETTRA as the beam is ramped in energy and on the stored beam when longitudinal coupled-bunch modes are damped or reduced. A transverse multi-bunch feedback system has been developed in order to allow longitudinal stability to be achieved and make the overall operation of the facility smoother and to improve the quality of the delivered beam also in view of storing higher beam currents. A bunch-by-bunch feedback approach where the positions of each bunch are individually detected and corrected has been chosen [3]. The additional requirements for flexibility and availability of diagnostic tools have led to the development of a digitally based scheme where the position data from the 432 2-ns spaced bunches are

Period length	64 mm
Peak field	3.5 T
Total no. of poles	49
Pole sequence	1/4, -3/4, 1, -1 ... 1, -3/4, 1/4
Internal aperture	81 mm (H) x 10.7 mm (V)
Total power	18.3 kW (2 GeV, 400 mA)

Table 1. Main Superconducting wiggler parameters.

Period length	140 mm
Number of periods	32
Minimum gap	19 mm
B_{y0}, B_{x0} at minimum gap	0.13, 0.72 T
Deflection parameters K_x, K_y	3.4, 9.4
Total power at 2 GeV, 400 mA	2.5 kW

Table 2. Main figure-8 undulator parameters.

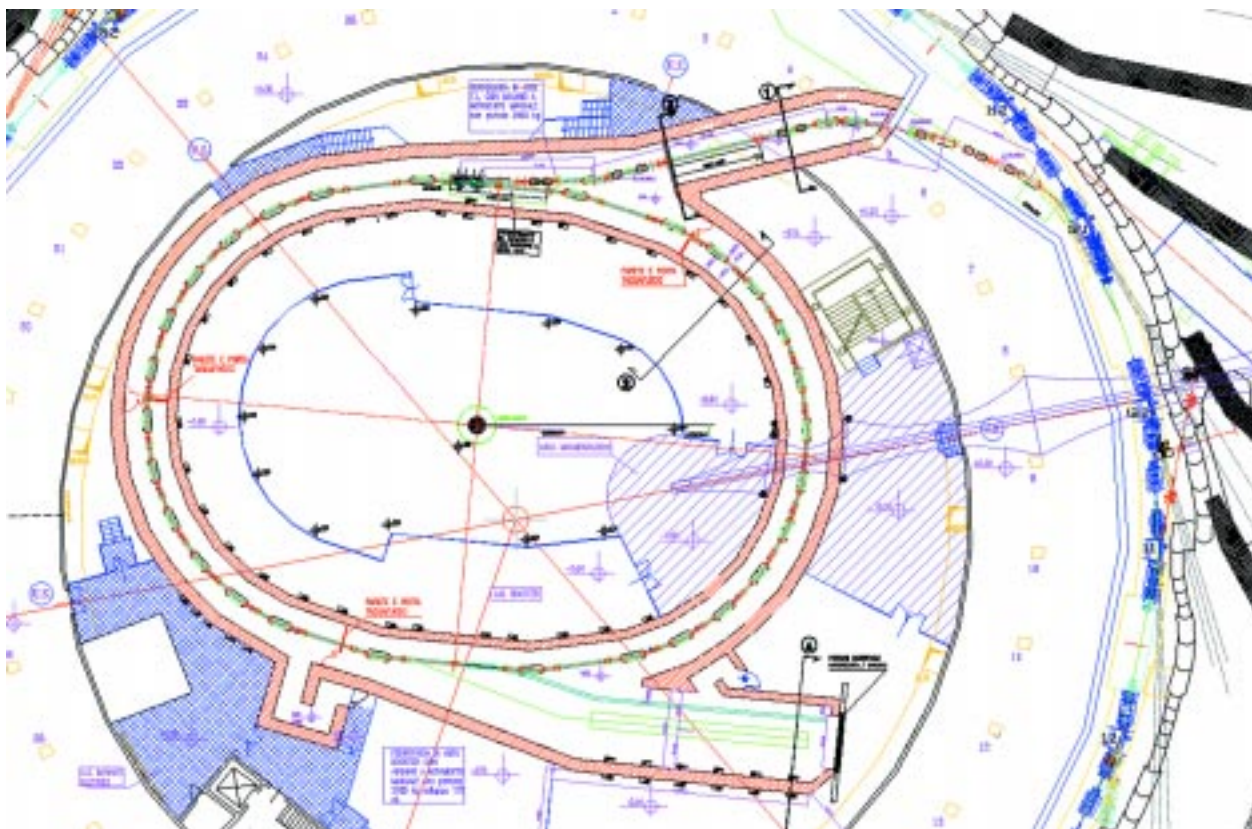
Operational Status and developments

processed by 24 Digital Signal Processors (DSP). The feedback has been installed on the vertical plane, where stronger instabilities have been observed and user requirements are more demanding. The loop has been successfully closed on beams of 320mA at 2 GeV and 130mA at 2.4 GeV, which are the typical target values during operation with users. Further details can be found in these highlights. In addition to the transverse feedback a longitudinal multibunch feedback is also planned. At present longitudinal multibunch instabilities are controlled by temperature tuning the cavities, a procedure that becomes difficult at higher currents [4]. The longitudinal multibunch feedback will take advantage of the already developed digital processing hardware chain, running the appropriate software.

In order to offset the reduction in beam lifetime that will result when the beam is fully stabilised, an idle superconducting 3rd harmonic cavity has been developed and is under construction, in collaboration with CEA-DAPNIA (Saclay, France) and SLS [5]. The cavity, a scaled version of the SOLEIL 350 MHz cavity, will lengthen the electron bunches and is

expected to more than double the overall lifetime. The cavity will operate at 1499 MHz with a nominal accelerating field of 4 MV/m. The first phase of activities was completed at the end of 2000 and involved the design and construction of a copper model that was used to optimise the damping of the higher order modes (HOM's). The final configuration that satisfies the specifications will consist of 6 HOM couplers, of which two are longitudinal mode couplers and four are dipole mode couplers.

The second phase of the project, now under way, concerns the construction of two complete cavities and respective cryomodules. Cavity construction started at CERN in March 2001 and involves the manufacturing process for the copper cavity and connection to the stainless steel Helium tank assembly, Niobium sputtering of the copper cavity bodies and cold tests (4.5 K) in a vertical cryostat. The detailed design and manufacturing drawings of the cryomodule have been completed at CEA-Saclay and orders have been placed for the HOM couplers and output lines, cold tuning system and other components of the module. The planned assembly



Booster Layout

Schematic layout of the booster and pre-injector in the open inner side of the storage ring building. The service gallery for the booster is located on the inside of the booster ring. Access for construction will be from a special crane to be constructed over the storage ring building. This will allow transportation of materials and workmen and the construction of the booster itself to be independent of User operation. Preparatory work for the construction of the booster to storage ring transfer line has already begun.

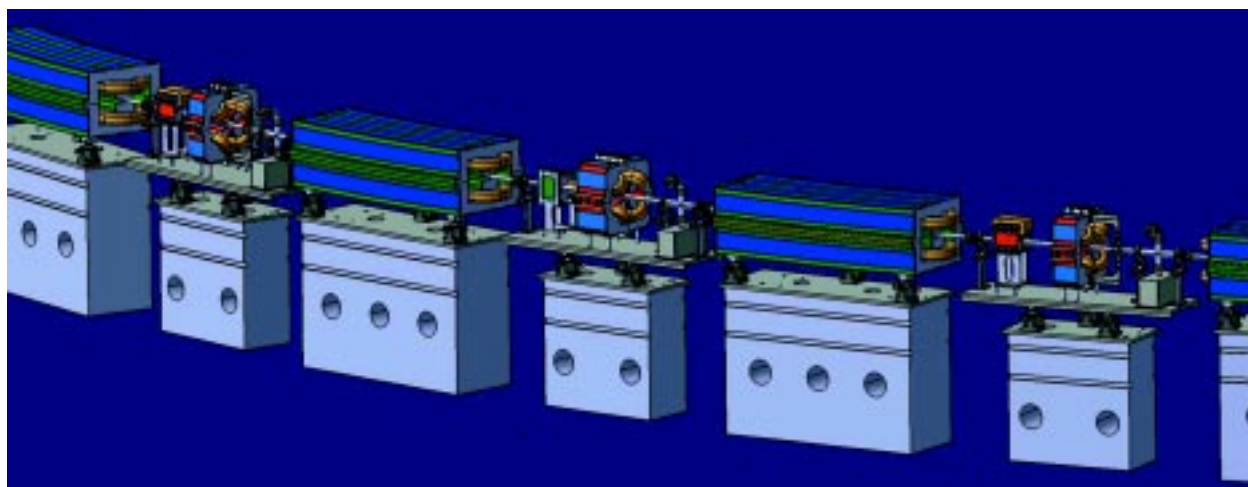
of the modules will be done during the first quarter of 2002 ready for final assembly of the complete system at the start of the third quarter of 2002.

The cryogenic system operating at 4.5 K will be a closed circuit comprising a Helium refrigerator/liquefaction plant operating in a mixed mode. The minimum plant specifications are 45 W of refrigeration power at 4.5 K and 1.3 bar and 5 l/hr liquefaction duty both with 50% margins. An order has recently been placed with AIR LIQUIDE for such a plant (HELIAL 1000). The cryomodule will be installed in a long straight section during an extended shutdown period in 2002. The overall length of the module allows sufficient space in the same section for the installation of the super-conducting wiggler that will have its own independent cooling system.

To provide a stable photon source point is a well-known challenge in third-generation synchrotron light sources. The stabilization over long time periods of the position of the electron beam can be achieved only using high-resolution (at the sub-micron level), high-stability beam position monitoring systems in feedback loops. The low gap Beam Position Monitor (lg-BPM) system [6 and these highlights] has been developed to provide both high resolution and high accuracy beam position measurements. Two main developments have been completed to satisfy the requirements: a new digital programmable detector and a new sensor with its dedicated support system. The digital detector is a completely new four-channel system using parallel processing of the four button signals, to avoid errors due to multiplexing and to improve read out rate. Furthermore, thanks to direct IF signal under-sampling and digital filtering, the receiver bandwidth can be tuned to any of the operation modes: closed orbit, feedback mode or

turn-by-turn. One of the main applications of the lg-BPM system is the use of the position signals for local orbit feedback. A standard PID (Proportional Integral Derivative) controller has been adopted to reduce the low frequency components of the beam noise spectrum, while selective narrow-band filters are dedicated to the suppression of the periodic components, i.e. 50 Hz and its harmonics. The local orbit feedback loop has been successfully closed at a rate of 8kHz on both vertical and horizontal planes and the beam stabilised to well below one micron. The system is currently undergoing long term stability tests and following a successful outcome position sensitive beamlines will be furnished with such systems.

ELETTRA's injector is not full energy, this complicates operation and reduces the overall efficiency. To circumvent this handicap a full energy injector is being designed and developed. The new injector [7] will be based on a 100 MeV linac pre-injector feeding a 2.5 GeV booster synchrotron and will be located on the inner side of the present building that houses the storage ring and experimental hall. Restrictions governed by the available space have led to a compact booster of 118.8 m circumference. The lattice is a FODO structure with 18 cells with missing dipole magnets allowing four long straight sections of near zero dispersion where injection/extraction elements and the rf cavity will be placed. The repetition frequency will be up to 3 Hz, permitting a simple 0.7mm thick stainless steel vacuum chamber and the use of a switched mode power supply. The pre-injector is being built in house. The modulator is currently being assembled and a prototype of the gun is undergoing tests. The main accelerating sections will use two of



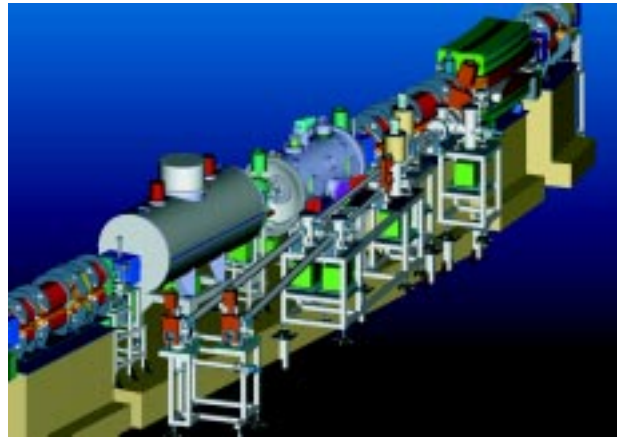
Booster Magnets

The booster magnets, diagnostics, vacuum chamber and pumps will be mounted on concrete blocks. The dipole will have its own support. The quadrupole and BPM, steerer magnet and vacuum system will be positioned on an independent support system.

Operational Status and developments

the recently decommissioned sections of the LIL linac (CERN).

Construction within existing infrastructures and the need to minimise disruption to normal operation calls for careful planning. Operation and shutdown periods during the coming years will be optimised with regard to this especially in view of system integration and putting to operation of the above mentioned developments. Major modifications have already started in the service gallery to make way for the booster to storage ring (BTS) transfer line. The tunnel housing this line will be constructed in the coming year. This year has seen the design and development of major components: magnets, injection/extraction elements, vacuum chamber, rf system, controls and diagnostics. Maximum use of in-house components will be made - including equipment from the existing transfer line and the linac. The chosen rf system will be a five-cell 500 MHz DORIS type cavity (already ordered from ACCEL) powered by one of the present storage ring 60 kW amplifiers that will be available after the rf upgrade. The booster dipole magnets have been designed to operate at 1.3 T and with different coils will be used in the BTS line. The extraction system from the booster will be built similar to the present



Superconducting Equipment in Section Eleven

Schematic layout of straight section 11 showing the two cryomodules for the superconducting wiggler and the idle superconducting third harmonic cavity. The wiggler is placed close to the front end. The two modules will have independent cryogenic systems. A bending magnet Front End is also shown.

storage ring system that also needs to be upgraded to operate at 2.5 GeV. Major orders to industry will be placed during 2002 in view of extracting first beam in 2004.

REFERENCES

- [1] R.P. Walker *et al.*, 'Construction and Testing of an Electromagnetic Elliptical Wiggler for ELETTRA', EPAC, Stockholm, Sweden, 2255, (1998)
- [2] R.P. Walker, Sincrotrone Trieste Internal Report in preparation.
- [3] T. Tanaka, H. Kitamura, Nucl. Instr. and Meth. in Phys. Res. A 364, 368, (1995).
- [4] B. Diviacco *et al.*, 'New Insertion Devices for ELETTRA', PAC, Chicago, USA, (2001).
- [5] L. Tosi and R.P. Walker, 'Study of the Feasibility of Installing Short Insertion Devices in the Dispersive Arcs of ELETTRA', Sincrotrone Trieste Internal Report, ST/SL-01/01 (April 2001).
- [6] A. Gambitta *et al.*, 'Experience with Aluminium Vacuum Chambers at ELETTRA', EPAC, Vienna, Austria, 2292, (2000).
- [7] D. Bulfone, *et al.*, 'First Commissioning Results of the ELETTRA Transverse Multi-Bunch Feedback', Proc. 5th European Workshop on Diagnostics and Beam Instrumentation, ESRF, Grenoble, (2001).
- R. Bressanutti, *et al.*, 'Exploitation of the Integrated Digital Processing and Analysis of the ELETTRA/SLS Transverse Multi-Bunch Feedback System', PAC, Chicago, USA, (2001).
- [8] M. Svandrlík, *et al.*, 'The Cure of Multibunch Instabilities in ELETTRA', PAC, Dallas, USA, 2762, (1995).
- [9] M. Svandrlík, *et al.*, 'The SUPER-3HC Project: An Idle Superconducting Harmonic Cavity for Bunch Length Manipulation', EPAC, Vienna, Austria, 2052, (2000).
- [10] M. Ferianis, *et al.*, 'The New Low Gap BPM System at ELETTRA: Description and Prototype Tests', Beam Instrumentation Workshop, Cambridge, (2000).
- [11] C. J. Bocchetta, 'A Full Energy Injector for ELETTRA', EPAC, Vienna, Austria, 607, (2000).

The ELETTRA Transverse Multi-Bunch Feedback System

C.J. Bocchetta, R. Bressanutti, D. Bulfone, A. Carniel, G. Cautero, A. Fabris, A. Gambitta, D. Giuressi, J. Grgic, G. Loda, M. Lonza, F. Mazzolini, G. Mian, N. Pangos, R. Sergio, V. Smaluk, R. Tommasini, L. Tosi, L. Zambon
Sincrotrone Trieste -ELETTRA- S.S. 14 Km.163.5 in AREA Science Park 34012 Basovizza, Trieste, Italy
M. Dehler
Paul Scherrer Institut, Villigen, Switzerland

INTRODUCTION

The electromagnetic fields associated with the very high intensity electron beams accumulated in state-of-the-art synchrotron light sources can generate Coupled Bunch Instabilities (CBI) through the interaction with the resistivity of the vacuum chamber, cavity-like structures and trapped ions. Multi-bunch instabilities degrade the quality of the beam leading to increased beam emittance, energy spread or even to beam loss. In order to damp any potentially excited transverse mode of oscillation of the accumulated beam, a wide-band bunch-by-bunch Transverse Multi-Bunch Feedback (TMBF) system, where the positions of the 2ns-spaced 432 bunches are independently sampled and corrected, has been developed for ELETTRA.

TRANSVERSE MULTI-BUNCH FEEDBACK SYSTEM OVERVIEW

The block diagram of the TMBF system, for one of the two transverse planes, is shown in Figure 1. The wide-band signals from a single standard four-button Beam Position Monitor (BPM) are combined in a hybrid network producing X and Y signals. These are entered into a RF front-end that demodulates the inputs into base-band (0-250 MHz). Each of the X and Y base-band bunch-by-bunch position signal is sampled by an eight-bit 500 Msample/s Analog-to-Digital Converter (ADC), split and digitally processed. The calculated corrective kick values are symmetrically recombined, transmitted to a complimentary 500 Msample/s Digital-to-Analog Converter (DAC) and amplified by a RF amplifier that powers a single downstream port of a two-stripline kicker. The whole process is synchronized by dedicated timing electronics. A detailed

description of the system can be found in [1] and [2]. In the frame of an effective collaboration, the TMBF kicker has been designed and built by the Swiss Light Source (SLS).

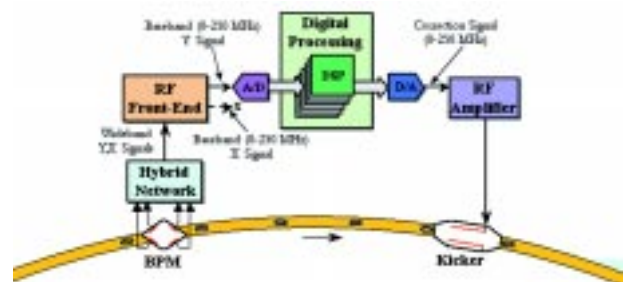


Figure 1. Block diagram of the Transverse Multi-Bunch Feedback System

THE DIGITAL FEEDBACK PROCESSING

In a bunch-by-bunch feedback each bunch is considered as an independent oscillator at the betatron frequency. To add a damping term to such oscillations the correcting kick signal must be shifted by $\pi/2$ betatron phase with respect to the position signal of the same bunch when it passes through the kicker. The basic task of the processing electronics is to calculate the kick values starting from the position signals detected by the BPM. The additional requirements for flexibility and availability of diagnostic tools have led to the choice of a digital scheme based on software programmable Digital Signal Processors (DSP).

The bunch-by-bunch approach splits the required processing power among several DSPs, where each of them is in charge of a given subset of bunches. The 500 Mbyte/s data flux from the ADC, carrying

the position samples of all the 432 bunches, is first de-multiplexed towards six VME based processing boards. The data on each board is then distributed by means of a programmable switch among four available DSPs. Different processing arrangements can be organized. At ELETTRA, the 72 bunch samples arriving at each VME board are passed to the first DSP for on-line acquisition and diagnostics and concurrently split over the three other DSPs that execute the feedback algorithm on the 24 respective bunches.

The correction kick values are basically determined by shifting through a digital filter the phase of the position signal detected by the BPM. As the filter can be programmed to provide any phase, the operation of the feedback is independent of the relative betatron phase between the BPM and the kicker that, because of this, can reside at any position in the ring. The processing should also reject the DC closed-orbit component from the BPM position signal, which is not used by the feedback and would only lead to a waste of output RF power. One of the simplest digital filters satisfying the above requirements is the 3-tap Finite Impulse Response (FIR) one (Fig. 2). It provides DC rejection and the appropriate phase and gain at the betatron frequency. Although the 3-tap FIR filter includes all the essential functionality, other important features can be added when designing a more complex filter. Betatron tune variations move the working point of the digital filter leading to degradation of the feedback performance. The additionally available degrees of freedom of a 5-tap FIR can be used to design a filter featuring the right amplitude and phase in a given limited frequency interval around the nominal tune. Figure 3 is an example of such a filter where fractional tune changes of more than $\pm 20\%$ are possible while keeping the same damping performance.

FEEDBACK OPERATIONAL RESULTS

As a compromise between lifetime and quality, at ELETTRA a beam with controlled longitudinal coupled-bunch instabilities is delivered during standard user shifts by acting on the cavity temperatures. Changing the current temperature values, longitudinal instabilities can be damped or minimized and consequently strong transverse instabilities appear, which require the use of the TMBF. The TMBF has been installed and commissioned in the vertical plane, where stronger instabilities have been observed and user requirements are more demanding. Figure 4 shows the third harmonic of the U5.6 undulator radiation spectrum taken on the SuperESCA beamline in the standard user mode and with damped longitudinal instabilities plus TMBF on (120 mA)

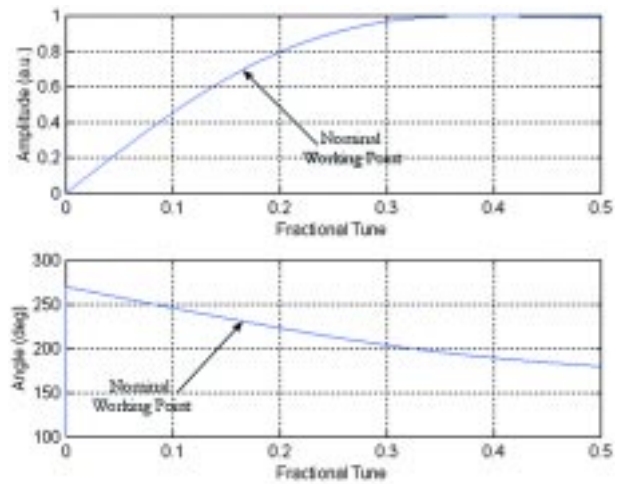


Figure 2. Transfer function of a typical 3-tap FIR filter

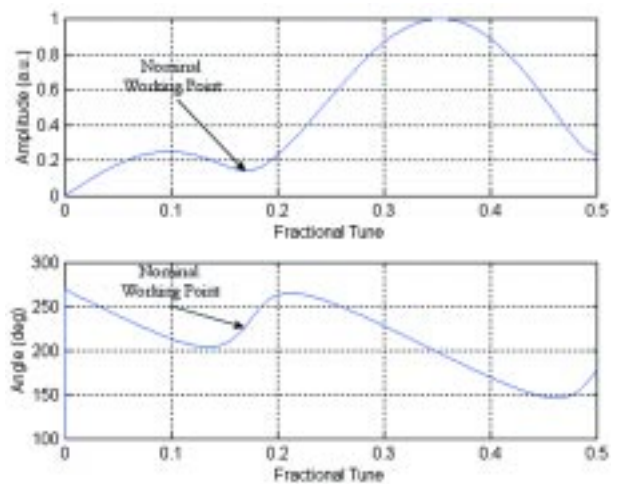


Figure 3. 5-tap FIR filter with compensation of tune variations

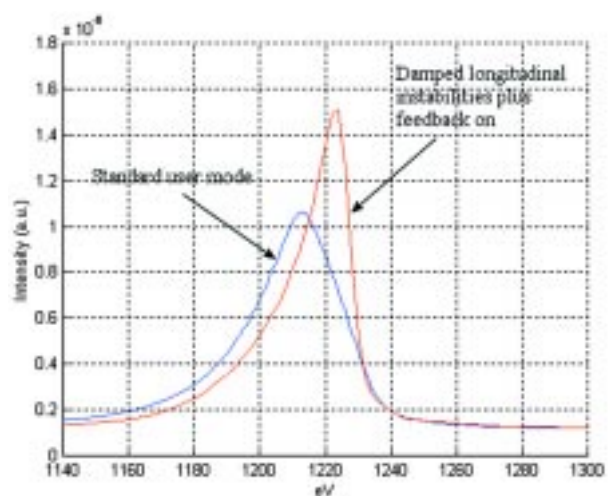


Figure 4. Third harmonic of the ELETTRA U5.6 undulator spectrum (40mm gap) taken on the SuperESCA beamline in the standard user mode and with damped longitudinal instabilities plus TMBF on (120 mA)

standard user mode and in the case of combined damped longitudinal instabilities plus TMBF on. A 5-tap FIR filter of the type discussed before is currently adopted. The feedback loop has been successfully closed on beams of 320mA@2GeV and 130mA@2.4GeV, which are the nominal target values during operation with users.

DIAGNOSTIC TOOLS AND MEASUREMENTS

In addition to the closed loop functionality, the digital implementation of the TMBF allows for an effective integration in the accelerator control system and the implementation of diagnostic features that can be built by appropriate programming of the system.

Filter tap values can be verified/changed on the fly by reading/writing the DSP internal memory through the VME bus, without interfering with the currently executing code. A software driver has been developed that allows setting all of the 432 filter coefficients within 150 μ s. Coefficients can also be changed in time according to a specified sequence of intervals to create controlled growth/damp transients.

A set of data acquisition tools has been developed taking advantage of the six DSPs that are not directly involved in the closed-loop operation. They can run in parallel to the feedback and allow one to acquire an array of bunch-by-bunch position samples of all the bunches during up to 192 ms, corresponding to 96 Mbytes of data.

All of the DSP software features above can be

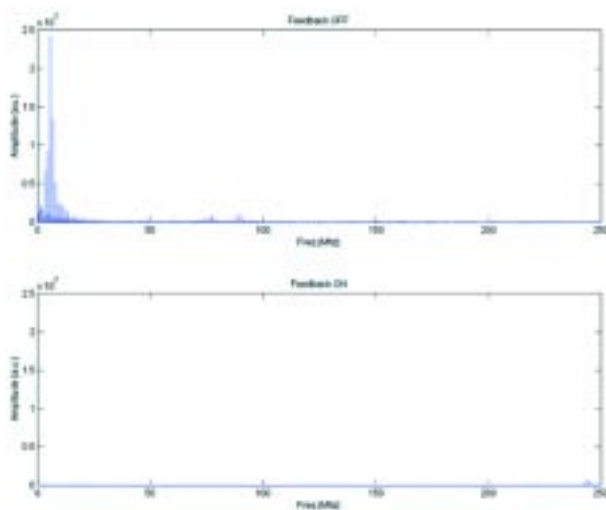


Figure 5. Base-band spectra (with rejected DC closed-orbit component for each bunch) of a 210 mA beam with feedback off/on

accessed through Matlab commands from the control room workstations, providing an integrated environment for TMBF system control, data analysis and graphical visualisation.

The described diagnostics tools are currently used to evaluate the performance of the TMBF and its effect on the beam. The most significant measurements are reported hereafter.

Wide-band Spectra

250MHz-wide spectra for complete multi-bunch mode analysis with 1kHz resolution can be obtained in the control room at a repetition rate of about 0.5 Hz. Figure 5 is an example of such a measurement and shows the base-band (0-250MHz) open/closed loop amplitude spectra of a beam with vertical coupled-bunch instabilities.

Growth/Damp Transients

Growth/damp transients are created by switching the feedback off/on through the proper setting of the digital filter coefficients according to a specified sequence of time intervals. The positions of the bunches during the transients are concurrently recorded by the diagnostic DSPs. Figure 6 shows the spontaneous growth of the oscillation amplitudes of the bunch train for a vertically unstable beam when the feedback is switched off and the subsequent damping effect when the feedback is switched back on. Filter coefficients are set to zero and restored back to their original value after a specified 3.6 ms interval. The bunch train gap can be clearly distinguished. In Figure 7, a transient is analysed in the frequency domain, where the evolution of the unstable vertical modes sidebands of the entire beam spectrum is plotted vs. time. Rise times and damping rates of coupled-bunch modes throughout the whole operating frequency range can be measured by appropriately fitting the acquired data.

Similar transients can also be started with an anti-damping period of positive feedback, which is obtained by inverting the sign of the filter coefficients.

Betatron Tune Measurement and Tune Tracking

Highly resolved betatron tune measurements can be performed using the TMBF system. In the case of a transversally unstable beam, the spectrum of the turn-by-turn position data of a given bunch clearly reveals a line at the fractional betatron tune. Figure 8 is an example of such a spectrum showing also the presence of spurious longitudinal components. Over 222 thousand position samples can be recorded and processed, providing a resolution in frequency of about 5 Hz.

During operation with users, however, the beam

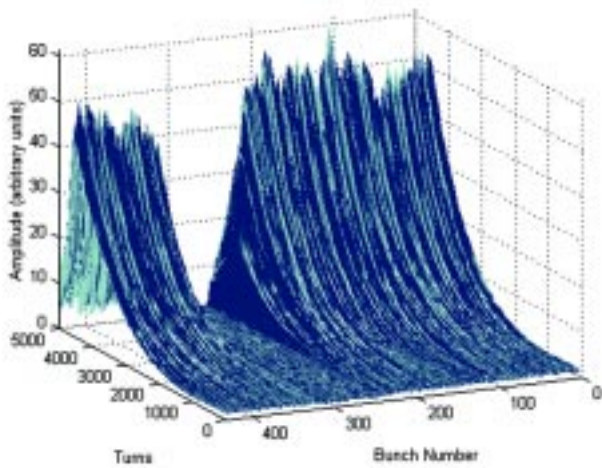


Figure 6. Growth/damp transient of a vertically unstable beam generated by switching the feedback off/on

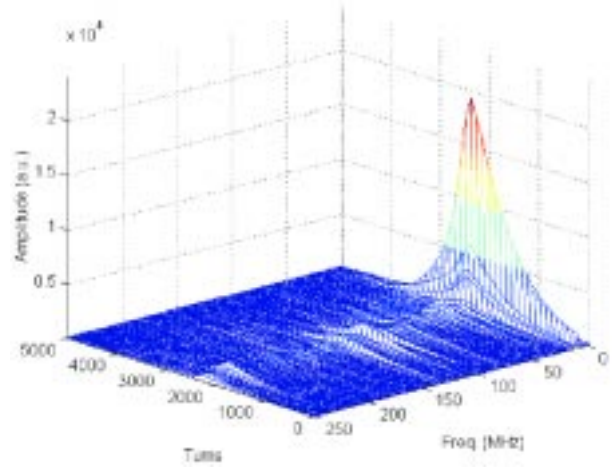


Figure 7. Frequency domain analysis of a growth/damp transient

is kept transversally stable through the action of the TMBF. In this case short growth/damp transients could be created by opening/closing the loop and the tune measured by analyzing the resulting oscillation data. In order to minimize the effect on the stored beam and the disturbance on the users' experimental activities, anti-damping/damping transients are induced on one or few bunches. With the present software configuration, short transients are generated on the subset of 24 bunches that are managed by a specific DSP. This is done by changing the filter coefficients of only the selected DSP. Figure 9 shows the time domain evolution of an anti-damping/damping transient of this type. The 24 bunches are distributed in six smaller groups each having four bunches. The remaining bunches are not affected by the transient and are kept damped by the TMBF system that is concurrently running.

At ELETTRA, considerable tune variations can be observed when opening/closing some insertion devices and during the energy ramping from 0.9 to 2 or 2.4 GeV. In addition to the adoption of a 5-tap filter, as already described, a novel technique called 'tune tracking' has been tested in order to keep the TMBF operation at its optimum working point even in the presence of large betatron tune variations. It consists of periodically measuring the tune by using the method just described, calculating the feedback digital filter coefficients according to the updated tune value and downloading these coefficients into the running DSPs. Positive tests have been performed using a Matlab script that has a repetition period of about one second.

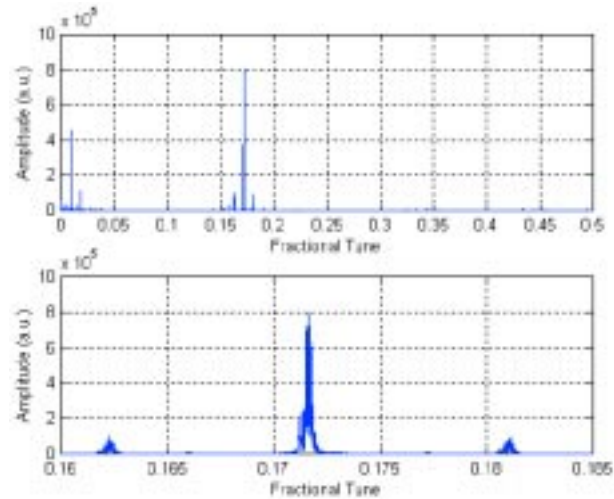


Figure 8. Spectra of the turn-by-turn position signal of a single bunch, with highly resolved betatron tune and spurious longitudinal components

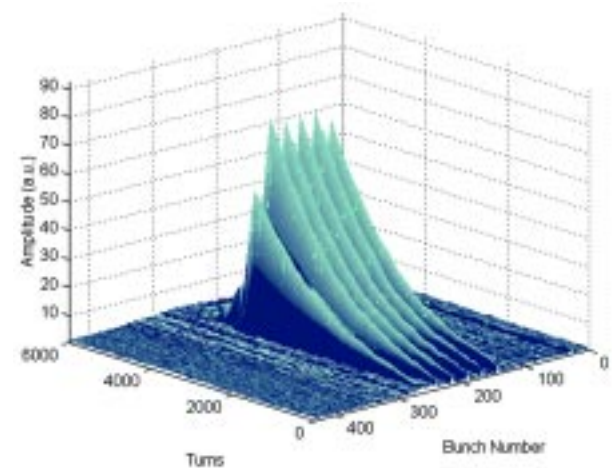


Figure 9. Anti-damping/damping transient created on a subset of 24 bunches

CONCLUSIONS

A bunch-by-bunch TMBF system based on programmable DSPs has been installed on the vertical plane of ELETTRA. Vertical coupled-bunch instabilities have been completely damped on beams with energies/currents corresponding to the standard operational values during user shifts.

Bunch-by-bunch data acquisition and on-line analysis can be performed in parallel to the loop execution. Such diagnostic capabilities are a valuable tool for the understanding of both the TMBF system

and beam physics. A newly developed adaptive technique, called tune tracking, takes full advantage of these integrated features and keeps feedback operation optimized irrespective of machine tune changes.

As part of an existing collaboration, the TMBF system has been successfully installed on the vertical plane of the SLS and is undergoing its commissioning phase. A Longitudinal Multi-Bunch Feedback is also being designed for both the accelerators and will use the already developed digital processing hardware, running the appropriate software.

REFERENCES

- [1] D. Bulfone et al.; *Design Considerations for the ELETTRA Transverse Multi-Bunch Feedback* Proc. PAC'99, New York, March 1999.
- [2] M. Lonza et al.; *Digital Processing Electronics for the ELETTRA Transverse Multi-Bunch Feedback System* Proc. ICALEPCS'99, Trieste, October 1999.

Commissioning results of the Low Gap BPM system

D. Bulfone, R. De Monte, M. Ferianis, G. Gaio, M. Lonza

Sincrotrone Trieste -ELETTRA- S.S. 14 Km.163.5 in AREA Science Park 34012 Basovizza, Trieste, Italy

INTRODUCTION

The “Low Gap” Beam Position Monitor (LG-BPM) system, recently installed at ELETTRA [1], [2] in section 2 has now completed the commissioning phase. The main purpose of the system is to measure the position of the electron beam at the ID centre and monitor its stability at the sub-micrometer level. Two main developments have been completed: the new Digital Detector and the new electron beam position sensor (BPM) with its dedicated support system. Several applications are foreseen for this new BPM system, the most attractive being its adoption in orbit position feedback systems. Measurements, both in laboratory and with a real beam, have confirmed the specifications of the different system components. As a final test a Local Feedback System prototype on section 2 has been successfully operated.

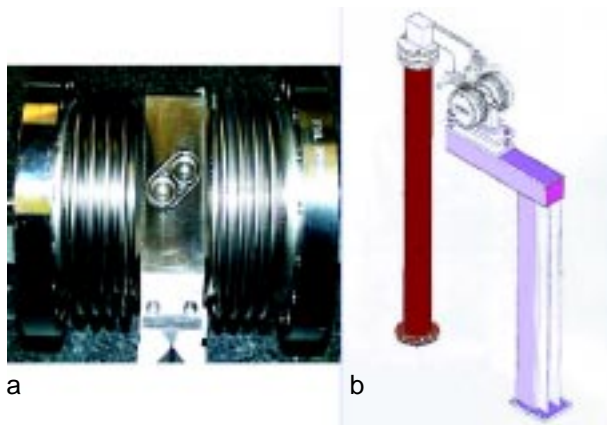


Figure 1a. The Low Gap BPM with the two button electrodes and the two bellows.

Figure 1b. The LG-BPM support system, on the right hand side, with the Reference Column, on the left hand side. A new steel support system for the LG-BPM (Fig. 1b) has been designed. Furthermore, the residual LG-BPM mechanical drifts (few tens of μm) are monitored with respect to a reference column made of carbon fibre and used to compensate the beam position readings.

THE LOW GAP BPM SENSOR

The LG-BPM system has to provide a horizontal and vertical position measurement with sub-micron resolution that is unaffected by long term (24 hours) machine operating condition variations such as beam current. To achieve this resolution and keep costs at a reasonable level a new BPM sensor (figure 1A) has been designed taking full advantage of the 14mm low-gap ID vacuum chamber. Mechanical coupling with the vacuum chamber has been reduced by mounting bellows on either side of the BPM body.

THE LG-BPM POSITION MONITORING SYSTEM

The position monitoring system has to provide real time contact free measurements, to be radiation hard and free from temperature drifts. It is based on capacitive sensors that measure the position and a micro-controller board for front-end acquisition.

The position monitoring system was first tested on a standard BPM showing a resolution of 30nm_{RMS} . Later, the two LG-BPMs installed in section 2 were each equipped with a position monitoring station, measuring the X and Y positions of the LG-BPM together with the temperatures of the LG-BPM and of the machine tunnel. The sub-mm resolution was confirmed on both monitoring stations while fast acquisitions at 1kHz showed no vibrations on the support system. The data from the position monitoring stations are collected through a CAN bus link at a 1Hz rate and delivered to the LG-BPM system CPU (Fig. 2).

DIGITAL DETECTOR: THE ELETTRA SOLUTION

In electronics, the equation “digital equals good performance” is generally agreed. Digital, however, requires a huge programming effort to define the optimum operating point of the device; the great

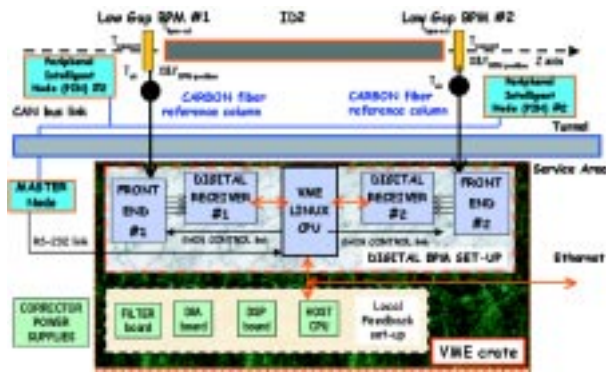


Figure 2. The Block Diagram of the Low Gap BPM system installed in section 2, including the Digital Receivers, the position monitoring system and the Local Feedback boards.

flexibility offered by digital devices calls for appropriate setting of software variables that have direct effect on the hardware behaviour of the device itself. The Digital Detector was jointly developed by the ELETTRA and the Swiss Light Source (SLS) Diagnostic groups [3] [4]. It is a newly developed four-channel system using parallel processing of the four button signals to overcome time-related miss-readings due to multiplexing and to improve acquisition rate.

The Digital Detector system comes as two VME boards: the Analogue Front-End (FE) and the Quad Digital Receiver (QDR). The QDR adopts the direct under-sampling technique [3] of the IF signal that, coupled with the programmability of the output signal bandwidth, allows for any of the operation modes: closed orbit, feedback mode or turn-by-turn [4].

Two pairs of QDR+FE have been installed to

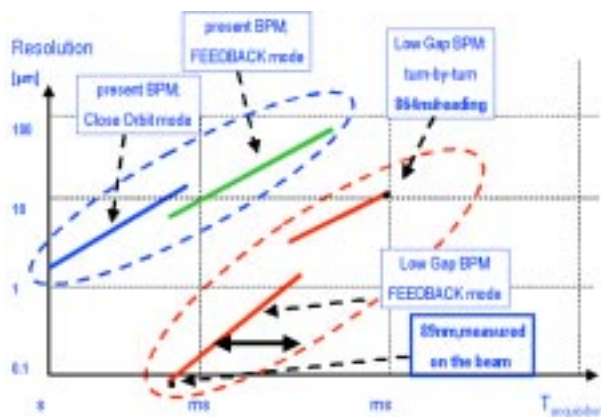


Figure 3. Plot of the resolution (expressed in mm) vs. Acquisition Time (1/reading rate) for various beam position measuring systems: present BPM system at ELETTRA (blu dashed line), Low Gap BPM with Digital Detector (red dashed line).

acquire the signals of the LG-BPM in section 2; the block diagram of the present set-up is shown in Figure 2. The necessary software tasks, including network connectivity are executed under a Linux operating system (RTAI). The core of the system software is a real time kernel module that continuously acquires the data from the VME Digital Receiver boards and performs the X and Y position calculations. The core module is synchronised by interrupts generated by the QDR boards at 4, 8, 16 and 32kHz. The acquired data is stored in a common shared memory area that can be accessed by other non real-time user processes. A number of user processes allow the calculation of average and rms values and the acquisition and management of the mechanical movement data provided by the LG-BPM sensors.

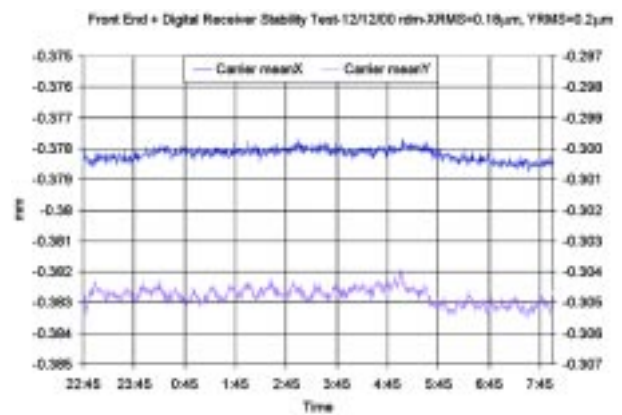


Figure 4. Digital Detector stability measured over 10hours: $X_{RMS}=0.18mm$, $Y_{RMS}=0.2mm$.

MEASUREMENT RESULTS

In beam position monitoring systems resolution has to be associated with reading rate. The graph in Figure 3 shows the two orders of magnitude improvement that has been achieved with this new development. The present BPM system, using the standard romboidal-section BPM sensor and the multiplexed detector, provides 2.5mm resolution at a readout rate of 1sec (including 200 averages). The new Digital Detector provides a resolution of 0.089mm at 62.5ms (including 500 averages). The improvement factor is equal to 16 (2.5/0.089) for the resolution and 25 (1/0.0625) for the read out rate leading to a global factor of 400.

The stability over long periods of time (8-24hours) of the electronics that read the BPM signals is also a major issue. Stability tests are performed using a reference RF generator at fixed amplitude and frequency. Tests performed over a 10 hour period gave the results shown in Figure 4. The RMS values of the vertical and horizontal positions, computed

Commissioning results of the Low Gap BPM system

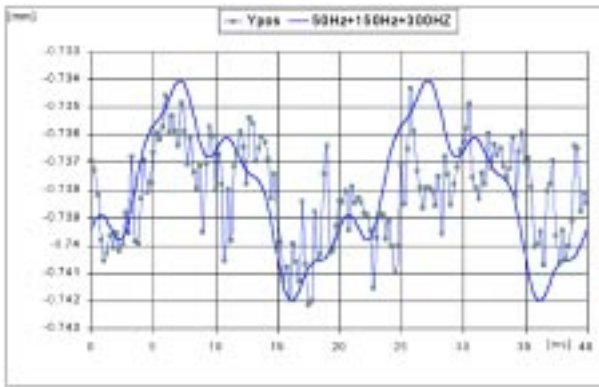


Figure 5. Wide-band (4kHz) beam position data in the vertical plane (red dots) and a first approximation interpolating curve (solid line) obtained by properly (amplitude and phase) summing up the three main spectral components (50, 150 and 300Hz) obtained from the FFT of the same wide-band data set.

using the sensitivity coefficients corresponding to the Low Gap BPM, are less than 0.2mm.

In Figure 5, the wide-band (4kHz) vertical beam motion data are shown (red dots). The solid line of the plot is the first approximation interpolating curve obtained by summing up, with the proper relative amplitude and phase, the three main spectral components obtained from the FFT of the same data set.

THE LOCAL ORBIT FEEDBACK SYSTEM

The LG-BPMs have been integrated in the Local Orbit Feedback System developed some years ago at ELETTRA, which made use of photon BPMs [5]. When operating in the feedback mode, the X and Y data are written by the Linux CPU into the dual-port memory of the local feedback Digital Signal Processor (DSP) VME board. A TI-320C40 DSP clocked at 50 MHz processes the data and implements the control algorithm. A standard PID (Proportional Integral Derivative) controller is adopted to reduce the low frequency components of the beam noise spectrum, while dedicated selective narrow-band filters concurrently suppress the periodic components, i.e. 50 Hz and its harmonics. A D/A converter board transforms the resulting digital output samples into analog signals that drive the corrector magnet power supplies after being low-pass filtered. The feedback uses four magnets per plane to create a local orbit bump that corrects the position and angle of the electron beam at the ID centre, with no distortion of the rest of the orbit. An Ethernet connection provides communication with

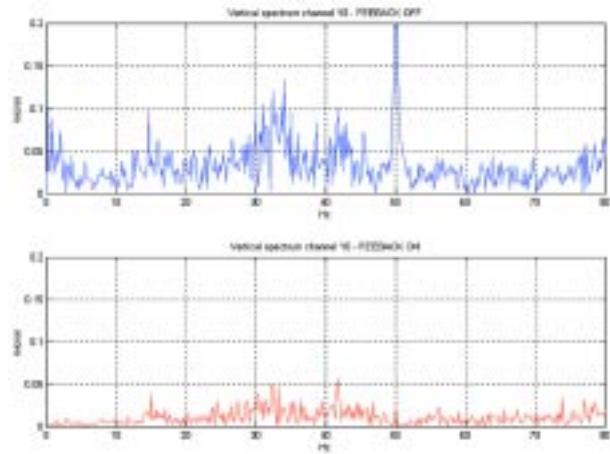


Figure 6. Vertical beam position spectra at the LG-BPM n.1 with local feedback OFF/ON using the PID regulator together with one harmonic suppresser centred at 50 Hz. The rms of the position signal in the 0-80 Hz range is reduced from 1.24 mm to 0.2 mm.

the control system. Operation of the feedback can be remotely controlled from any Matlab session running on control room UNIX workstations. In parallel to feedback processing, the DSP board can store up to 64 seconds of continuous position data at 8kHz that can be uploaded in Matlab for data processing and visualisation.

The local orbit feedback loop has been successfully closed at a rate of 8kHz in both vertical and horizontal planes. The loop corrects slow orbit drifts and low frequency noise components. The position of the beam, measured with the LG-BPMs at a repetition rate of 16 Hz over two hours, shows a rms value of 0.2mm. The spectra in Figure 6 shows the effect of the feedback with the combined action of the PID controller and one harmonic suppresser at 50 Hz.

OPTIMIZATION OF THE EEW FEED FORWARD CORRECTION SYSTEM

A feed forward correction system based on four correction coils is currently used to compensate for the magnetic field integral errors of the Electromagnetic Elliptical Wiggler (EEW) [6]. In view of the operation of the EEW with fast AC waveforms (up to 100 Hz frequency) an optimisation procedure of the feed forward algorithm based on the LG-BPMs has been developed. The readings at high acquisition rate provided by the LG-BPMs give a measurement of the orbit distortion, which is recorded by the DSP system and analysed with Matlab. An algorithm based on a measured response matrix calculates the currents of correction coils that

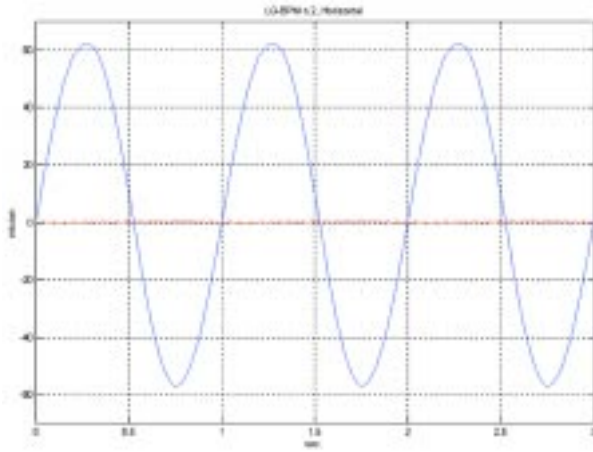


Figure 7. Horizontal orbit at the LG-BPM n.2 without/with the optimized feed forward system based on correction coils. The EEW horizontal coils are operated with a sinusoidal current of 260A amplitude at 1 Hz.

minimise the orbit distortion.

First tests operating the EEW horizontal current with a sinusoidal waveform at 1 Hz give good results. After five iterations of the optimisation procedure

the residual distortion at the LG-BPMs is reduced to the beam noise level as shown in Figure 7.

Further measurements are foreseen to verify the residual distortion using the photon BPMs and operating the EEW with different waveforms and higher frequencies.

ACKNOWLEDGMENTS

The authors thank A. Gambitta and G. Loda for the design of the LG-BPM and its support system; the Vacuum Group for having checked and installed the LG-BPM; N. Pangos, J. Grgic and R. Sauro for the preliminary on-site measurements, quality control and for the dimensional inspection of the LG-BPM. Thanks also go to D. Corso and the workshop for “hardware” assistance.

The thesis studies of prof. A. Boscolo’s (University of Trieste) students, D. Novak and F. Chianese also gave a valuable contribution to the LG-BPM characterisation and to the development of the CAN field network.

REFERENCES

- [1] M. Ferianis et al. “The New Low Gap BPM System at ELETTRA: Description and Prototype Tests”, BIW’00, Cambridge, May 2000.
- [2] M. Ferianis et al. “The Low Gap BPM system at ELETTRA: commissioning results” DIPAC 2001, ESRF Grenoble.
- [3] Dehler, M. et al. “New Digital BPM System for the Swiss Light Source”, in DIPAC’99 Proceedings, *pg.158-160*.
- [4] M. Dehler et al.,”Digital BPM System for the Swiss Light Source- First operational Results”, BIW’00, Cambridge, May 2000
- [5] M. Lonza et al., “The ELETTRA Fast Digital Local Orbit Feedback”, ICALEPCS’97, Beijing China, November 1997
- [6] M. Lonza et al., “Controls for the Electromagnetic Elliptical Wiggler at ELETTRA”, ICALEPCS’99, Trieste Italy, October 1999.

Progress with the European Storage Ring Free-Electron Laser Project at ELETTRA

M.Marsi, M. Trovò, R.P. Walker

Sincrotrone Trieste

J.A. Clarke, M.W. Poole

CLRC Daresbury Laboratory, Warrington, UK

M.E. Couprie, D. Garzella

CEA/SPAM and LURE, Orsay, France

G. Dattoli, L. Giannessi

ENEA, Frascati, Italy

A. Gatto, N. Kaiser

Fraunhofer Institut für Angewandte Optik und Feinmechanik, Jena, Germany

S. Günster, D. Ristau

Laser Zentrum Hannover, Germany

INTRODUCTION

Free-Electron Lasers (FELs) represent the next generation of accelerator based light sources, capable in principle of operating at any wavelength from the far infrared to the X-ray region. In the most common FEL configuration, the oscillator, the light produced by an electron beam travelling through an undulator is stored in an optical cavity composed of two high reflectivity mirrors, and laser amplification occurs starting from this stored emission. Although the ambitious goal of reaching the hard X-ray region rests on the successful evolution of other kinds of FEL not employing mirrors, such as Self Amplified Spontaneous Emission (SASE), nevertheless, in the regions where high quality mirrors are available FEL oscillators represent excellent light sources for scientific research, because of their spectral purity, temporal stability and coherence (both spatial and temporal). In the infrared region they have already evolved to become real user facilities, based on linear accelerators. In the UV/VUV they are under development both at ELETTRA and on other storage rings such as SuperACO (France), UVSOR and NIJI-IV (Japan), and Duke University (USA).

The first storage ring FEL project to be based on a “third generation” synchrotron radiation user facility began at ELETTRA in May 1998 as a European collaboration, with partial funding from the European Commission under a RTD contract [1]. First lasing was achieved in February 2000 at a

wavelength of 350 nm, and later in May at 220 nm [2], as described in last year’s “ELETTRA Highlights”. Since then further significant progress has been made in a number of areas as described below.

LATEST RESULTS

The most important result obtained this year was in February 2001 when lasing was achieved at slightly less than 190 nm using specially developed oxide multilayer coated mirrors [3,4]. The wavelength was tuneable (by undulator gap variation) over the range 189.7-200.3 nm. Figure 1 shows the measured spectrum at close to the shortest wavelength obtained, representing the current shortest wavelength reached by any FEL oscillator. Figure 2 shows the temporal profile of the FEL radiation pulses. Lasing below 200 nm was been obtained on 3 successive FEL runs with the same mirrors. A maximum output power of 16 mW was measured at 31 mA beam current at 195 nm, in line with expectations.

Most of the mirror types that have been employed so far have been optimised for maximum reflectivity and low transmission (T), so limiting the power output to the range of a few tens of mW. In order to explore the possibilities for increasing the power, special mirrors were fabricated in the 250 nm region with higher transmission. Together with a low

transmission back mirror, studies were carried out with a medium transmission ($T_2 = 1.3\%$) and a high transmission ($T_2 = 5.2\%$) front mirror. In July 2001 a maximum of 330 mW was recorded with 36 mA beam current with the high transmission mirror. Figure 3 shows the power as a function of wavelength for both mirror types. The useful width is of the order 32 nm (24 nm) with the medium (high) transmission mirrors respectively.

Initial attempts to use the FEL radiation for experiments have concentrated on performing photoemission electron microscopy (PEEM) close to the photothreshold. Lateral contrast due to work function variations was observed on Pb islands grown *in situ* on a W (110) surface within a $5\ \mu\text{m} \times 5\ \mu\text{m}$ observation area [5]. Given this encouraging result work will continue on such systems in the future. Another important aspect for the future of the FEL activity is the compatibility of the FEL operation with the operation of other beamlines interested in exploiting the 4-bunch mode of ring operation for carrying out time-resolved measurements. On several occasions it has been verified that the Gas Phase beamline undulator can be closed to minimum gap and used in parallel with FEL operation without any difficulty. Most recently the FEL has also been operated at higher ring energy, 1.3 GeV, which could be important in the future for a combined FEL/ Timing mode of operation.

CONCLUSION AND FUTURE PLANS

The initial phase of development of the European FEL at ELETTRA has been successfully concluded. The main present characteristics of the FEL radiation can be summarised as follows:

Wavelength	190 – 350 nm
Max. power	330 mW
Max. photon flux	$4.2 \cdot 10^{17}$ photons/s/
Relative spectral bandwidth	$2 - 4 \cdot 10^{-4}$
Pulse duration	8 - 10 ps
Pulse repetition rate	4.6 MHz

The further improvements of the source and related experimental equipment which are necessary in order to allow the FEL to become a user facility will be carried out under a second EC contract due to start in the near future. In order to enhance the scientific potential of the source an important future objective is to pursue shorter wavelengths, the aim being firstly 180 nm and eventually 155 nm. Another objective is to improve the FEL temporal stability, both to permit two-colour (“pump-probe”) experiments, as well as for the benefit of single beam experiments. The third goal is to develop instrumentation to allow a range of different types of experiment to be performed and carry out a set of initial experiments using the FEL only (particularly

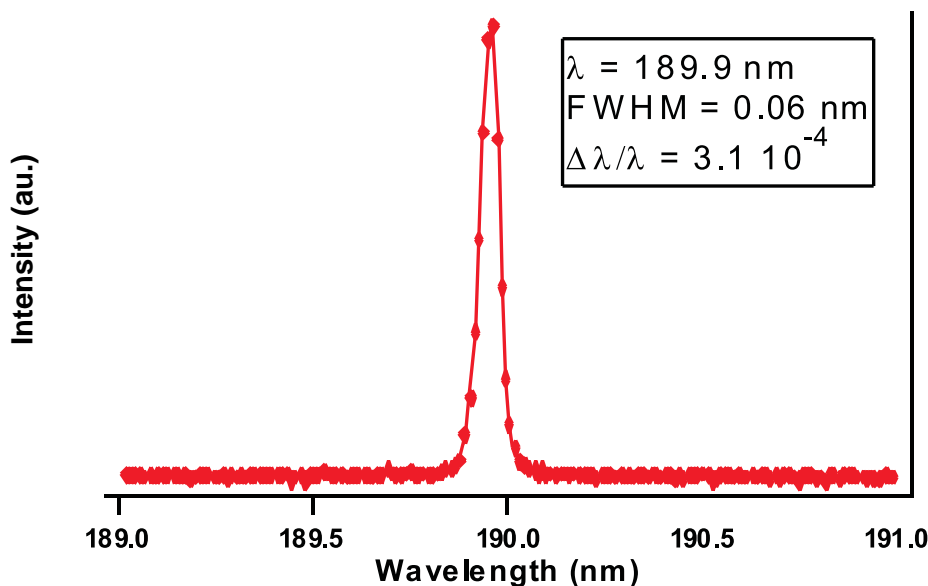


Figure 1. Measured FEL spectrum at 189.9 nm – currently the world record for the shortest wavelength of a FEL oscillator.

Figure 2. Measured FEL pulse shape at 190 nm.

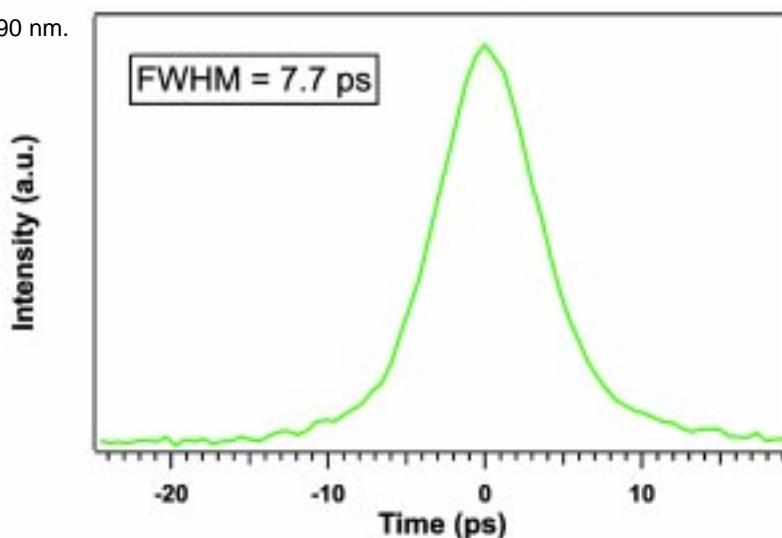
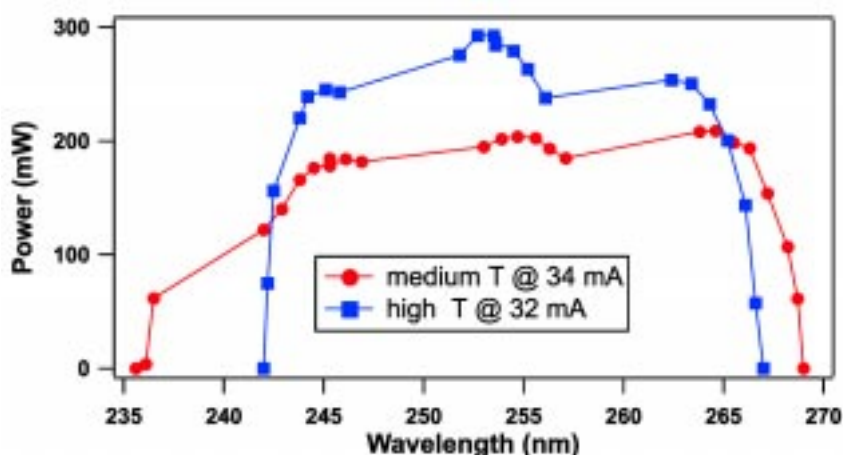


Figure 3. Measured output power as a function of wavelength with medium and high transmission mirrors.



those techniques that require the high photon flux of the FEL - spectroscopic PEEM, time resolved spectroscopy of magnetic systems, energy and spin resolved photoemission of clusters) as well as pump-probe experiments to study excited states in molecules.

ACKNOWLEDGEMENTS

It is a pleasure to thank our colleagues from Sincrotrone Trieste for their continued support: D. Cocco, D. Corso, B. Diviacco, A. Fabris, M. Ferianis,

F. Iazzourene, E. Karantzoulis, C. Pasotti, M. Pasqualetto, G. Sostero, M. Svandrlík, L. Tosi and D. Zangrando as well as N. Bliss, R. Marl, I.D. Mullacrane and R.J. Reid (Daresbury Laboratory) for assistance with the mirror chambers, and R. Bartolini (ENEA) for participation in FEL shifts. The support of previous EC contract participants D. Nölle, K. Wille (University of Dortmund), M. Eriksson and S. Werin (MAX-lab) is also gratefully acknowledged.

A. Gatto is supported by EC TMR Network Contract ERBFMRX-C980245.

REFERENCES

- [1] R.P. Walker et al., Nucl. Instr. Meth. Phys. Res. A429 (1999) 179.
- [2] R.P. Walker et al., Proc. 22nd Int. FEL Conference, Durham, NC, USA, Aug. 2000, to be published in Nucl. Instr. Meth. Phys. Res.
- [3] M. Marsi et al., Synchrotron Radiation News, Vol. 14, No. 4, 2001 p. 19.
- [4] M. Trovò et al., Proc. 23rd Int. FEL Conference, Darmstadt, Germany, Aug. 2001, accepted for publication in Nucl. Instr. Meth. Phys. Res.
- [5] M. Marsi et al., Proc. VUV-XIII, Trieste, July 2001, accepted for publication in Surf. Rev. Letters.

94 ELETTRA Beamline Status
95 ELETTRA Layout
96 Statistics of accepted proposals
98 Resources allocated at ELETTRA
99 Laboratory Staff



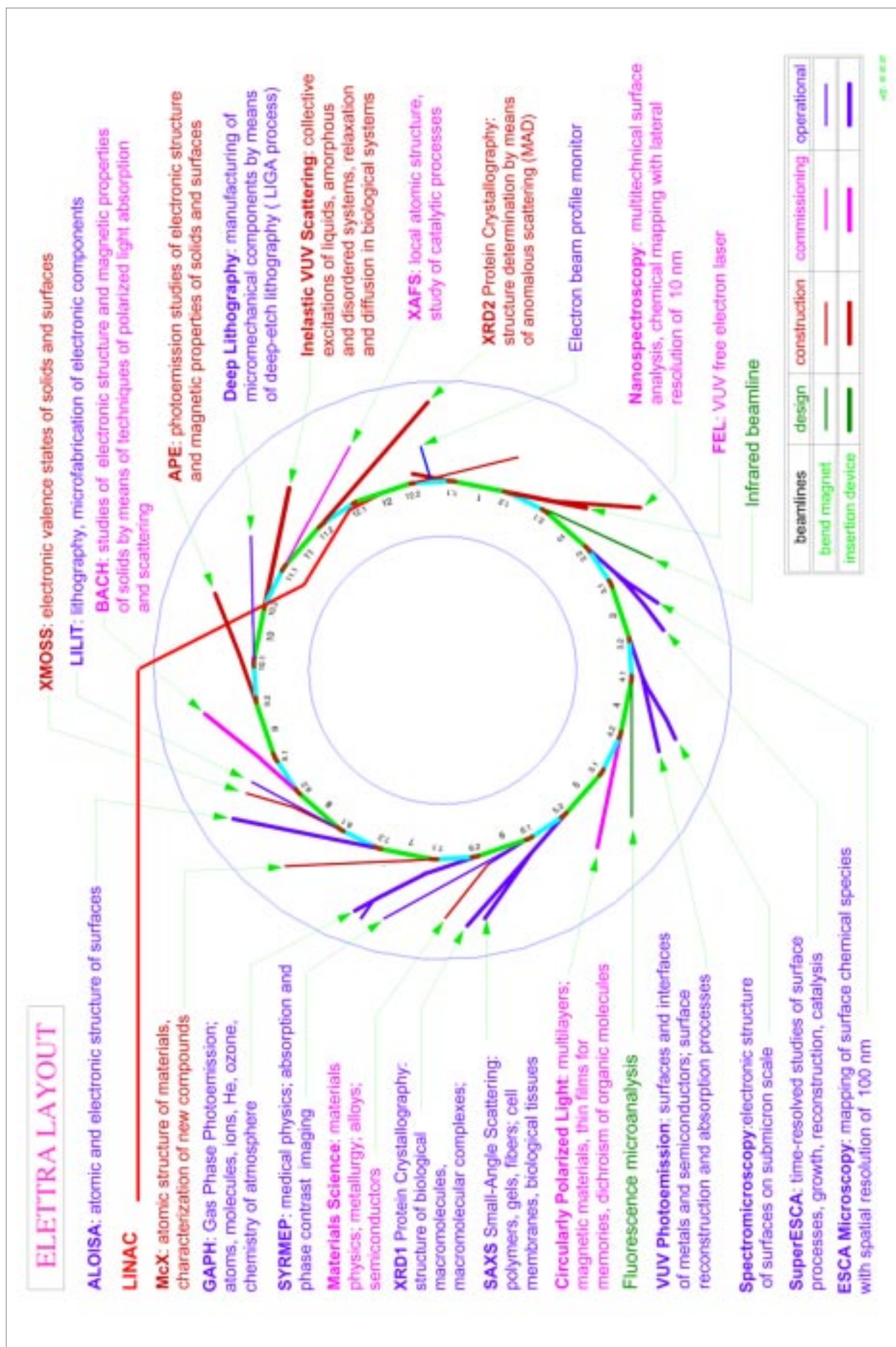
Facts &
figures

STATUS	N°	BEAMLINE	INSTITUTION	PHOTON SOURCE
operational	1	SUPERESCA	SINCROTRONE TS	UNDULATOR U 5.6
	2	ESCAMICROSCOPY	SINCROTRONE TS	BRANCH LINE OF N° 1
	3	VUV PHOTOEMISSION	CNR-ISM	UNDULATOR U 12.5
	4	X-RAY DIFFRACTION	CNR	WIGGLER W 14.0
	5	X-RAY SMALL-ANGLE SCATTERING	AUSTRIAN ACADEMY OF SCIENCES	BRANCH LINE OF N° 4
	6	SURFACE DIFFRACTION (ALOISA)	(CNR) INFN	U 8.0 UNDULATOR/ WIGGLER
	7	GAS-PHASE PHOTOEMISSION	CNR-IMAI INFN UNIV. OF ROME	U 12.5 UNDULATOR
	8	MAMMOGRAPHY (SYRMEP)	UNIVERSITY OF TRIESTE-INFN	BENDING MAGNET
	9	SPECTROMICROSCOPY	SINCROTRONE TS	BRANCH LINE OF N° 3
	10	PROXIMITY PHOTOLITHOGRAPHY (LILIT)	INFN	BENDING MAGNET
	11	DEEP LITHOGRAPHY	SINCROTRONE TS	BENDING MAGNET
under commissioning	12	CIRCULARLY POLARIZED LIGHT	CNR-ISM CNR-ICMAT UNIV. OF ROME I	CROSS FIELD UNDULATOR/WIGGLER
	13	MATERIALS SCIENCE	CZECH ACADEMY OF SCIENCES - PRAGUE	BENDING MAGNET
	14	BEAMLINE FOR ADVANCED DICHROISM (BACH)	INFN	CROSS-FIELD UNDULATOR
	15	NANOSPECTROSCOPY	SINCROTRONE TS	FEL UNDULATOR
	16	EXAFS	SINCROTRONE TS	BENDING MAGNET
under construction	17	DICHROIC PHOTOEMISSION (APE)	INFN	CROSS-FIELD UNDULATOR
	18	SOFT X-RAY OPTICAL SPECTROSCOPY (X-MOSS)	INFN	BENDING MAGNET
	19	XRDI II	SINCROTRONE TS	WIGGLER
	20	INELASTIC ULTRAVIOLET LIGHT SCATTERING	SINCROTRONE TS	UNDULATOR
in design phase	21	POWDER DIFFRACTION (McX)	CNR-UNIV. OF TRENTO	BENDING MAGNET
	22	IR BEAMLINE	UNIVERSITY OF ROME I	BENDING MAGNET
	23	FLUORESCENCE MICROANALYSIS	SINCROTRONE TS	BENDING MAGNET

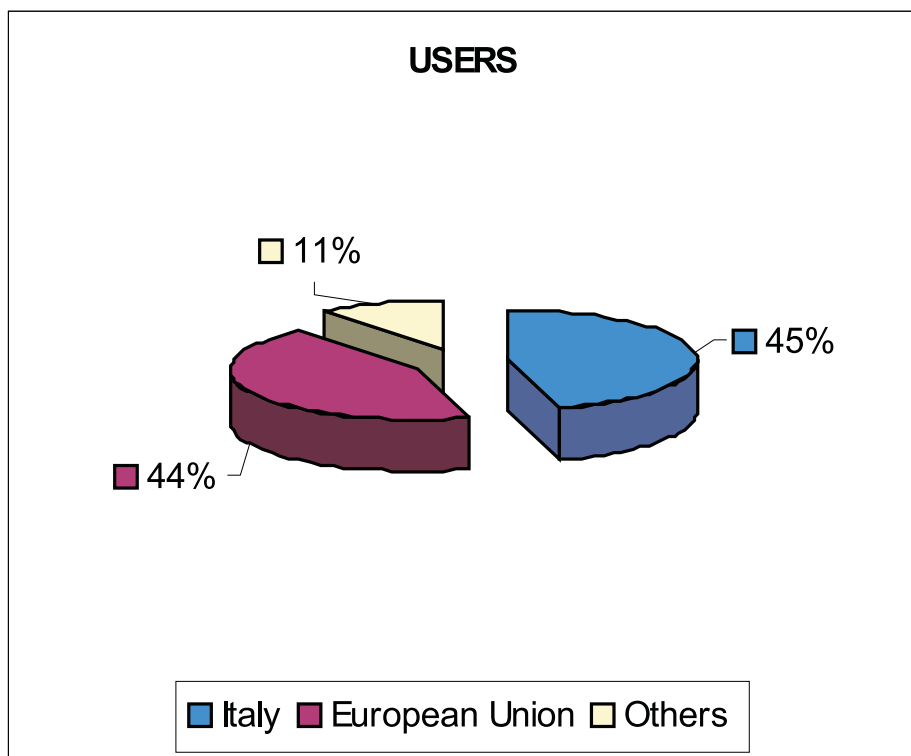
CNR - National Research Council

INFN - National Institute for the Physics of Matter

INFN - National Institute of Nuclear Physics

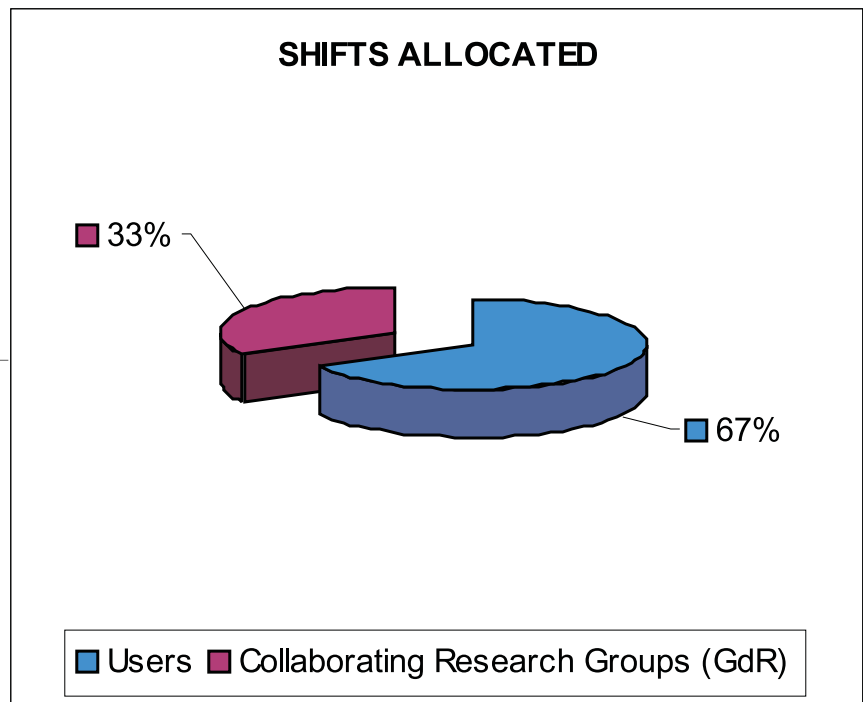


STATISTICS OF ACCEPTED PROPOSALS



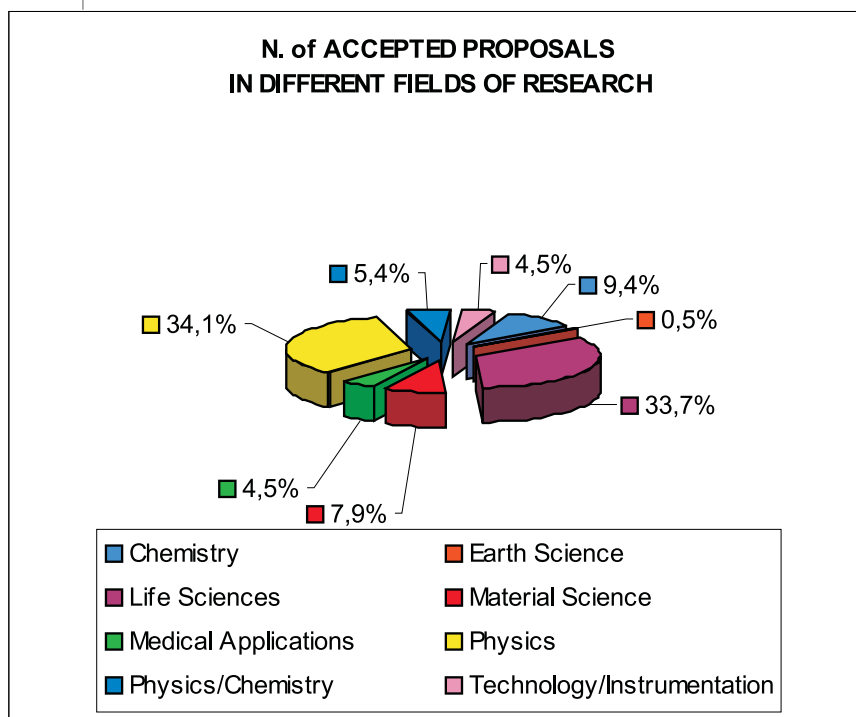
USERS	
Italy	260
European Union	249
Others	63
TOTAL	572

N. of ACCEPTED PROPOSALS IN DIFFERENT FIELDS OF RESEARCH		
Research Fields	n.	%
Chemistry	19	9,4
Earth Science	1	0,5
Life Sciences	68	33,7
Material Science	16	7,9
Medical Applications	9	4,5
Physics	69	34,1
Physics/ Chemistry	11	5,4
Technology/ Instrumentation	9	4,5
TOTAL	202	100,0



SHIFTS* ALLOCATED	
Users	2528
Collaborating Research Groups (GdR)	1248
TOTAL	3776

*A shift lasts 8 hours.



RESOURCES ALLOCATED AT ELETTRA (year 2000)*(figures expressed in EURO)***SINCROTRONE TRIESTE SCPA**

Light Sources Operation	5.629.380,20
Beamlines operation and support activities	5.009.631,92
Laboratory in-house research and development	5.216.214,68
Buildings, other operating costs and general expenses	10.484.075,05
TOTAL	26.339.301,85

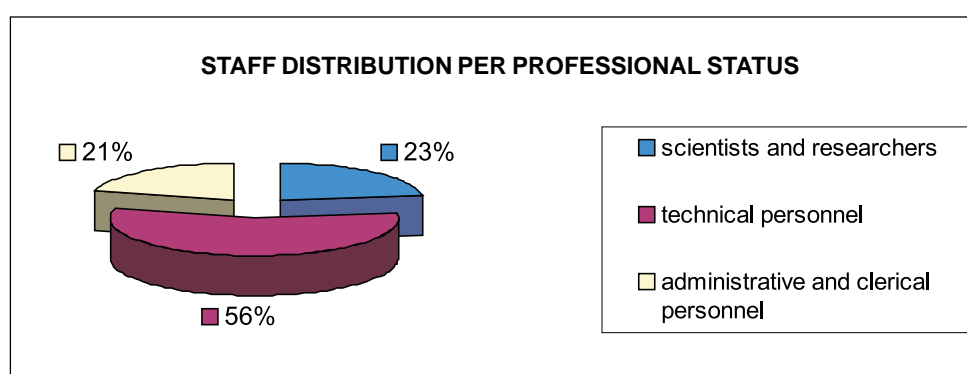
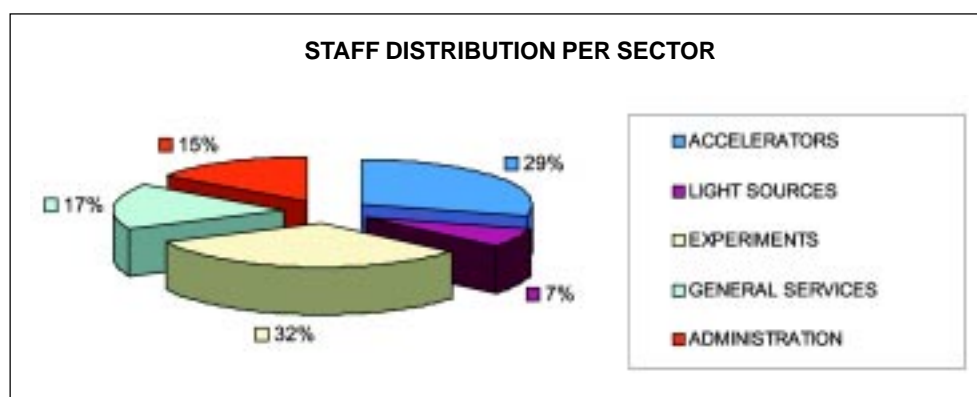
PARTNER INSTITUTIONS

Technical & research personnel	6.197.482,79
Users' support and laboratories operation	7.746.853,49
TOTAL	13.944.336,28

LABORATORY STAFF (Updated August 31st 2001)

	scientists and researchers	technical personnel	administrative and clerical personnel	TOTAL
ACCELERATORS	12	50	3	65
LIGHT SOURCES	3	11	1	15
EXPERIMENTS	34	32	5	71
GENERAL SERVICES	0	25	12	37
ADMINISTRATION	1	8	25	34
TOTAL *	50	126	46	222

* Note: plus 66 people in training and/or visiting and about 130 staff members of the partner GdRs. Total on-site: 418.





Events

- 103** Thirteenth International Conference on Vacuum Ultraviolet Radiation Physics
- 107** Inauguration of the Deep X-Ray Lithography beamline
- 109** VIII USERS' MEETING
- 111** Rai International
- 111** IAEA visit

Thirteenth International Conference on Vacuum Ultraviolet Radiation Physics

Trieste, July 23-27, 2001

K.C. Prince

The triennial VUV conference was hosted in Trieste this year by ELETTRA, in collaboration with the Italian National Research Council (CNR) and National Institute for the Physics of Matter (INFN). This is one of the largest, if not the largest, conference in the field of VUV and soft x-ray science and attracts participants not just from the synchrotron radiation field, but also theoreticians and those working with laser and other sources.

The conference was held at the Stazione Marittima conference centre in downtown Trieste, and located on the waterfront. This was previously the embarkation hall for ocean-going liners that departed for destinations as far away as Australia. In the opening session, the Conference Chair Massimo Altarelli welcomed those present, and recalled that this conference was the latest in a long line held in San Francisco, Tokyo and Paris to mention only the most recent locations. Various other dignitaries including the Mayor of Trieste, representatives of the Region and supporting bodies also welcomed the participants.

The first plenary lecture was given by Olle Björneholm (Uppsala) on the use of resonant core excitation of molecules and clusters to understand femtosecond dynamics. The short lifetime of core holes – a few femtoseconds typically – allows the studies of dissociation processes occurring on this time scale, by means of detuning and other techniques. In addition the recently discovered Auger Doppler effect comes into play due to the kinetic energy of the fragments. This starts with atomic and molecular physics was followed by a contribution from Kiyoshi Ueda (Tohoku University, Sendai) describing work at Spring-8 on nuclear dynamics of polyatomic molecules. By imaging all the ion fragments after photoexcitation, it is possible to understand the dynamics of dissociation in these targets. Uwe Hergenroth (Berlin) reported on very recent measurements on nitrogen, where the gerade and ungerade N 1s core level states have been resolved in photoemission. He also described results showing core level circular dichroism in the gas phase for camphor which is a chiral molecule.

A wide range of other physics was discussed, for instance Jan-Erik Rubensson (Uppsala) presented fluorescence results from doubly excited helium, and M. Krisch (ESRF, Grenoble) showed how x-ray Raman scattering from low Z materials could yield the same results as soft x-ray core level NEXAFS without the need for vacuum, and indeed could provide much more information as well, in the form of non-dipole transitions. Chuck Fadley (University of California Davis) spoke about core level spectroscopy and diffraction, Enzo Di Fabrizio (INFN, Trieste) described some exciting new developments in zone plate imaging using phase contrast. A notable presentation from a related field was given by Prof. R. Wiesendanger who talked about spin-resolved spectromicroscopy with atomic resolution.

Soft x-ray microscopy based on photoemission or photoabsorption contrast and its recent development and applications in different domains of material research, biology etc was a subject of keen interest with a plenary lecture by C. Larabell (University of California in San Francisco), and talks given by F. Nolting (PSI, Switzerland and ALS Berkeley), J. Susini (ESRF Grenoble), Adam Hitchcock (McMaster University, Hamilton, Canada), C.A. Larabell (University of California San Francisco), Chris Jacobsen (SUNY, Stony Brook, USA) among others. Contributions related to catalysis were presented by Ronald Imbihl (Hannover), Falko Netzer (Graz), Giorgio Paolucci (ELETTRA) among others. This is just a selection from a wide program that included current results on superconductors, magnetism and other hot topics.

Given the highly developed culinary culture of Italy, the conference dinner was perhaps the item that took up more time and attention of the organisers than any other single task. It was held in Muggia, a small town across the bay from Trieste, and the participants travelled there in two large, open boats. As thunderstorms occur in Trieste at this time of year, conference organiser Giovanni Comelli awoke on the day of the dinner and nervously read the weather forecast: possible thundery showers. Throughout the

day the weather tormented Giovanni by alternately clearing and clouding over. However he resisted the temptation to have a nervous breakdown, and was suitably rewarded: there was not a drop of rain during the trip across the bay, and dinner was enjoyed in the open, under the warm Italian night sky, with a magnificent view out across the Adriatic sea towards Trieste. The efforts of the organising committee paid off in the form of a memorable banquet.

The last session of the scientific program on the final day was begun by Ernst Bauer (Arizona State University) who presented very fresh results from the Nanospectroscopy beamline at ELETTRA. He showed a range of photoemission microscope images with magnetic contrast from several structures, taken using the new undulator based source. He was followed by Michel Van Hove (LBNL, Berkeley) who reviewed recent developments in the field of photoelectron diffraction and holography. The very last contribution was from T. Takahashi (Tohoku University, Sendai) who showed how very high resolution photoemission can contribute to our understanding of strongly correlated systems like superconductors.

After the conference, there was a tour of the nearby synchrotron light source, ELETTRA, the participants had the chance to see the beamlines and discuss science with the staff and partners of this third generation source.

The site of the next conference, VUV-XIV, was announced in the closing session: it will be in Cairns, Australia, in the year 2004. The proposal for this site had been presented by Brenton Lewis of the Australian National University, Canberra, and he described the facilities available, the temperate weather of Cairns in July, and the beautiful surrounding area. In addition he updated the audience on the progress of plans to build an Australian synchrotron.

Ingolf Lindau, Chairman of the International Advisory Board, summed up the conference. On a sad note, he pointed out that since the last VUV conference a number of well-known colleagues had died (see separate box.) The International Advisory Board is in charge of supervising the organisation of the VUV conference and members are elected for 3 conferences, a period of 9 years. The outgoing and incoming members are:

Outgoing	Incoming
M.L. Cohen (USA)	E. Shirley (USA)
K. Codling (Great Britain)	D.P. Woodruff (Great Britain)
D. L. Ederer (USA)	A.P. Hitchcock (Canada)
B. Lewis (Australia)	F. Larkins (Australia)
I. Lindau (Sweden)	J. Nordgren (Sweden)
I. Nenner (France)	P. Morin (France)
E. Verkhovtseva (Ukraine)	G. Margaritondo (Switzerland)
New honorary members:	
K. Codling, L. Hedin, T. Ishii and D. Shirley.	

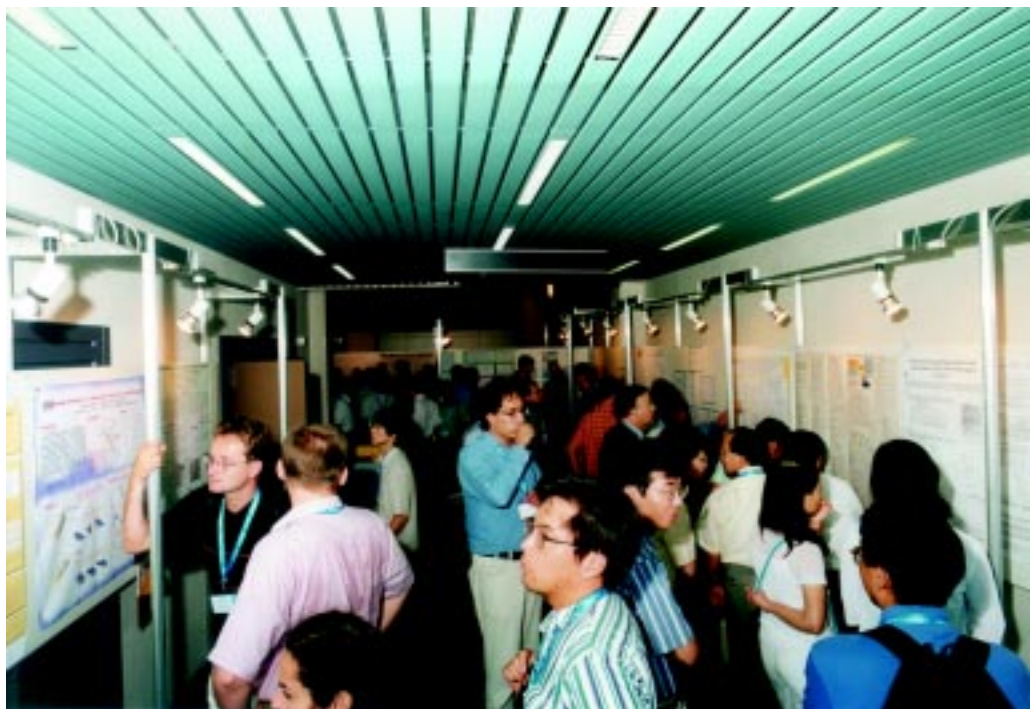
The conference continues to be vigorous and attract a wide range of participants from around the world. The number attending was about constant over the last three conferences, but the range of scientific activity was broad. Ingolf thanked all of the committee members and others who had contributed to the organisation, particularly Maya Kiskinova on the Program committee and Giovanni Comelli, the Chair of the local organising committee.

You can read the abstracts of the conference on the ELETTRA internet site (www.elettra.trieste.it): click on VUV XIII under News and Events. By the time you read this the photographs from the conference will also be posted here. Finally the proceedings of the conference will be available next year as a special volume of Surface Review and Letters, with your correspondent, Maya Kiskinova and Giovanni Comelli as editors.



The opening session of the conference, during the address of the Mayor of Trieste, Roberto Dipiazza (far right.)

Participants at the poster session.





Departure for the conference dinner. In the background, the conference centre is on the left, and the waterfront of Trieste is on the right.

The conference dinner at Porto San Rocco, Muggia, looking out across the bay towards Trieste.



Inauguration of the Deep X-Ray Lithography beamline (15, 16 March 2001)



Antonino Cuffaro, Under-Secretary of State at the Italian Ministry of University and Scientific Research, visiting the Laboratory between Carlo Rizzuto, ELETTRA Chairman (left), and Adolfo Savoia, Co-Director of the Experiments Sector (right).



Philippe Bousquin, EU Commissioner for Research (right), visiting ELETTRA and the Deep X-Ray Lithography beamline.



VIII USERS' MEETING (4-5 December 2000)



A presentation held by Carlo J. Bocchetta, Director of the Accelerators Sector at ELETTRA.



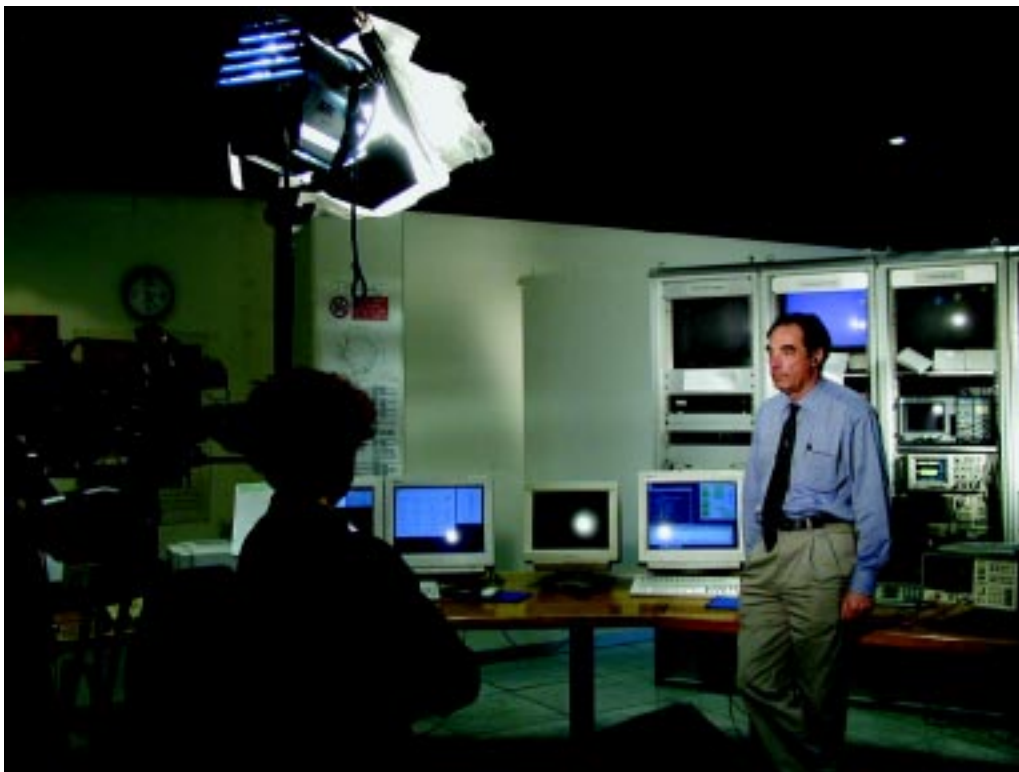
Conference dinner.

Participants to the Satellite Workshop “Challenges in Crystallography of Macromolecular Assemblies” (5-6 December 2000).



Rai International

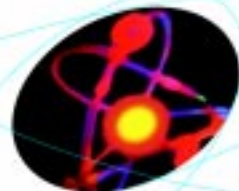
Massimo Altarelli, ELETTRA Managing Director, interviewed by Rai International (3 April 2001).



IAEA visit

Delegation of the International Atomic Energy Agency -IAEA- visiting the Laboratory (2 February 2001).





AREA Science Park

*a world for research
and innovation*



AREA Science Park of Trieste is one of the main multi-sector

science and technology parks in Europe: nearly 1400 specialised people work in more than 60 national and international research and hi-tech organizations which include public and private R&D labs, branch offices, innovative enterprises, training and educational centres. Their activities refer to a wide number of sectors, such as biotechnology, biomedical technologies, physics and new materials, electronics and electro-optics, informatics and multimedia systems, telematics and communication, environmental technologies.

Current contracts, where knowledge and market meet, concern chemical, pharmaceutical, automobile, environment food and space industries.

AREA Science Park holds the headquarters and the premises of some international excellence centres: among them the Sincrotrone Trieste, the company that manages the synchrotron radiation laboratory ELETTRA, stands out as one of the most advanced companies in the sector of research on materials.



Sincrotrone Trieste facilitates the access and the use of the ELETTRA scientific facilities to AREA Science Park tenants and its associates.

AREA Science Park is managed by a non-profit public consortium, Consorzio per l'AREA di ricerca, that is strongly committed to promote industrial research and market-oriented technologies, disseminate technological innovation through a close research-industry interaction and support the creation of innovative start-up companies. Its commitments also include financial support for research and educational projects, marketing, administrative and technical assistance, information/telematic services and promotional activities.



AREA

SciencePark

AREA Science Park
Padriciano 99, 34012 Trieste
Phone (39) 040 375 111 Fax (39) 040 226698
<http://www.area.trieste.it>
e-mail: info@area.trieste.it

ÅGREN P.	30		DESNICA U.V.	33
ALBOUY P.A.	36		DESNICA-FRANKOVIC I.D.	33
AMENITSCH H.	16,	30, 36	Di COSTANZO L.	59
ANDERSSON J.	30		Di FABRIZIO E.	72
ARFELLI F.	12		DJINOVIC-CARUGO K.	26
AVALDI L.	55		DUBCEK P.	33
BABONNEAU F.	36		ELLIS I.O.	12
BALKENENDE A. R.	36		EVANS A.	12
BARALDI A.	50		EVANS S.	12
BARINOV A.	53,	68	FABRIS A.	81
BATTERA G.	55		FAVA C.	70
BERNSTORFF S.	16,	33	FERIANIS M.	86
BOCCHETTA C.J.	76,	81	FERMANI S.	22
BOGGIS C.R.M.	12		FLOREANO L.	40
BORISENKO S.V.	47		FRATZL P.	16
BOWER C.	68		FRIBOURG S.	10
BRAUN I.C.	10		FRÖMTER R.	47
BRESSANUTTI R.	81		GAIO G.	86
BRUNET-BRUNEAU A.	36		GAMBITTA A.	81
BULFONE D.	81,	86	GARZELLA D.	90
BUSSIAN P.	30		GATTO A.	90
CABRINI S.	72		GAYONE J.E.	50
CAMILLONI R.	55		GEREMIA S.	59
CARNIEL A.	81		GIANNESSI L.	90
CARRATO S.	70		GIURESSI D.	70, 81
CAUTERO G.	70,	81	GOLDEN M.S.	47
CAUTERO M.	70		GOLDONI A.	63, 64
CLARKE J.A.	90		GOTTER R.	40
CONTI E.	10		GREGORATTI L .	53, 64, 68
COUPRIE M.E.	90		GRGIC J.	81
CREPALDI E.L.	36		GROSSO D.	36
CVETKO D.	40		GÜNSTER S.	90
D'ADDATO S.	40		HALL C.J.	12
DANCE D.R.	12		HEUN S.	68
DATTOLI G.	90		HILGENFELD R.	28
De BONA F.	74		HOFMANN PH.	50
De MONTE R.	86		HRICOVINI K.	44
De PADOVA P.	44		HUFTON A.P.	12
De RANTER C.	19		IZAURRALDE E.	10
DEHLER M.	81		JACOBS L.	12
DESAIR J.	19		KAISER N.	90

KAULICH B.	53, 64, 68, 72	RIOUAL S.	55
KISKINOVA M.	53, 63, 64, 68	RIPAMONTI A.	22
KLAUSHOFER K.	16	RISTAU D.	90
KRASTANOV B.	70	ROGERS K.D.	12
LACOVIG P.	70	ROMANATO F.	72
LARCIPRETE R.	64	ROSCHGER P.	16
LEGNER S.	47	ROUVELLOU B.	55
LEWIS R.A.	12	SABATINO P.	22
LINDÉN M.	30	SANCHEZ C.	36
LIZZIT S.	50	SANGALETTI L.	64
LODA G.	81	SCAGLIARINI S.	22
LONZA M.	81, 86	SCHMIDT W.	30
LUCHES P.	40	SCHNEIDER C.M.	47
MARSI M.	90	SCHULTZ CH.	50
MARTIN D.	40	SCHÜTH F.	30
MATTHES F.	47	SERGO R.	70, 81
MAZZOLINI F.	81	SICKER T.	28
McARTHUR P.A.	12	SMALUK V.	81
MENK R.H.	12	SOLER-ILLIA G. J. de A.A.	36
MIAN G.	81	SØNDERGAARD CH.	50
MORENO S.	50	STEFANI G.	55
MORGANTE A.	40	SUSINI J.	72
NEWTON A.	40	SUZUKI S.	68
NOVOA de ARMAS H.	19	TESCH W.	16
OGINO T.	68	TOMMASINI R.	70, 81
OLIVO A.	12	TOSI L.	81
PANGOS N.	81	TROMBA, G.	12
PARIS O.	16	TROST P.	22
PARMIGIANI F.	64	TROVÒ M.	90
PÉRENNÈS F.	74	TURCHINI S.	47
PERFETTI P.	44	TURRI G.	55
PINDER S.E.	12	UNSWORTH P.	40
POLENTARUTTI M.	26	VANDE BROECK A.	19
POOLE M.W.	90	VANDERLEYDEN J.	19
PUPILLO P.	22	VERBOVEN C.	19
PURRELLO R.	59	VICENTE ALVAREZ M. A.	50
QUARESIMA C.	44	WALKER R.P.	90
RABIJNS A.	19	WATANABE Y.	68
RANDACCIO L.	59	WEIGHTMAN P.	40
RICHTER C.	44	WEISS M.S.	28
RIGON L.	12	WILHEIN T.	72

ZAMBON L.	81
ZAMPIERI G.	50
ZANOTTI G.	22
ZENNARO S.	47
ZERROUKI M.	44
ZHOU O.	68
ZHU W.	68
ZIZAK I.	16